

Jordan Journal of Mechanical and Industrial Engineering (JJMIE)

JJMIE is a high-quality scientific journal devoted to fields of Mechanical and Industrial Engineering. It is published by The Hashemite University in corporation with the Jordanian Scientific Research Support Fund.

EDITORIAL BOARD

Editor-in-Chief

Prof. **Nabil Anagreh**

Editorial board

Prof. **Mohammad Ahmad Hamdan**
The University of Jordan

Prof. **Ibrahim A. Rawabdeh**
The University of Jordan

Prof. **Amin Al Robaidi**
Al Balqa Applied University

Assistant Editor

Dr. Khalid Al-Widyan
Hashemite University

Prof. **Naser Al-Hunuti**
The University of Jordan

Prof. **Suhil Kiwan**
The Jordan University of Science and Technology

Prof. **Mahmoud Abu-Zaid**
Mutah University

Dr. Osama Al Meanazel
Hashemite University

THE INTERNATIONAL ADVISORY BOARD

Abu-Qudais, Mohammad
Jordan University of Science & Technology, Jordan

Abu-Mulaweh, Hosni
Purdue University at Fort Wayne, USA

Afaneh Abdul-Hafiz
Robert Bosch Corporation, USA

Afonso, Maria Dina
Institute Superior Tecnico, Portugal

Badiru, Adedji B.
The University of Tennessee, USA

Bejan, Adrian
Duke University, USA

Chalhoub, Nabil G.
Wayne State University, USA

Cho, Kyu-Kab
Pusan National University, South Korea

Dincer, Ibrahim
University of Ontario Institute of Technology,
Canada

Douglas, Roy
Queen's University, U. K

El Bassam, Nasir
International Research Center for Renewable
Energy, Germany

Haik, Yousef
United Arab Emirates University, UAE

Jaber, Jamal
Al- Balqa Applied University, Jordan

Jubran, Bassam
Ryerson University, Canada

Kakac, Sadik
University of Miami, USA

Khalil, Essam-Eddin
Cairo University, Egypt

Mutoh, Yoshiharu
Nagaoka University of Technology, Japan

Pant, Durbin
Iowa State University, USA

Riffat, Saffa
The University of Nottingham, U. K

Saghir, Ziad
Ryerson University, Canada

Sarkar, MD. Abdur Rashid
Bangladesh University of Engineering &
Technology, Bangladesh

Siginer, Dennis
Wichita State University, USA

Sopian, Kamaruzzaman
University Kebangsaan Malaysia, Malaysia

Tzou, Gow-Yi
Yung-Ta Institute of Technology and Commerce,
Taiwan

EDITORIAL BOARD SUPPORT TEAM

Language Editor

Dr. Qusai Al-Debyan

Publishing Layout

Eng. Mohammad Oqdeh

SUBMISSION ADDRESS:

Prof. **Nabil Anagreh**, Editor-in-Chief
Jordan Journal of Mechanical & Industrial Engineering,
Hashemite University,
PO Box 330127, Zarqa, 13133, Jordan
E-mail: jjmie@hu.edu.jo



Hashemite Kingdom of Jordan



Hashemite University

Jordan Journal of
Mechanical and Industrial Engineering

JJMIE

An International Peer-Reviewed Scientific Journal
Financed by Scientific Research Support Fund

<http://jjmie.hu.edu.jo/>

ISSN 1995-6665

Jordan Journal of Mechanical and Industrial Engineering (JJMIE)

JJMIE is a high-quality scientific journal devoted to fields of Mechanical and Industrial Engineering. It is published by The Jordanian Ministry of Higher Education and Scientific Research in corporation with the Hashemite University.

Introduction: The Editorial Board is very committed to build the Journal as one of the leading international journals in mechanical and industrial engineering sciences in the next few years. With the support of the Ministry of Higher Education and Scientific Research and Jordanian Universities, it is expected that a heavy resource to be channeled into the Journal to establish its international reputation. The Journal's reputation will be enhanced from arrangements with several organizers of international conferences in publishing selected best papers of the conference proceedings.

Aims and Scope: *Jordan Journal of Mechanical and Industrial Engineering (JJMIE)* is a refereed international journal to be of interest and use to all those concerned with research in various fields of, or closely related to, mechanical and industrial engineering disciplines. *Jordan Journal of Mechanical and Industrial Engineering* aims to provide a highly readable and valuable addition to the literature which will serve as an indispensable reference tool for years to come. The coverage of the journal includes all new theoretical and experimental findings in the fields of mechanical and industrial engineering or any closely related fields (Materials, Manufacturing, Management, Design, Thermal and Fluid, Energy, Control, Mechatronics, and Biomedical). The journal also encourages the submission of critical review articles covering advances in recent research of such fields as well as technical notes.

Guide for Authors

Manuscript Submission:

High-quality submissions to this new journal are welcome now and manuscripts may be either submitted online or email.

Online: For online and email submission upload one copy of the full paper including graphics and all figures at the online submission site, accessed via <http://jjmie.hu.edu.jo>. The manuscript must be written in MS Word 2010 Format. All correspondence, including notification of the Editor's decision and requests for revision, takes place by e-mail and via the Author's homepage, removing the need for a hard-copy paper trail.

Submission address and contact:

Prof. Nabil Anagreh
Editor-in-Chief
Jordan Journal of Mechanical & Industrial Engineering,
Hashemite University,
PO Box 330127, Zarqa, 13115, Jordan
E-mail: jjmie@hu.edu.jo

Types of contributions: Original research papers and Technical reports

Corresponding author: Clearly indicate who is responsible for correspondence at all stages of refereeing and publication, including post-publication. Ensure that telephone and fax numbers (with country and area code) are provided in addition to the e-mail address and the complete postal address. Full postal addresses must be given for all co-authors.

Original material: Submission of an article implies that the work described has not been published previously (except in the form of an abstract or as part of a published lecture or academic thesis), that it is not under consideration for publication elsewhere, that its publication is approved by all authors and that, if accepted, it will not be published elsewhere in the same form, in English or in any other language, without the written consent of the Publisher. Authors found to be deliberately contravening the submission guidelines on originality and exclusivity shall not be considered for future publication in this journal.

Withdrawing: If the author chooses to withdraw his article after it has been assessed, he shall reimburse JJMIE with the cost of reviewing the paper.

Manuscript Preparation:

General: Editors reserve the right to adjust style to certain standards of uniformity. Original manuscripts are discarded after publication unless the Publisher is asked to return original material after use. Please use MS Word 2010 for the text of your manuscript.

Structure: Follow this order when typing manuscripts: Title, Authors, Authors title, Affiliations, Abstract, Keywords, Introduction, Main text, Conclusions, Acknowledgements, Appendix, References, Figure Captions, Figures and then Tables. Please supply figures imported into the text AND also separately as original graphics files. Collate acknowledgements in a separate section at the end of the article and do not include them on the title page, as a footnote to the title or otherwise.

Text Layout: Use 1.5 line spacing and wide (3 cm) margins. Ensure that each new paragraph is clearly indicated. Present tables and figure legends on separate pages at the end of the manuscript. If possible, consult a recent issue of the journal to become familiar with layout and conventions. All footnotes (except for table and corresponding author footnotes) should be identified with superscript Arabic numbers. To conserve space, authors are requested to mark the less important parts of the paper (such as records of experimental results) for printing in smaller type. For long papers (more than 4000 words) sections which could be deleted without destroying either the sense or the continuity of the paper should be indicated as a guide for the editor. Nomenclature should conform to that most frequently used in the scientific field concerned. Number all pages consecutively; use 12 or 10 pt font size and standard fonts.

Corresponding author: Clearly indicate who is responsible for correspondence at all stages of refereeing and publication, including post-publication. The corresponding author should be identified with an asterisk and footnote. Ensure that telephone and fax numbers (with country and area code) are provided in addition to the e-mail address and the complete postal address. Full postal addresses must be given for all co-authors. Please consult a recent journal paper for style if possible.

Abstract: A self-contained abstract outlining in a single paragraph the aims, scope and conclusions of the paper must be supplied.

Keywords: Immediately after the abstract, provide a maximum of six keywords (avoid, for example, 'and', 'of'). Be sparing with abbreviations: only abbreviations firmly established in the field may be eligible.

Symbols: All Greek letters and unusual symbols should be identified by name in the margin, the first time they are used.

Units: Follow internationally accepted rules and conventions: use the international system of units (SI). If other quantities are mentioned, give their equivalent in SI.

Maths: Number consecutively any equations that have to be displayed separately from the text (if referred to explicitly in the text).

References: All publications cited in the text should be presented in a list of references following the text of the manuscript.

Text: Indicate references by number(s) in square brackets in line with the text. The actual authors can be referred to, but the reference number(s) must always be given.

List: Number the references (numbers in square brackets) in the list in the order in which they appear in the text.

Examples:

Reference to a journal publication:

[1] M.S. Mohsen, B.A. Akash, "Evaluation of domestic solar water heating system in Jordan using analytic hierarchy process". Energy Conversion & Management, Vol. 38 (1997) No. 9, 1815-1822.

Reference to a book:

[2] Strunk Jr W, White EB. The elements of style. 3rd ed. New York: Macmillan; 1979.

Reference to a conference proceeding:

[3] B. Akash, S. Odeh, S. Nijmeh, "Modeling of solar-assisted double-tube evaporator heat pump system under local climate conditions". 5th Jordanian International Mechanical Engineering Conference, Amman, Jordan, 2004.

Reference to a chapter in an edited book:

[4] Mettam GR, Adams LB. How to prepare an electronic version of your article. In: Jones BS, Smith RZ, editors. Introduction to the electronic age, New York: E-Publishing Inc; 1999, p. 281-304

Free Online Color : If, together with your accepted article, you submit usable color and black/white figures then the journal will ensure that these figures will appear in color on the journal website electronic version.

Tables: Tables should be numbered consecutively and given suitable captions and each table should begin on a new page. No vertical rules should be used. Tables should not unnecessarily duplicate results presented elsewhere in the manuscript (for example, in graphs). Footnotes to tables should be typed below the table and should be referred to by superscript lowercase letters.

Notification: Authors will be notified of the acceptance of their paper by the editor. The Publisher will also send a notification of receipt of the paper in production.

Copyright: All authors must sign the Transfer of Copyright agreement before the article can be published. This transfer agreement enables Jordan Journal of Mechanical and Industrial Engineering to protect the copyrighted material for the authors, but does not relinquish the authors' proprietary rights. The copyright transfer covers the exclusive rights to reproduce and distribute the article, including reprints, photographic reproductions, microfilm or any other reproductions of similar nature and translations.

Proof Reading: One set of page proofs in MS Word 2010 format will be sent by e-mail to the corresponding author, to be checked for typesetting/editing. The corrections should be returned within **48 hours**. No changes in, or additions to, the accepted (and subsequently edited) manuscript will be allowed at this stage. Proofreading is solely the author's responsibility. Any queries should be answered in full. Please correct factual errors only, or errors introduced by typesetting. Please note that once your paper has been proofed we publish the identical paper online as in print.

Author Benefits:

No page charges: Publication in this journal is free of charge.

Free offprints: One journal issues of which the article appears will be supplied free of charge to the corresponding author and additional offprint for each co-author. Corresponding authors will be given the choice to buy extra offprints before printing of the article.

PAGES**PAPERS**

- 119 - 125 **The Optimization of Thickness and Permeability of Wick Structure with Different Working Fluids of L-Shape Heat Pipe for Electronic Cooling.**
Mohamed H.A Elnaggar.
- 127 – 136 **Numerical Study of the Hydrodynamic Structure of a Water Savonius Rotor in a Test Section**
Ibrahim Mabrouki , Zied Driss , Mohamed Salah Abid
- 137– 141 **Studying the Design and Verification of 5-axis NC program under the Manufacturing System**
Wang Zhun
- 143– 151 **Experimental Investigations on the Electrochemical Machining Characteristics of Monel 400 Alloys and Optimization of Process Parameters**
M.Kalaimathi, G.Venkatachalam and M.Sivakumar
- 153 – 160 **Statistical Investigation on Effect of Electroless Coating Parameters on Coating Morphology of Short Basalt Fiber**
S. Ezhil Vannan, S. Paul Vizhian
- 161– 167 **The Performance Study of Alcohol in an Air Gap Ceramic Insulated Diesel Engine with Brass Piston**
S Sunil Kumar Reddy , V.Pandurangadu , M.Venkat Rao
- 169 – 176 **Direct Torque Control of Induction Motor Based on Space Vector Modulation Using a Fuzzy Logic Speed Controller**
Abdeselem Chikhi
-

The Optimization of Thickness and Permeability of Wick Structure with Different Working Fluids of L-Shape Heat Pipe for Electronic Cooling

Mohamed H.A. Elnaggar *

Engineering Department, Palestine Technical College, Deir EL-Balah, Gaza Strip, Palestine.

Received 11 Jan 2014

Accepted 30 May 2014

Abstract

As part of the ongoing research on finned L-shape heat pipes for electronic cooling, the present work focuses on the optimization of the thickness and permeability of wick structure of L-shape heat pipe, using different working fluids. D-Optimal Designs Software is used to obtain the optimal solution to align the competing parameters such as the working fluid properties, thickness of the wick and the type of wick structure. The optimization results yielded that a wick thickness of 0.52 mm and permeability of $1.39E-11 \text{ m}^2$ with water as a working fluid could produce the minimum temperature difference between the evaporator and condenser sections of $9.56 \text{ }^\circ\text{C}$ and liquid pressure drop of 5730 Pa, which could increase the heat transport capability from 35 W to 43 W. These results reveal that the performance of L-shape heat pipe in terms of heat transport capability is improved by 20%.

© 2014 Jordan Journal of Mechanical and Industrial Engineering. All rights reserved

Keywords: L-Shape Heat Pipe; D-Optimal Designs; Wick Structure; Working Fluid

1. Introduction

The electronic devices have highly integrated circuits with an ever increasing power dissipating high heat flux which leads to an increase in the operating temperature of devices; this results in shortening the life time of the electronic devices [1]. Consequently, the need for cooling techniques to dissipate the associated heat is quite obvious. It is highly desirable to explore high-performance cooling devices, especially for CPU cooling. Thus, heat pipes are regarded as a promising way for cooling the electronic equipment. As an alternative to the traditional heat sinks, two-phase cooling devices, such as heat pipe and thermosyphon, have emerged as promising heat transfer devices; the effective thermal conductivity of a heat pipe can be 10 to 200 times more than that of a solid copper rod of the same diameter [2].

Substantial numerical and experimental works have been reported on the application of heat pipes [3-6]. Park [7] presented a numerical model of heat pipe for optimum placement of satellite equipment to predict the temperature profile by assuming cylindrical two-dimensional laminar flow for vapor, and conduction heat transfer for wall and wick. Noh and Song [8] focused on heat pipe with multiple heaters to predict the characteristics on transient heat pipe operation. Xie *et al.* [9] presented the applications of heat pipes in the portable computers, and their use was illustrated in Pentium processor-based notebooks and sub-notebooks. Xie *et al.* [10] summarized the future outlook

of using the heat pipe for cooling personal computers, through reviewing the performance of several heat pipes with different designs and the new technology used for cooling personal computers. Seok-Hwan *et al.* [11] studied experimentally a new woven-wire-type wick for Miniature Heat Pipes (MHP), which had a high productivity and a large capillary limit. They used MHP with diameters of 3 mm or 4 mm which could be used for notebook- CPU cooling. Wuttijumnong *et al.* [12] reviewed the various cooling solutions using heat pipe and vapor chamber for cooling high power processors in a confined space of the notebook.

Recently, heat sinks with finned U-shape heat pipes have been introduced for cooling the high-frequency microprocessors such as Intel Core 2 Duo, Intel Core 2 Quad, AMD Phenom series and AMD Athlon 64 series [13]. The work of Wang *et al.* [14], Wang [15], Liang & Hung [13] and Elnaggar *et al.* [16] were remarkable contributions to finned U-shape heat pipes where they have been introduced to cooling the high-frequency microprocessors.

Recently, [17] and [18] have exerted effort to optimize the operating conditions such as heat input and the cooling air velocity without addressing the internal parameters of the heat pipe such as the working fluid properties, thickness of the wick and the type of wick structure.

The decrease in the pore size of the wick causes low wick permeability, which increases the maximum capillary pumping head generated by the wick to overcome the total pressure drop within the heat pipe. On the other hand, the

* Corresponding author. e-mail: mohdhn@yahoo.com.

permeability should be large in order to have a small liquid pressure drop and, therefore, a higher heat transport capability. Furthermore, the effective thermal conductivity in the liquid-wick region also plays an important role in the heat pipe performance as the high value of this parameter gives a small temperature drop across the wick, which increases the thermal performance of the heat pipe. The rate of mass transfer increases with the increase in thermal conductivity and porosity, while it decreases with the increase in viscosity [19]. The effective thermal conductivity in the liquid-wick region depends on the material of the wick structure, the working fluid properties, the thickness of the wick and the type of wick structure. These parameters present conflicting properties in most wick designs. Accordingly, an optimal wick design requires harmonization between these contradictory features.

Therefore, in the present study, D-Optimal Designs Software is used to obtain the optimal solution to align the competing parameters such as the working fluid properties, the thickness of the wick and the type of wick structure. The three significant parameters, wick thickness, wick permeability, and working fluids, are considered, in this study, with the objective of minimizing the temperature difference between the evaporator and condenser sections (ΔT) and liquid pressure drop ΔP_l to get the best performance of the heat pipe.

2. Materials and Methods

2.1. L-Shape Heat Pipe

As shown in Figure 1, the finned heat pipe under investigation serves to cool the CPU of a modern notebook. In this system, the heat pipe is used to transfer heat from CPU to the fins in a remote location, usually in

the sides or corners of the notebook PC. The copper base plate directly communicates with the evaporator section of the heat pipe while the condenser section is equipped with 50 rectangular fins of 20mm \times 10 mm size [17]. The total length of the heat pipe is 212 mm (the length of evaporator, adiabatic and condenser sections are 30 mm, 110 mm and 72 mm, respectively). The system is supported by a radial fan with dimensions of 73 mm \times 73 mm \times 10 mm (width \times length \times thickness).

The heat transfers from processor (CPU) to base plate then to the heat pipe and then to the fins, and the heat is dissipated to the surrounding area by a fan.

The thermal resistance of the heat pipe (R_{hp}) is:

$$R_{hp} = \frac{\Delta T}{Q} \quad \text{where} \quad \Delta T = T_e - T_c \quad (1)$$

where T_e is the evaporator temperature and T_c is the condenser temperature and Q is the rate of heat transfer.

2.2. Simulation Results

This study is extend to the work of [17] and [20], which investigated the effect of the thickness and permeability of the wick structure on L-shape heat pipe performance using different working fluids. The applied heat was 35 W with coolant airflow rate of 6.5 m³/h. As shown in Figures 2 and 3, which were illustrated by [20], a good performance of heat pipe was achieved by employing water with 0.5 mm thickness of sintered copper powder (recorded the smallest temperature difference 9.8 °C) but the unfavorable high pressure (6563 Pa) resulted in a low heat transport capability at the liquid-wick region. Consequently, the current study resolved this issue by using the D-Optimal Designs software to obtain the optimal performance associated with a moderately low pressure in liquid-wick region to achieve the maximum heat transport capability.

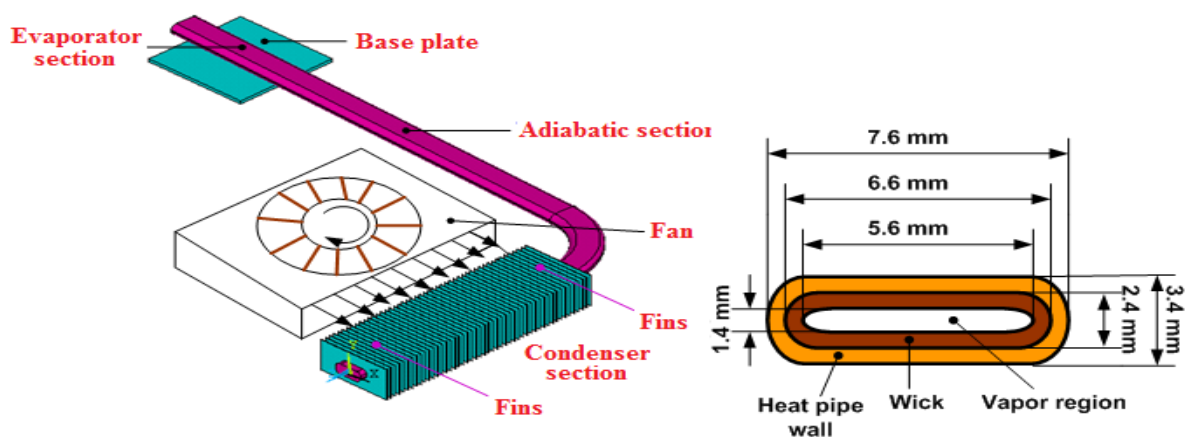


Figure 1. Finned flat heat pipe and its cross-section [17].

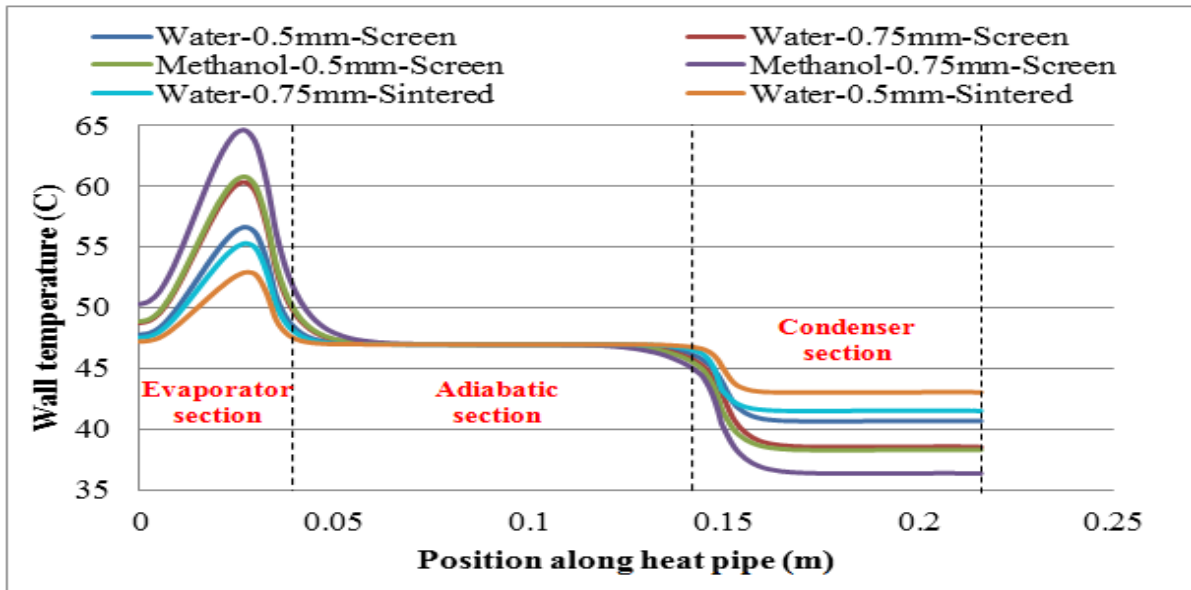


Figure 2. Wall temperature distribution along the heat pipe with various thicknesses and types of wicks and at different working fluids [20].

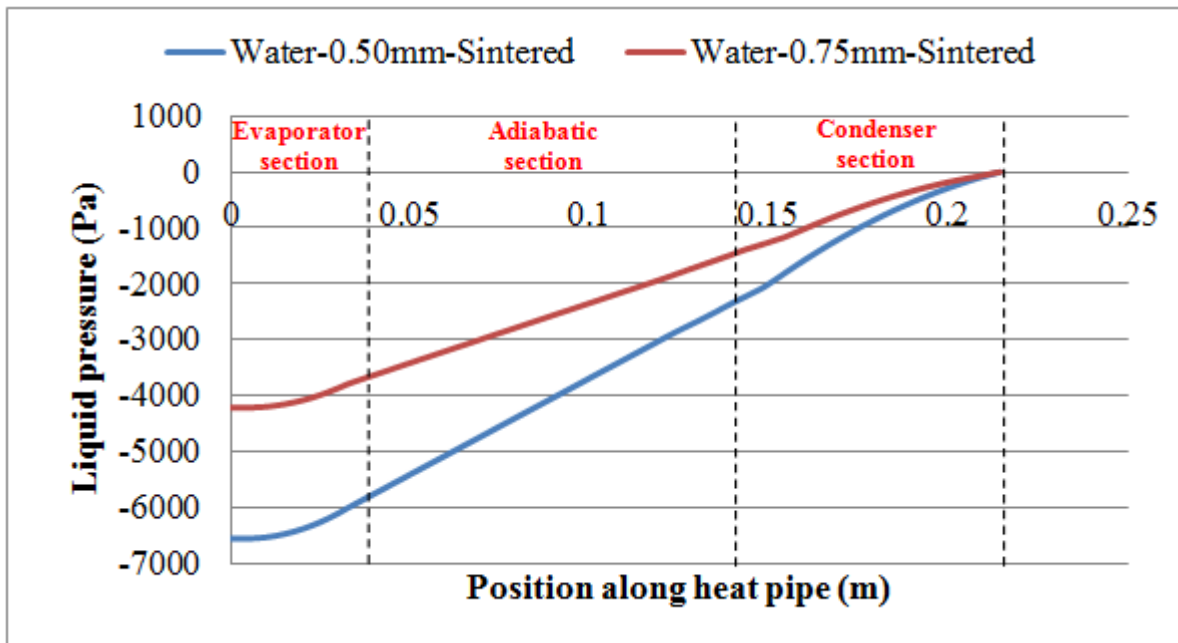


Figure 3. Predict liquid (Water) pressure distribution of heat pipe with sintered copper powder wick at various thicknesses [20].

2.3. Analytical method²³

The maximum achievable heat transfer by the heat pipe can be obtained from the equation [21]:

$$Q_{max} = \left(\frac{\rho_l \sigma_l h_{fg}}{\mu_l} \right) \left(\frac{A_w K}{L_{eff}} \right) \left(\frac{2}{r_{eff}} \right) \quad (2)$$

where μ_l = liquid viscosity, L_{eff} = effective length of the heat pipe, ρ_l = liquid density, K = wick permeability,

A_w = wick cross-sectional area, h_{fg} = heat of vaporization of liquid, σ_l is surface tension and r_{eff} is the effective radius of the pores of the wick.

The properties of the working fluid change as follows:

$$\begin{aligned} \rho_l &= 989 \text{ Kg/m}^3, \\ \sigma_l &= 0.066 \text{ N/m}, \\ \rho_v &= 0.2 \text{ Kg/m}^3 \text{ and} \\ h_{fg} &= 2.4 \times 10^6 \text{ J/kg} \end{aligned}$$

3. D-Optimal Designs

D-Optimal approach of Design of Experiment (DOE) software program is used for the design of experiments, statistical analysis, modeling and optimization. A D-optimal design is a computer aided design which contains the best subset of all possible experiments. Depending on a selected criterion and a given number of design runs, the best design is created by a selection process.

The optimality of a design depends on the statistical model and is assessed with respect to a statistical criterion, which is related to the variance-matrix of the estimator. Specifying an appropriate model and specifying a suitable criterion function require both an understanding of statistical theory and practical knowledge.

D-optimal designs for multi-factor experiments with both Numeric and Categorical factors are used. The factors can have a mixed number of levels. D-optimal designs are constructed to minimize the generalized variance of the estimated regression coefficients.

In this study, the analysis depends on the simulation results of Elnaggar [20] instead of experiments to obtain the optimal solution to align the competing parameters.

3.1. Factors Definition

This program was implemented based on the simulation results rather than the results of experiments. The three significant factors considered are: two numeric factors such as wick thickness (A) and wick permeability (B), and the categorical factor, working fluids (C), as presented in Table 1. Each factor is varied at two levels: low actual and high actual. Additionally, in this design, two response factors are used, such as the temperature difference between the evaporator and the condenser sections (ΔT) and the liquid pressure drop ΔP_1 .

Table 1. Factors of D-Optimal design

Factor	Name	Units	Type	Low Actual	High Actual
A	Thickness	mm	Numeric	0.5	0.75
B	Permeability	m ²	Numeric	1.17E-11	1.93E-10
C	Working fluids		Categorical	Water	Methanol

Table 2. Response values for different simulation conditions

Run no.	Factor 1 A:Thickness (mm)	Factor 2 B:Preamability (m ²)	Factor 3 C:Working fluids	Response 1 Temperature difference (°C)	Response 2 Pressure drop (Pa)
1	0.5	1.93E-10	Water	16	1129
2	0.5	1.93E-10	Water	16	1129
3	0.5	1.17E-11	Water	9.8	6563
4	0.5	1.93E-10	Methanol	22.5	1789
5	0.75	1.93E-10	Water	21.8	633
6	0.75	1.93E-10	Methanol	28.27	1083
7	0.75	1.17E-11	Water	13.8	4219
8	0.75	1.93E-10	Methanol	28.27	1083
9	0.75	1.93E-10	Water	21.8	633
10	0.5	1.93E-10	Methanol	22.5	1789

A total of 10 simulation runs were enhanced with 4 runs replications to assess the pure error, as illustrated in Table 2. Methanol with copper powder wick was excluded because it results in an exceedingly high pressure in the liquid-wick region.

4. Results and Discussion

4.1. Results of D-Optimal Designs

The model created for predicting the temperature differences between the evaporator and the condenser sections (ΔT) and the liquid pressure drops (ΔP_1) has been considered sensible. The final regression models, in terms of coded factors, are expressed by the following linear equations:

$$\Delta T = -2.22819 + 21.71200 * t_w + 3.91616 \times 10^{10} * K \quad (3)$$

$$\Delta P_1 = +8056.04799 - 3798.40 * t_w - 2.48759 \times 10^{13} * K \quad (4)$$

B. Methanol is used as working fluid

$$\Delta T = +4.25681 + 21.71200 * t_w + 3.91616 \times 10^{10} * K \quad (5)$$

$$\Delta P_1 = +8611.04799 - 3798.40 * t_w - 2.48759 \times 10^{13} * K \quad (6)$$

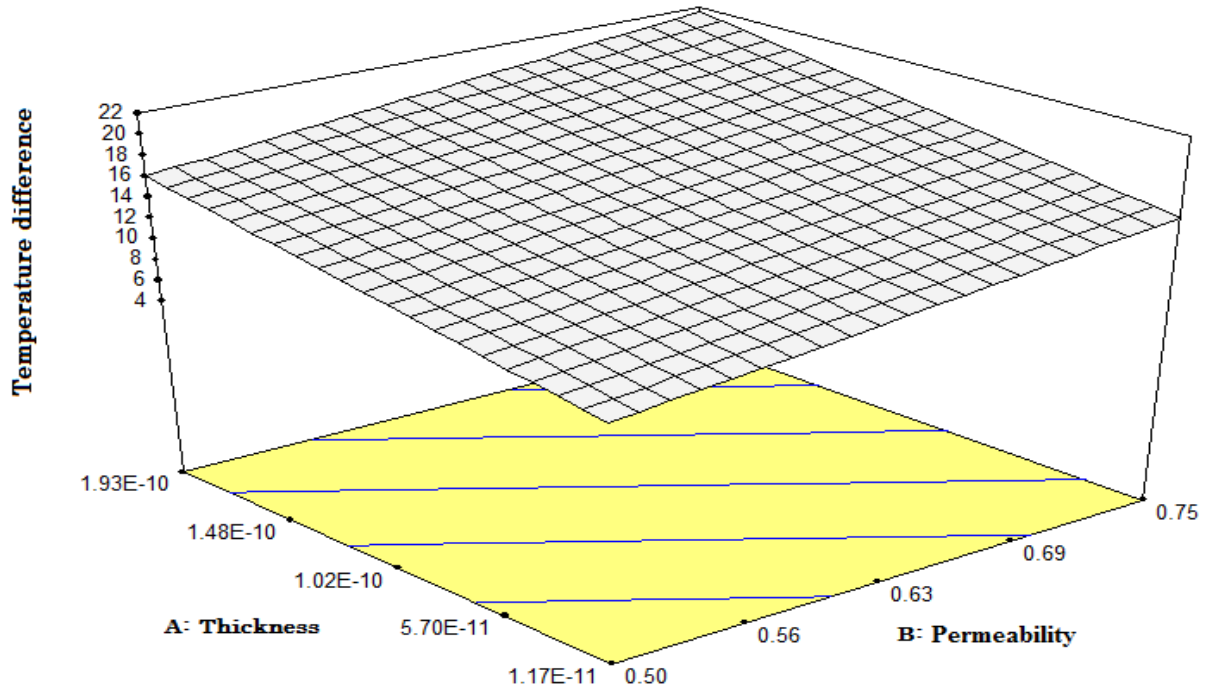
Where ΔT is the temperature difference between the evaporator and the condenser sections (°C), ΔP_1 is liquid pressure in wick region (Pa), t_w is wick thickness (mm) and K is the wick preamability (m²).

4.2. Interaction between Factors

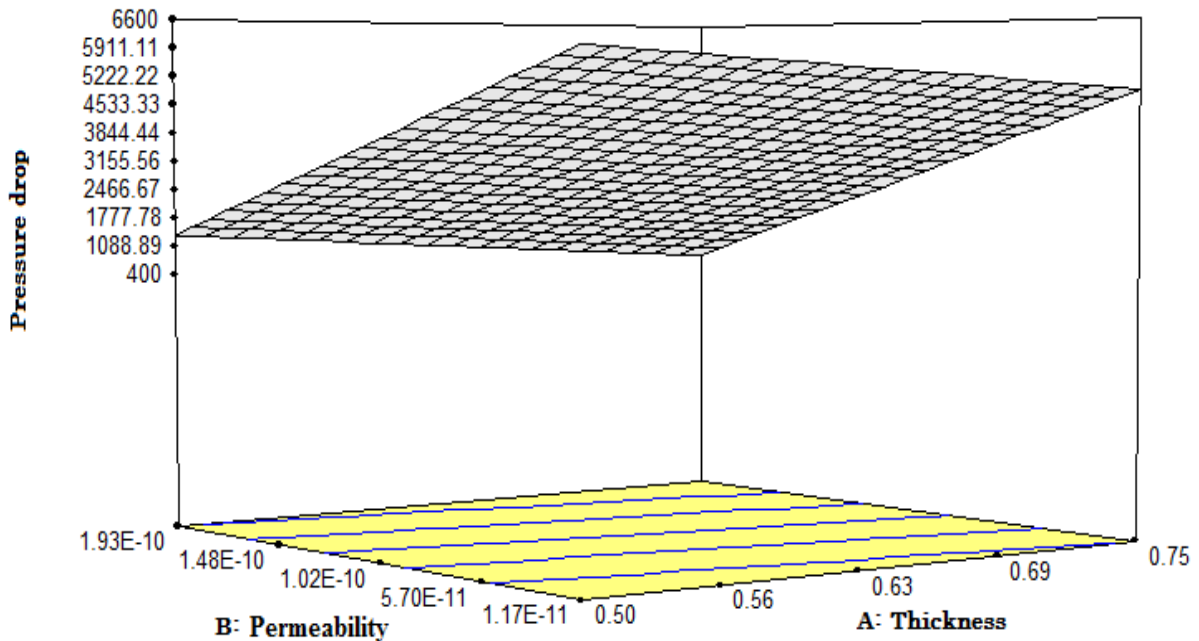
Equations 3, 4, 5 and 6 are used to visualize the influences of factors (i.e., wick thickness and wick permeability) on temperature difference ΔT and liquid pressure drop ΔP_1 as shown in Figure 4. For both working fluids, water and methanol, the curvature of 3D surfaces indicates that the wick permeability and wick thickness

have a major effect on temperature difference and pressure drop. As shown in Figures 4 (a) and 4 (c) for both water and methanol, the decrease in permeability increases the effective thermal conductivity of liquid-wick, and hence the temperature difference decreases. Moreover, with the decrease in the wick thickness, the temperature difference decreases. Additionally, for both working fluids, water and methanol, the decrease in the wick permeability leads to a

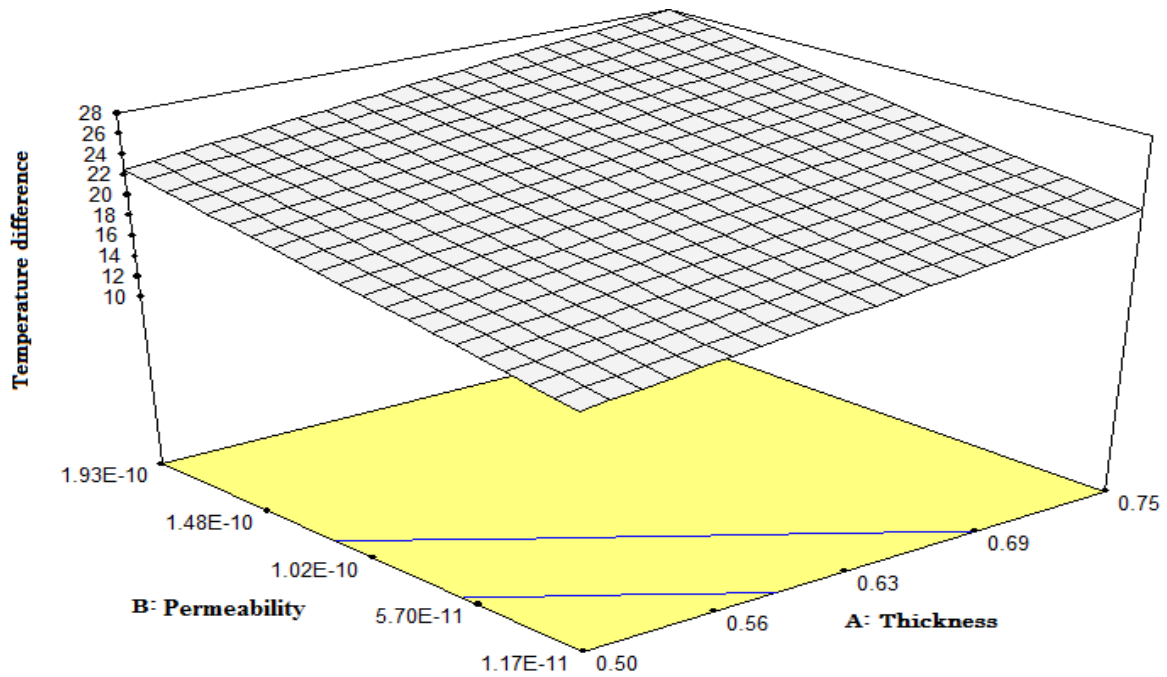
remarkable increase of the liquid pressure drop and the decrease in the wick thickness also leads to an increase in the liquid pressure drop, as shown in the Figures 4 (b) and 4 (d). The pressure drop resulting from the use of methanol is greater than the pressure drop resulting from the use of water, as the viscosity of methanol is greater than the viscosity of water.



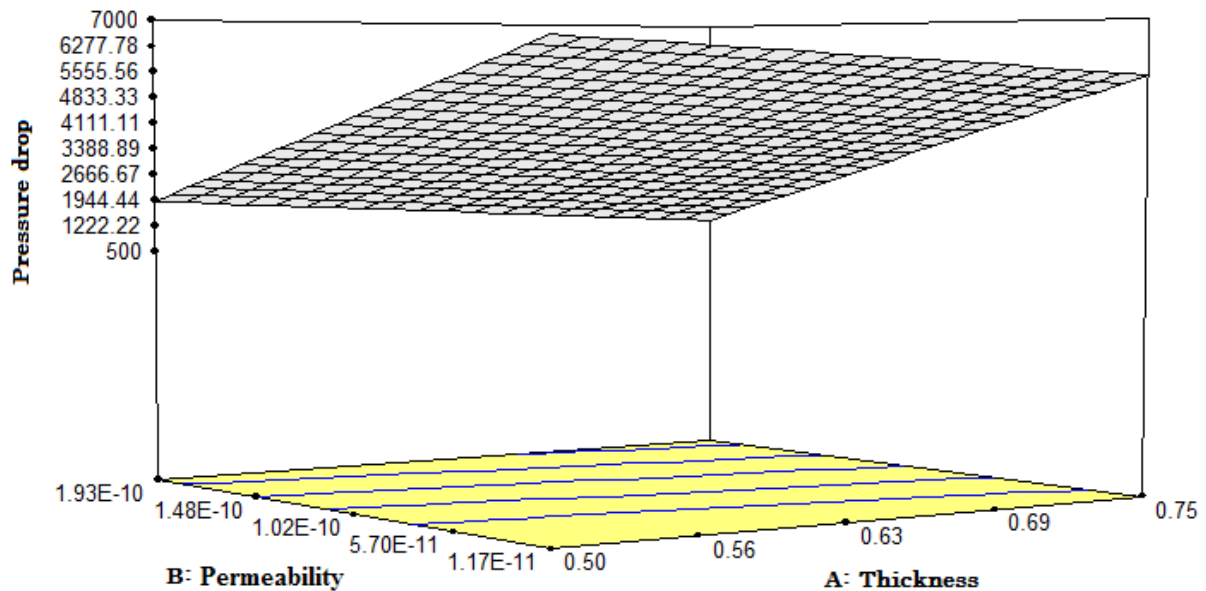
a) 3D surface plots of temperature difference (ΔT) as function of wick thickness and wick permeability when water is used as working fluid.



b) 3D surface plots of pressure drop as function of wick thickness and wick permeability when water is used as working fluid.



c) 3D surface plots of temperature difference (ΔT) as function of wick thickness and wick permeability when methanol is used as working fluid.



d) 3D surface plots of pressure drop as function of wick thickness and wick permeability when methanol is used as working fluid.

Figure 4. 3D surface for temperature difference (ΔT) and pressure drop (ΔP_1) as a function of wick thickness and wick permeability for the; (a) water- ΔT , (b) water- ΔP_1 , (c) methanol- ΔT , (d) methanol- ΔP_1

4.3. Optimization Results

In numerical optimization using D-optimal Design software, the wick permeability and wick thickness were goaled to be in range; the temperature differences and the pressure drop were aimed to be minimum. The optimization results yielded that a wick thickness of 0.52 mm and permeability of $1.39E-11 \text{ m}^2$ with water as working fluid could produce the minimum temperature difference of 9.56 °C and liquid pressure drop of 5730 Pa (less than about 833 Pa from the orginal pressure drop

6563 at the same heat input 35 W). These values commensurate with the experimental results of Elnaggar *et al.* [17]. Thus a model of good thermal performance of heat pipe with the proper pressure drop has been obtained which could increase the heat transport capability from 35 W to 43 W with about a 20% increase, where the values were confirmed by applying equation (2) in an analytical method.

The result of the optimization using D-optimal design software reveals that the performance of L-shape heat pipe in terms of heat transport capability is improved by 20%.

5. Conclusion

D-optimal designs software was performed to optimize the thickness and the permeability of wick structure with different working fluids of L-shape heat pipe for electronic devices cooling. The three significant parameters, wick thickness, wick permeability, and working fluids, are considered in this study with the objective of minimizing the temperature difference ΔT and liquid pressure drop ΔP_1 to get the best performance of the heat pipe. The optimization results yielded that a wick thickness of 0.52 mm and permeability of $1.39E-11 \text{ m}^2$ with water as working fluid could produce the minimum temperature difference of $9.56 \text{ }^\circ\text{C}$ and liquid pressure drop of 5730 Pa which increased the heat transport capability from 35 W to 43 W.

References

- [1] S.P. Ma, K.M. Park, W. Joung, and J. Lee, "Operating Characteristics of a Loop Heat Pipe with a Novel Flat Evaporator," 10th International Heat Pipe Symposium, Taipei, Taiwan, 2011.
- [2] Y.-W. Chang, C.-H. Cheng, J.-C. Wang, and S.-L. Chen, "Heat Pipe for Cooling of Electronic Equipment," *Energy Conversion and Management*. vol. 49, no. 11. 2008, 3398-3404.
- [3] R.A. Hossain, M.A.K. Chowdhuri, and C.M. Feroz, "Design, Fabrication and Experimental Study of Heat Transfer Characteristics of a Micro Heat Pipe," *Jordan Journal of Mechanical and Industrial Engineering*. vol. 4, no. 5. 2010, pp. 531-542.
- [4] M.H.A. Elnaggar, M.Z. Abdullah, and M. Abdul Mujeebu, "Characterization of Working Fluid in Vertically Mounted Finned U-Shape Twin Heat Pipe for Electronic Cooling," *Energy Conversion and Management*. vol. 62, 2012, pp. 31-39.
- [5] M.H.A. Elnaggar, "Numerical Investigation of Characteristics of Wick Structure and Working Fluid of U-Shape Heat Pipe for Cpu Cooling," *Microelectronics Reliability*. vol. 54, no. 1. 2013, pp. 297-302.
- [6] Elnaggar, "Development of Heat Pipe and Its Application in Electronic Cooling - a Comprehensive Survey," *Fundamental Journal of Thermal Science and Engineering*. vol. 3, no. 1. 2013, pp. 1-55.
- [7] J.H. Park, "A Study of Thermal Performance of Heat Pipe for Optimum Placement of Satellite Equipment," *ETRI Journal*. vol. 19, no. 2. 1997, pp. 59-70.
- [8] H.-K. Noh and K.-S. Song, "Temperature Distribution of a Low Temperature Heat Pipe with Multiple Heaters for Electronic Cooling," *ETRI Journal*. vol. 20, no. 4. 1998, pp. 380-394.
- [9] H. Xie, M. Aghazadeh, and J. Toth, "The Use of Heat Pipes in the Cooling of Portables with High Power Packages-a Case Study with the Pentium Processor-Based Notebooks and Sub-Notebooks," in *Electronic Components and Technology Conference, 1995. Proceedings.*, 45th. 1995. p. 906-913.
- [10] H. Xie, A. Ali, and R. Bhatia, "The Use of Heat Pipes in Personal Computers", *The Sixth Intersociety Conference on Thermal and Thermomechanical Phenomena in Electronic Systems, ITherm '98*. Seattle, WA, 1998, 442-448.
- [11] M. Seok Hwan, Y. Ho Gyeong, H. Gunn, and C. Tae Goo, "Experimental Study on the Performance of Miniature Heat Pipes with Woven-Wire Wick," *IEEE Transactions on Components and Packaging Technologies*, vol. 24, no. 4. 2001, pp. 591-595.
- [12] V. Wuttijumnong, T. Nguyen, M. Mochizuki, K. Mashiko, and Y. Saito, "Overview Latest Technologies Using Heat Pipe and Vapor Chamber for Cooling of High Heat Generation Notebook Computer," in *Semiconductor Thermal Measurement and Management Symposium, Twentieth Annual IEEE*, 2004, 221-224.
- [13] T.S. Liang and Y.M. Hung, "Experimental Investigation on the Thermal Performance and Optimization of Heat Sink with U-Shape Heat Pipes," *Energy Conversion and Management*. vol. 51, no. 11. 2010, pp. 2109-2116.
- [14] J.C. Wang, H.-S. Huang, and S.-L. Chen, "Experimental Investigations of Thermal Resistance of a Heat Sink with Horizontal Embedded Heat Pipes," *International Communications in Heat and Mass Transfer*. vol. 34, no. 8. 2007, pp. 958-970.
- [15] J.C. Wang, "Novel Thermal Resistance Network Analysis of Heat Sink with Embedded Heat Pipes," *Jordan Journal of Mechanical and Industrial Engineering*. vol. 2, no. 1. 2008, pp. 23-30.
- [16] M.H.A. Elnaggar, M.Z. Abdullah, and M. Abdul Mujeebu, "Experimental Analysis and Fem Simulation of Finned U-Shape Multi Heat Pipe for Desktop PC Cooling," *Energy Conversion and Management*. vol. 52, no. 8-9. 2011, pp. 2937-2944.
- [17] M.H.A. Elnaggar, M.Z. Abdullah, and S.R.R. Munusamy, "Experimental and Numerical Studies of Finned L-Shape Heat Pipe for Notebook-Pc Cooling," *IEEE Transactions on Components, Packaging and Manufacturing Technology*, vol. 3, no. 6. 2013, pp. 978-988.
- [18] M.H.A. Elnaggar, M.Z. Abdullah, and M.A. Mujeebu, "Experimental Investigation and Optimization of Heat Input and Coolant Velocity of Finned Twin U-Shaped Heat Pipe for Cpu Cooling," *Experimental Techniques*. vol. 37, no. 6. 2011, 34-40.
- [19] Z. Uddin and M. Kumarib, "Mhd Heat and Mass Transfer Free Convection Flow near the Lower Stagnation Point of an Isothermal Cylinder Imbedded in Porous Domain with the Presence of Radiation," *Jordan Journal of Mechanical and Industrial Engineering*. vol. 5, no. 5. 2011, pp. 419 - 423.
- [20] M.H.A. Elnaggar, "The Effect of Thickness and Permeability of Wick Structure on L-Shape Heat Pipe Performance Using Different Working Fluids," *Frontiers in Heat Pipes*. vol. 3, no. 4. 2013, pp. 1-7.
- [21] F. Kreith and M.S. Bohn, *Principles of Heat Transfer*, Brooks/Cole, Pacific Grove, CA, USA, 2001.

Numerical Study of the Hydrodynamic Structure of a Water Savonius Rotor in a Test Section

Ibrahim Mabrouki *, Zied Driss , Mohamed Salah Abid

Laboratory of Electro-Mechanic Systems (LASEM), National School of Engineers of Sfax (ENIS), University of Sfax, B.P. 1173, Road Soukra km 3.5, 3038 Sfax, TUNISIA.

Received 18 Feb 2014

Accepted 18 Jun 2014

Abstract

Turbulent free surface flows are encountered in many hydraulic and water resources engineering problems. Their understanding is thus a critical prerequisite for designing stream and river restoration projects and a broad range of hydraulic structures. For this purpose, a volume of fluid (VOF) advection algorithm, coupled with the Reynolds averaged Navier-Stokes (RANS) equations with a two-equation turbulence closure model, is employed. For efficiently describing and predicting the degree of turbulence in dam-break flows, the computations are carried out with the variation of initial turbulence intensities. From this investigation, it was found that the power performances of a Savonius water turbine were changed with the distance between the rotor and the bottom wall of the tunnel and with a rotation direction of the rotor.

© 2014 Jordan Journal of Mechanical and Industrial Engineering. All rights reserved

Keywords: CFD, VOF, Turbulence, Hydrodynamic, Savonius Rotor, Water Turbine

1. Introduction

The Savonius vertical axis water turbine is simple in structure, has good starting characteristics, relatively low operating speeds, and an ability to accept water from any direction. However, has a lower efficiency than some other vertical axis water turbines. So far a number of experimental investigations have been carried out to study the performance of the Savonius rotor. Due to the problems of the conventional sources of energy, like the depletion of its resources and environmental pollutions, great efforts are made towards the use of renewable energy sources. Hydraulic energy is considered one of the most important renewable energy sources because of its availability, simplicity and economy. Water rotors are the main tools of hydraulic energy. Savonius water rotor is one of the simplest and cheapest vertical axis water turbines. It is constructed from two vertical half cylinders and has good starting characteristics, relatively low operating speeds and ability to capture water from any direction. In fact, the performance of Savonius rotor has been widely studied by many researchers in order to determine its optimum design parameters. The effect of the blade aspect ratio, the blade overlap, the end plates, and the shielding were tested by Alexander and Holownia [1]. They concluded that there was an improvement in the rotor performance after increasing the aspect ratio and rotor overlap ratio. The tests of three and four bladed geometries gave appreciably lower values of efficiency than the two blades rotor. Roth [2] and Modi *et al.* [3] reported that the

optimum values of aspect and overlap ratios are 0.77 and 0.25, respectively. Mojola [4] concluded that the effect of overlap ratio on rotor performance depends on its tip speed ratio. Most of hydropower is generated by a large-scale hydroelectric plant. Some have suggested that dam constructions can lead to tremendous environmental damages. On the other hand, small/micro/nano hydropower has attracted much attention in the recent years mainly because of the decrease of construction place for large-scale plants and environmental conservation.

There have been many studies on a Savonius wind rotor, e.g., rotor configurations, a flow field around rotor numerical simulations and others [5]. The advantages of Savonius rotor using for the hydropower are little complex constitution, low cost, durability and easy maintenance. Although the previous studies give us useful information, problems of Savonius hydraulic turbine, used for the hydropower, are still unclear [6]. Fujisawa and Gotoh [7] have conducted experimental studies by flow visualization techniques, such as smoke wires. The studies of the smoke-wire method revealed variations in the flow around the rotor with rotor angle, but only qualitative information could be obtained. Measurements of the pressure distribution on the blade surfaces were carried out by Fujisawa [8], which provided some help in understanding the flow phenomena revealed by the flow visualization studies.

According to these anterior studies, there is a lack of detailed descriptions of the field for different types of Savonius rotors. Thus, the present paper aims at numerically exploring the three-dimensional unsteady flow

* Corresponding author. e-mail: : mabroukiibrahim@hotmail.fr.

over a conventional Savonius type rotor. It is thought that this approach could lead to a cheaper power generation without the environmental disruptions, compared with that produced by the large-scale hydroelectric plant.

2. Numerical Model

2.1. Geometrical Arrangement

Figure 1 shows the geometrical arrangement of the test section bench with an obstacle. The water turbine is placed on the test section at the point defined by $x=4$ m, $y=-0.8$ m and $z=0.7$ m. In these conditions, the test section is reduced from $L_1=0.4$ m to $L_2=0.2$ m. The turbine is equipped by two cylindrical buckets with a height equal to $H=0.1$ m and a diameter $D=0.1$ m.

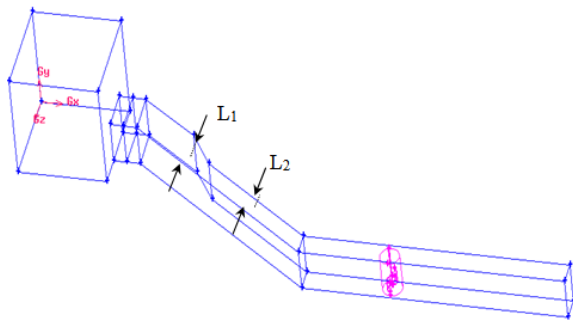


Figure 1. Geometrical arrangement.

2.2. Meshing

Figure 2 presents the meshing of the test bench with obstacle. It consists of 170426 nodes and 924170 cells. A tetrahedral hybrid is used as a type of cells for the meshing.

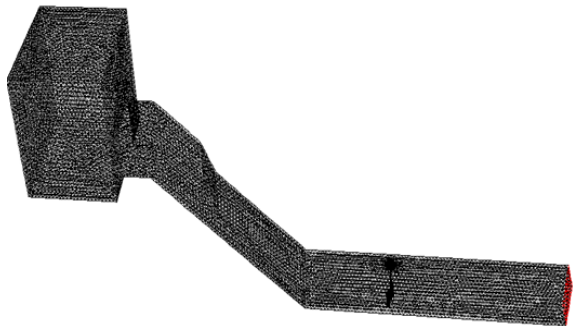


Figure 2. Meshing.

2.3. Boundary Condition

Figure 3 illustrates the boundary conditions using the commercial CFD code "FLUENT". The control volume, consisting of the intake, the penstock and the test section, is limited by "wall" condition. The control gate, located at the outlet of the intake, is modeled by an interior surface which will be removed at the instant $t=0$ s to start the water flow through the test bench. However, we impose the out flow condition in the test section. For the turbine, we have used the MRF model in order to approach the hydrodynamic behavior. A rotative speed equal to 500 rpm is imposed.

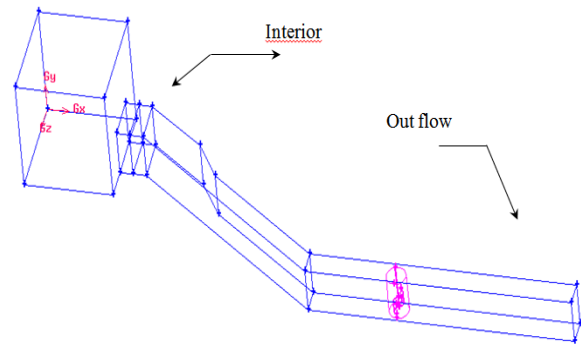


Figure 3. Boundary conditions.

2.4. MRF Model

The Multiple Reference Frame (MRF) model is the simplest of the three approaches for modeling problems that involve both stationary and moving zones. It is a steady-state approximation in which individual cell zones move at different rotational speeds. This approach is appropriate when the flow, at the boundary between these zones, is nearly uniform. While the multiple reference frame approach is clearly an approximation, it can provide a reasonable model of the time-averaged flow for many applications. When the relative velocity formulation is used, velocities in each sub domain are computed relative to the motion of the sub domain. Velocities and velocity gradients are converted from a moving reference frame to the absolute inertial frame as described below.

The position vector relative to the origin of the zone rotation axis is defined as:

$$\vec{r} = \vec{x} - \vec{x}_0 \quad (1)$$

Where \vec{x} is the position in absolute cartesian coordinates and \vec{x}_0 is the origin of the zone rotation axis. The relative velocity in the moving reference frame can be converted to the absolute (stationary) frame of reference using the following equation:

$$\vec{v} = \vec{v}_r + (\vec{\omega} \times \vec{r}) + \vec{v}_t \quad (2)$$

Where \vec{v} is the velocity in the absolute inertial reference frame, \vec{v}_r is the velocity in the relative non inertial reference frame, and \vec{v}_t is the translational velocity of the non inertial reference frame.

Using this definition of absolute velocity, the gradient of the absolute velocity vector is given by:

$$\nabla \vec{v} = \nabla \vec{v}_r + \nabla (\vec{\omega} \times \vec{r}) \quad (3)$$

3. Mathematical Formulation

3.1. Navier Stocks Equations

The governing equations for a Newtonian fluid are:

Conservation of Mass:

$$\frac{\partial \rho}{\partial t} + \frac{\partial \rho \vec{v}_i}{\partial x_i} = 0 \quad (4)$$

Conservation of momentum:

$$\frac{\partial \rho \tilde{u}_i}{\partial \tau} + \frac{\partial \rho \tilde{u}_j \tilde{u}_i}{\partial x_j} = \frac{\partial}{\partial x_j} \left(\mu \frac{\partial \tilde{u}_i}{\partial x_j} \right) - \frac{\partial \tilde{p}}{\partial x_i} + \rho g_i + \tilde{s}_{ui} \quad (5)$$

Where:

ρ : Density of fluid.

τ : Viscous stress.

u_i : Cartesian component of velocity in the direction x_i .

μ : Molecular kinematic viscosity.

k : Turbulent kinetic energy.

g_i : Gravitational acceleration.

The turbulent flow field is characterized by velocity fluctuations in all directions and has an infinite number of scales (degrees of freedom). Solving the Navier–Stocks equations for a turbulent flow is impossible because the equations are elliptic, non-linear and coupled (pressure-velocity, temperature-velocity). One of the solutions is to reduce the number of scales by using the Reynolds decomposition. Any property (whether a vector or a scalar) can be written as the sum of an average and a fluctuation:

$$\tilde{\phi} = \Phi + \phi \quad (6)$$

where the capital letter denotes the average and the lower case letter denotes the fluctuation of the property. Of course, this decomposition will yield a set of equations governing the average flow field. The new equations will be exact for an average flow field, not for the exact turbulent flow field. By an average flow field, we mean that any property becomes constant over time. The result of using Reynolds decomposition in the Navier–Stocks equations is called the Reynolds Averaged Navier Stokes equations (RANS). For each variable, we substitute the corresponding decomposition and we obtain the following RANS equations upon substitution of the Reynolds decomposition.

3.2. Standard k-ε Model

The standard k-ε model, developed by Launder and Spalding, is a two-equation eddy viscosity turbulence model. In this model, the turbulent viscosity is computed based on the turbulence kinetic energy k , and the turbulence dissipation rate ε :

$$\mu_t = C_\mu \frac{k^2}{\varepsilon} \quad (7)$$

Each of these two turbulence scales has its transport equation. The turbulence kinetic energy equation k is derived from the exact momentum equation by taking the trace of the Reynolds stress. This equation can be expressed as:

$$\frac{\partial k}{\partial t} + \bar{u}_i \frac{\partial k}{\partial x_i} = \nu_t \left[\frac{\partial \bar{u}_i}{\partial x_j} + \frac{\partial \bar{u}_j}{\partial x_i} \right] \frac{\partial \bar{u}_i}{\partial x_j} + \frac{\partial}{\partial x_i} \left(\frac{\nu_t}{\sigma_k} \frac{\partial k}{\partial x_i} \right) - \varepsilon \quad (8)$$

The dissipation rate equation, on the other hand, is obtained using physical reasoning. This equation can be expressed as:

$$\frac{\partial \varepsilon}{\partial t} + \bar{u}_i \frac{\partial \varepsilon}{\partial x_i} = C_{\varepsilon 1} \frac{\varepsilon}{k} \nu_t \left[\frac{\partial \bar{u}_i}{\partial x_j} + \frac{\partial \bar{u}_j}{\partial x_i} \right] \frac{\partial \bar{u}_i}{\partial x_j} + \frac{\partial}{\partial x_i} \left(\frac{\nu_t}{\sigma_\varepsilon} \frac{\partial \varepsilon}{\partial x_i} \right) - C_{\varepsilon 2} \frac{\varepsilon^2}{k} \quad (9)$$

These values were obtained using experiments and computer optimization. It is worth noting that these values are not universal and the k-ε model requires some amount of fine tuning in order to obtain correct results.

3.3. Volume of Fluid (VOF)

If one defines motions of the interface using a volume fraction field, the resulting VOF equation is described as:

$$\frac{\partial}{\partial t} \int_{\Omega} \alpha \, d\Omega + \int_S \alpha v \cdot n \, dS = 0 \quad (10)$$

Here, the density and viscosity are determined on the basis of the level-set function as:

$$\rho(\phi) = H(\phi) \rho_l + (1-H(\phi)) \rho_g \quad (11)$$

$$\mu(\phi) = H(\phi) \mu_l + (1-H(\phi)) \mu_g \quad (12)$$

Where the subscripts l and g denote the liquid and the gas respectively, ρ is the density, μ is the molecular kinematic viscosity. If the level-set construction process for considering surface tension effects is unnecessary, the local density and viscosity of the fluid can be defined using the volume fraction instead of the level-set function as follows:

$$\rho(\alpha) = \alpha \rho_l + (1-\alpha) \rho_g \quad (13)$$

$$\mu(\alpha) = \alpha \mu_l + (1-\alpha) \mu_g \quad (14)$$

Instead of the ULTIMATE-QUICKEST scheme, which is used in the CICSAM for the boundedness of the volume fraction distribution, we propose a less complicated and lower-order scheme $2\tilde{\alpha}_D = \tilde{\alpha}_f$, that is one basis element of the HRIC's bounded DD scheme. After enforcing the CBC for explicit flow calculations blended with the Hyper-C scheme, the proposed high resolution scheme can be rewritten as follows:

$$\tilde{\alpha}_f(\text{HRIC}) = \begin{cases} \min(\tilde{\alpha}_D C_0 + 2 \tilde{\alpha}_D (1 - C_0), \\ \tilde{\alpha}_D \end{cases} \quad (15)$$

$$\tilde{\alpha}_f(\text{Hyper-C}) \left. \begin{array}{l} \text{where } 0 \leq \tilde{\alpha}_D \leq 1 \\ \text{elsewhere} \end{array} \right\}$$

To achieve the balance between the smoothness and sharpness of the interface, we need a blending function that switches gradually between the Hyper-C and our proposed high resolution scheme. For this, we implement the following weighting factor, which is based on the orientation of the interface and the flow direction:

$$\gamma_f = \cos^4(\theta_f) \quad (16)$$

Where:

$$\theta_f = \arccos \left| \frac{(\nabla \alpha)_f \cdot n_f}{|(\nabla \alpha)_f| |n_f|} \right| \quad (17)$$

n_f is the vector connecting the centers of the CV, D and A. We use a blending function of higher degree than in the CICSAM. This is defined as:

$$\gamma_f = 0.5(\cos(2\theta_f) + 1) = \cos^2(\theta_f) \quad (18)$$

The normalized cell face value for the volume fraction computed by using the proposed high resolution advection scheme is defined as:

$$\tilde{\alpha}_f = \gamma_f \tilde{\alpha}_f^{(Hyper-C)} + (1 - \gamma_f) \tilde{\alpha}_f^{(HRIC)} \quad (19)$$

4. Numerical Results

4.1. Volume Fraction

Figure 4 presents the distribution of the volume fraction of water for the test section bench with obstacle in the x-y plane. According to these results, a decrease of the water height in the intake during the flow was noticed. The impact of water front with the turbine is very aggressive. In fact, this impact is due to the higher flow velocity created through the penstock. Also, the water front applies an important strength on the turbine blade, which is converted to the important torque and it becomes able to start the rotative motion of the turbine. In these conditions, the behavior of the water around the

turbine can be observed at the instant t=1.504 s, which is characterized with an important turbulence phenomena.

4.2. Average Velocity

Figure 5 presents the average velocity in the x-z plane of the test bench section with obstacle, for different instances of the water flow. According to these results, it has been observed that the average velocity has a very weak value in the intake during the flow. When the water flow ahead's through the penstock until the turbine, an increase of the velocity distribution is observed. A wake zone was created near the turbine during the flow and it reaches a higher value after impacting the water turbine. In addition, a gradient of velocity appeared between the two blades of the turbine. The velocity gradient increases in value especially at the instance t=1.504 s. Also, it has been noted that the aim of air is located in the roof of the penstock and the test section. The velocity value increases with the ahead of water through the test section.

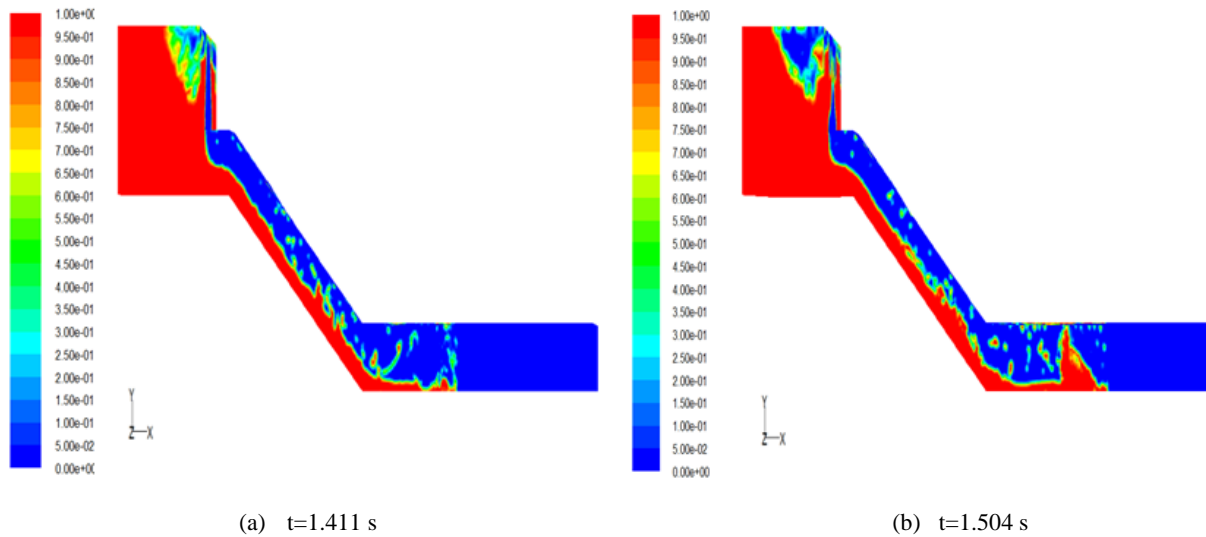


Figure 4. Distribution of the volume fraction in the x-y plane

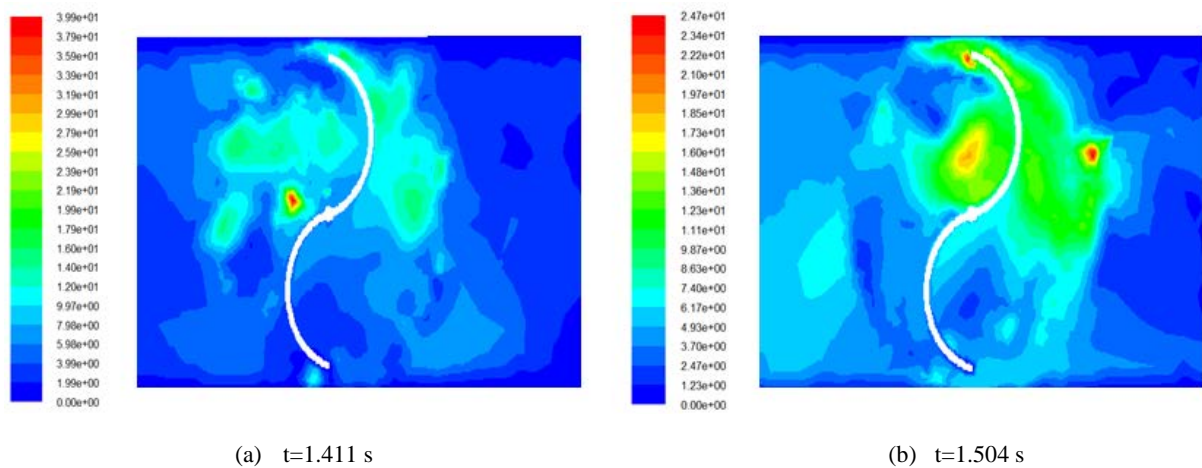


Figure 5. Distribution of the average velocity in the x-z plane

4.3. Velocity Vectors

Figures 6 and 7 present the distribution of the velocity vectors in the test section bench in the x-y plane, and around the turbine in the x-z plane, for different instances of water flow. According to these results, it has been noted that the flow velocity is very weak in the intake. A circulation zone of the air was created in the upstream of the turbine. Indeed, the water's velocity increases near and around the turbine. This fact is due to the turbulence phenomena, which decrease in the turbine downstream.

4.4. Static Pressure

Figures 8 and 9 show the distribution of the static pressure in the test bench with obstacle in the x-y plane,

and around the turbine in the x-z plane. In these condition, it has been noted that the static pressure is measured relatively to the atmospheric pressure. According to these results, it has been noted that the static pressure has a uniforme value through the test bench section. Also, the static pressure value has a weak value. This fact can ameliorate the hydrodynamic behavior of the test bench section. In addition, a compression zone located near the blade of the turbine buckets has been observed. The compression zone has an important value when the water flow impacts the turbine at $t=1.411$ s. However, it decreases the ahead of the water front through the test section. The zone around the turbine has a uniforme value, which is very important. In fact, the increase of the static pressure is due to the rotation velocity of the turbine.

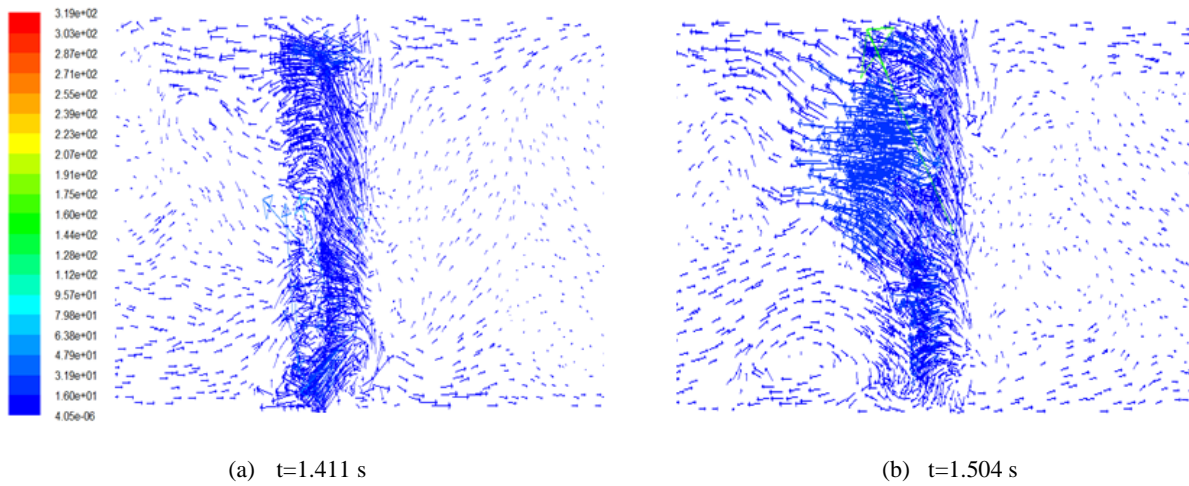


Figure 6. Distribution of the velocity vectors in the x-y plane.

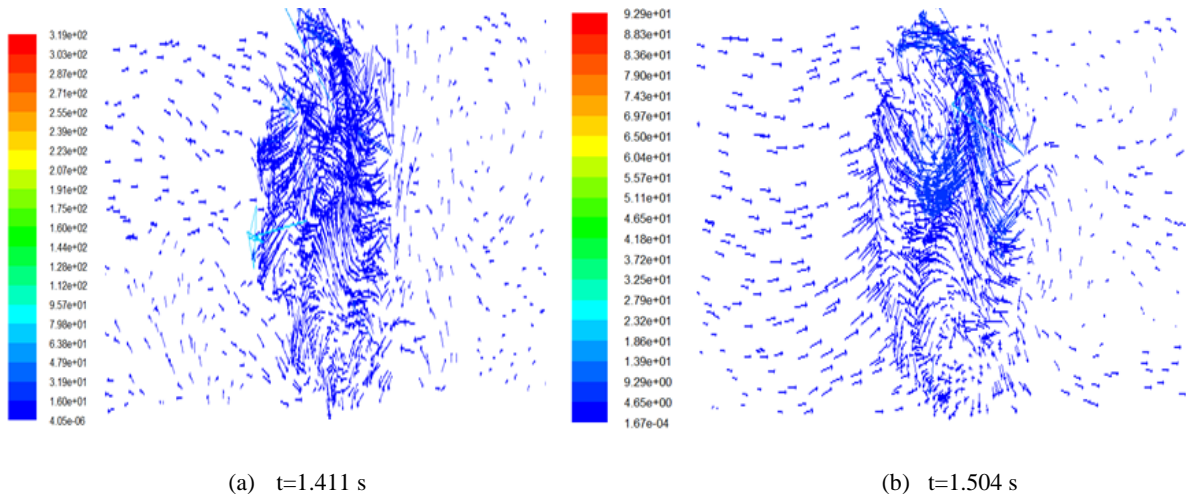


Figure 7. Distribution of the velocity fields in the x-z plane.

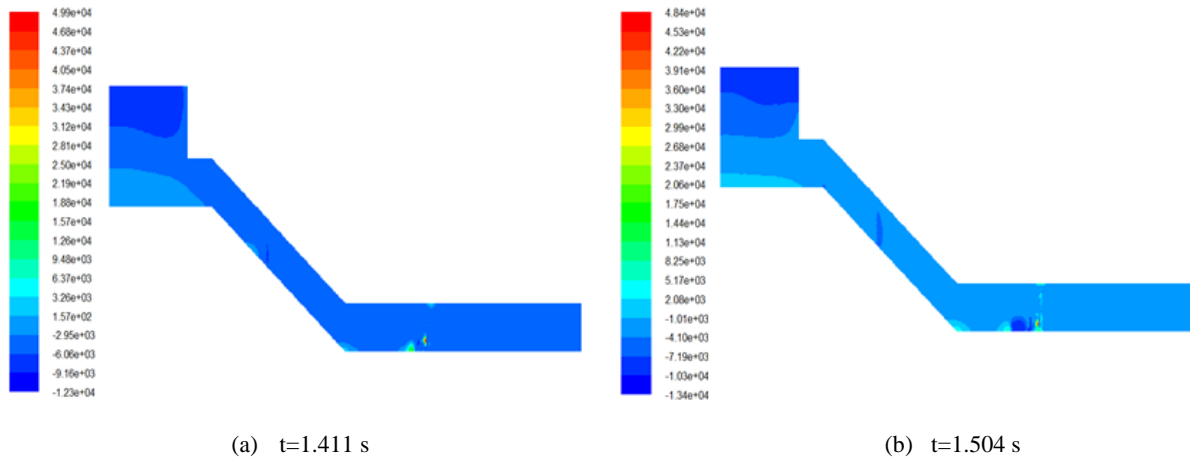


Figure 8. Distribution of the static pressure in the x-y plane.

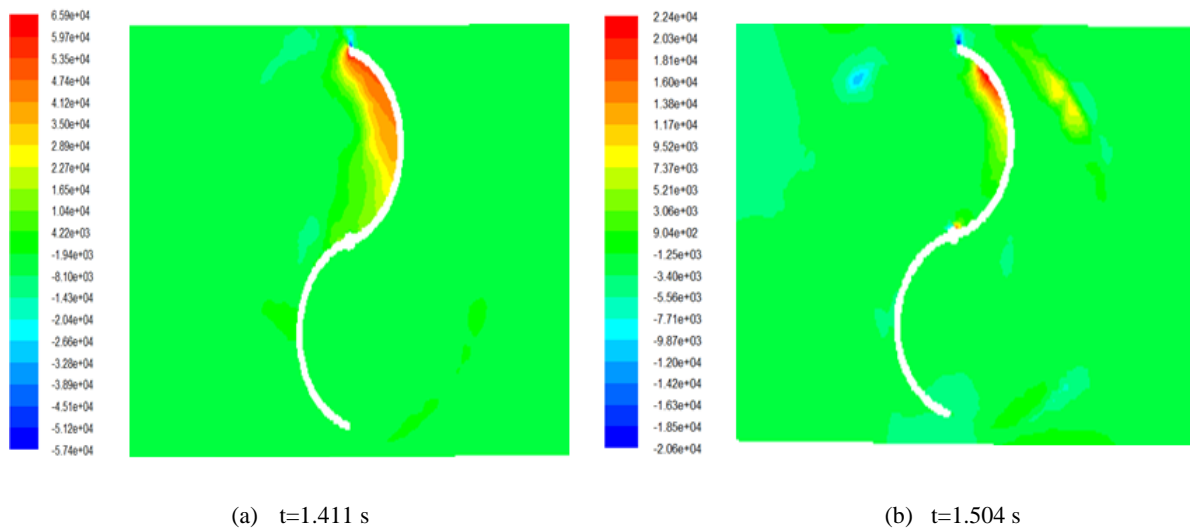


Figure 9. Distribution of the static pressure in the x-z plane.

4.5. Dynamic Pressure

Figure 10 shows the distribution of the dynamic pressure on the test bench section in the x-z plane for different instances of the flow. According to these results, it has been noted that the dynamic pressure is uniform in the intake and in the penstock at $t=1.504$ s. It increases after impacting the turbine. A compression

zone was created near the blade of the turbine. This zone increases in value and area extension, after the water flows ahead through the turbine. The maximum value of dynamic pressure reaches $p=94800$ Pa, which is able to put the turbine on rotation motion. Indeed, it has been noted that the zone around the turbine has an important value. In fact, the penstock ameliorates the water flow behavior of the turbine.

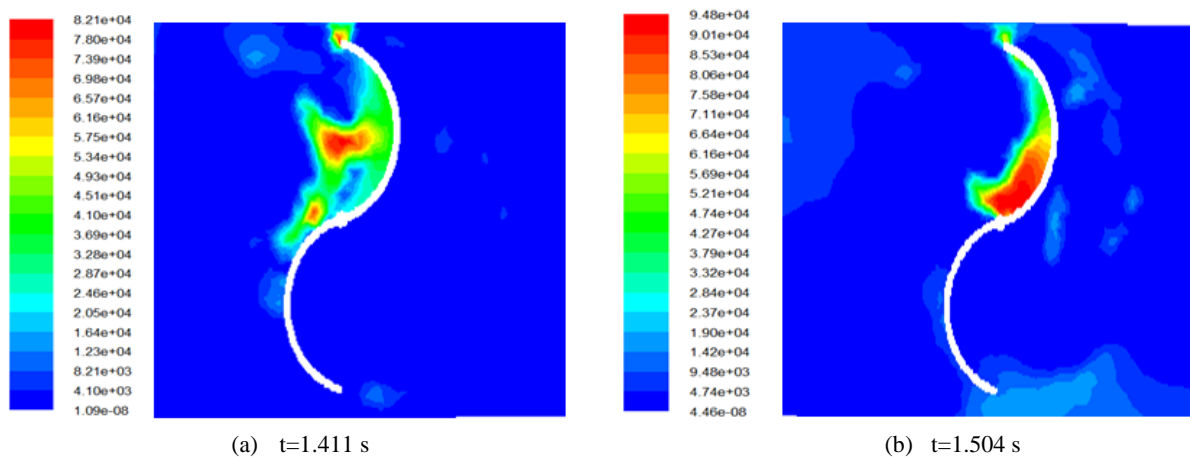


Figure 10. Distribution of the dynamic pressure in the x-z plane.

4.6. Turbulent Kinetic Energy

Figure 11 shows the distribution of the turbulent kinetic energy for the test section bench with obstacle in the x-z plane. According to these results, it has been noted that the turbulent kinetic energy is uniform in the penstock and the test section. However, a wake zone characteristic of the maximum values appears around the turbine. This zone is located between the upstream and the downstream of the turbine during the water flow. The zone extension decreases during the ahead of the water flow through the test section.

4.7. Turbulent Dissipation Rate

Figure 12 shows the distribution of the turbulent dissipation rate in the test section bench with obstacle in the x-z plane. According to these results, it has been noted that the turbulent dissipation rate presents the same distribution with those of the turbulent kinetic energy. Indeed, a very low value of the turbulent dissipation rate

in the penstock and in the test section has been observed. This value is uniform in the flow field. However, a variation of the turbulent dissipation rate values appears around the turbine. This fact is due to the turbulence phenomena created around the turbine and the friction of water with the wall of the test section bench.

4.8. Turbulent Viscosity

Figure 13 presents the behavior of the turbulent viscosity in the test section bench in the x-y plane and around the turbine in the x-z plane for different instances of water flow. According to these results, wake zone characteristics of the maximum values of the turbulent viscosity appear in the middle of the intake, which decreases in value during the flow. Also, the variation of the turbulent viscosity has been observed near the turbine bucket. At $t=1.504$ s, a wake zone, located in the downstream of the turbine, has been observed, with a maximal value equal to 6.64 Pa.s.

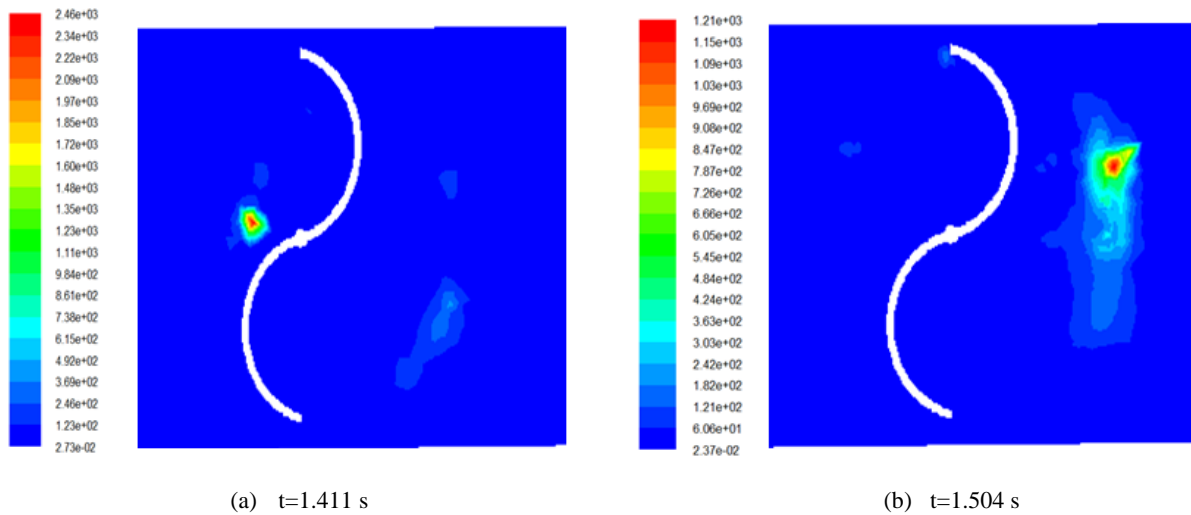


Figure 11. Distribution of the turbulent kinetic energy in the x-z plane.

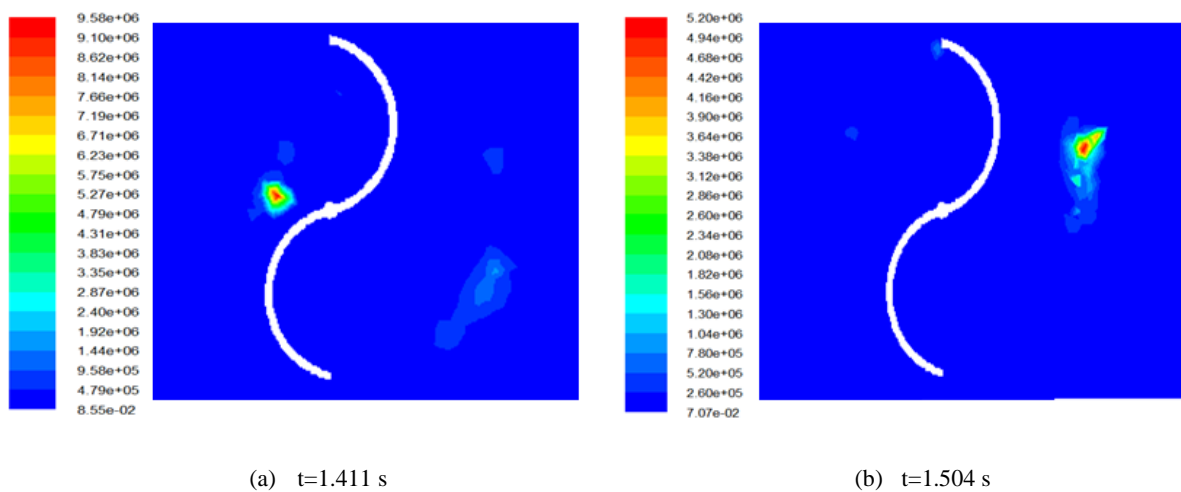


Figure 12. Distribution of the turbulent dissipation rate in the x-z plane.

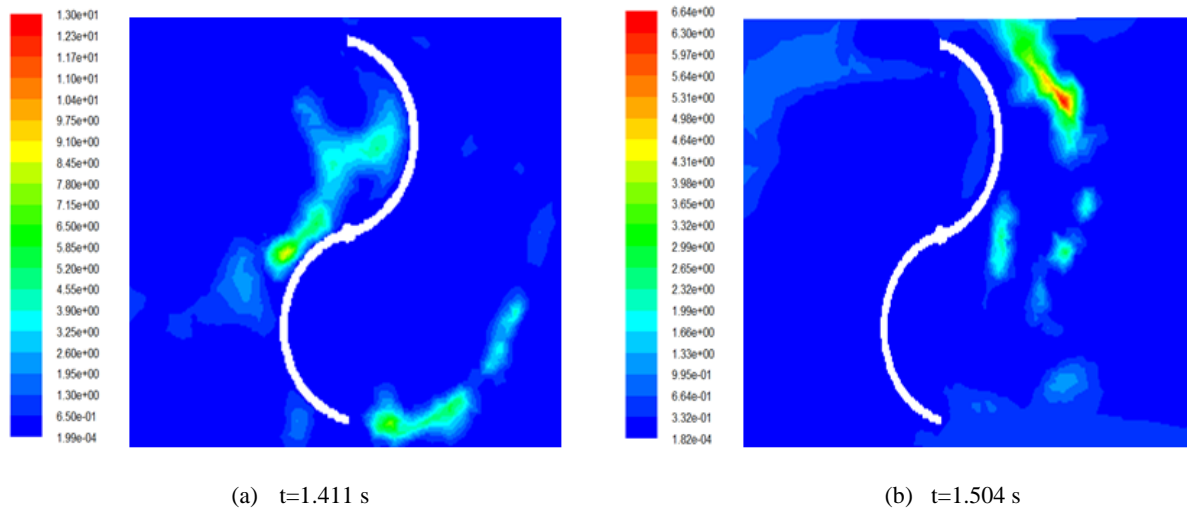


Figure 13. Distribution of the turbulent viscosity in the x-z plane.

4.9. Vorticity

Figure 14 shows the distribution of vorticity in the test section bench in the x-z plane for different instances of flow. According to these results, it has been noted that the value of vorticity is uniform along the penstock and the test section, and it is very low during the water flow. However, a wake zone characteristics of the maximum values of the vorticity appear around the turbine.

4.10. Comparison with Experimental Results

Figures 15 and 16 compare the numerical results obtained by the commercial CFD code “FLUENT”, for

the test section bench with obstacle and equipped with turbine, with the experimental results obtained from the test section bench. The comparison between the numerical and the experimental results consists on the curves which present the free surface and the water front of the flow. According to these results, the ahead of the flow through the test section and the impact between the water front and the turbine has been observed. The comparison was carried out for the validation of our numerical model for these cases. In fact, the comparison shows an acceptable agreement between the experimental and the numerical results. The gap between the results is about 6%.

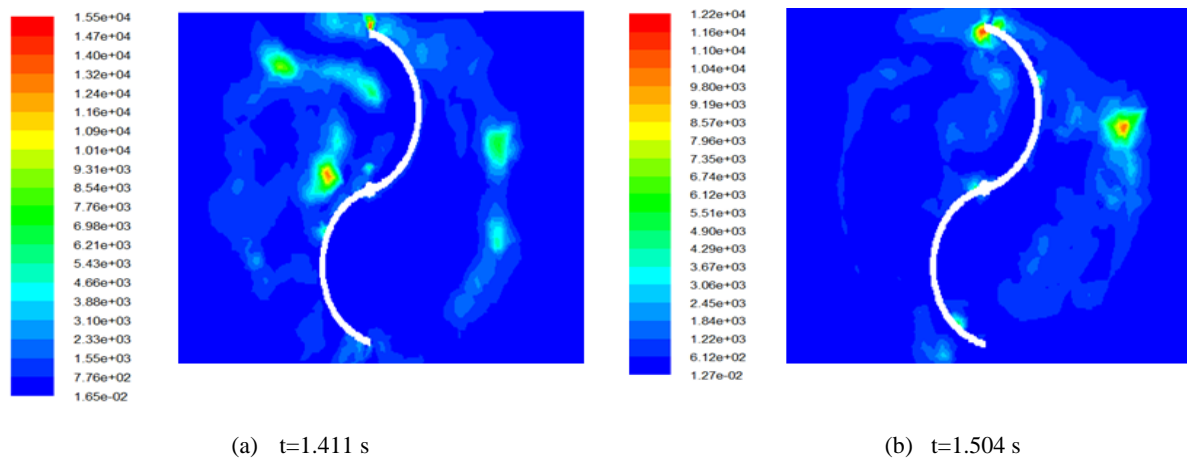


Figure 14. Distribution of the vorticity in the x-z plane.

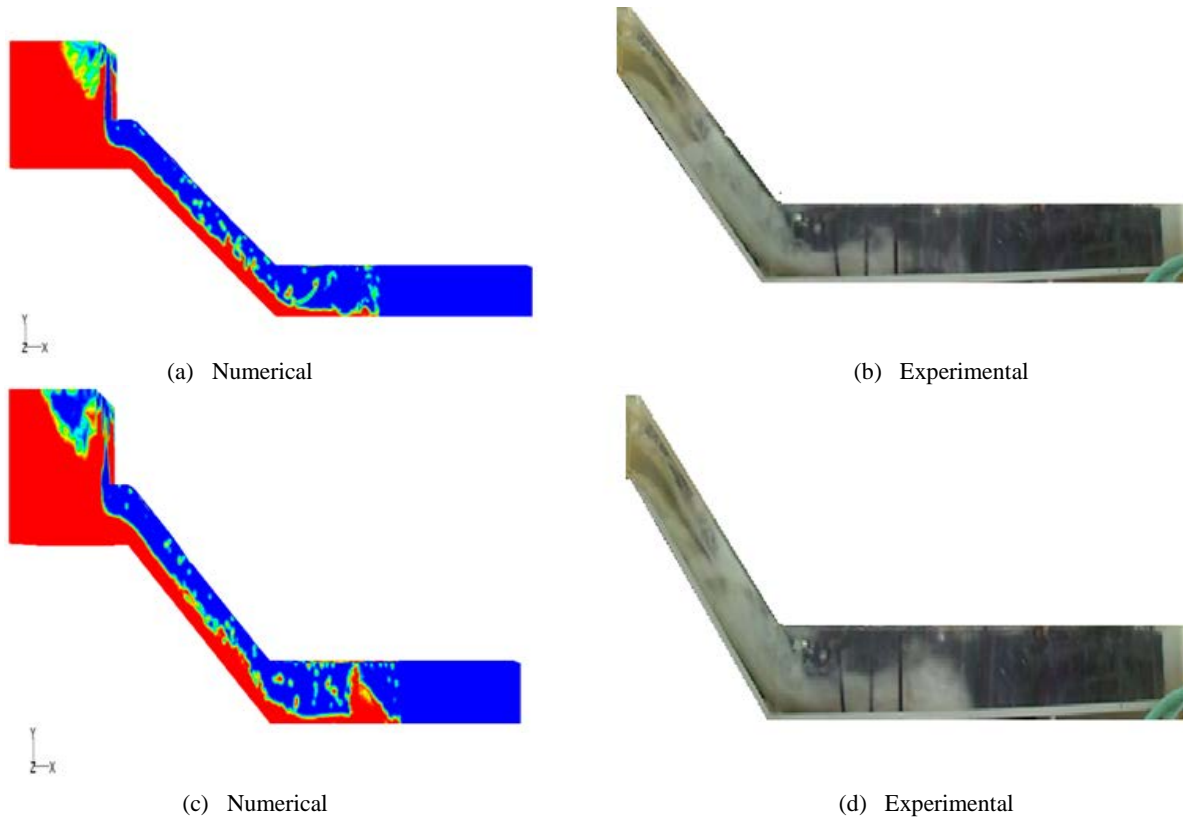


Figure 15. Comparison of the volume fraction with experimental results.

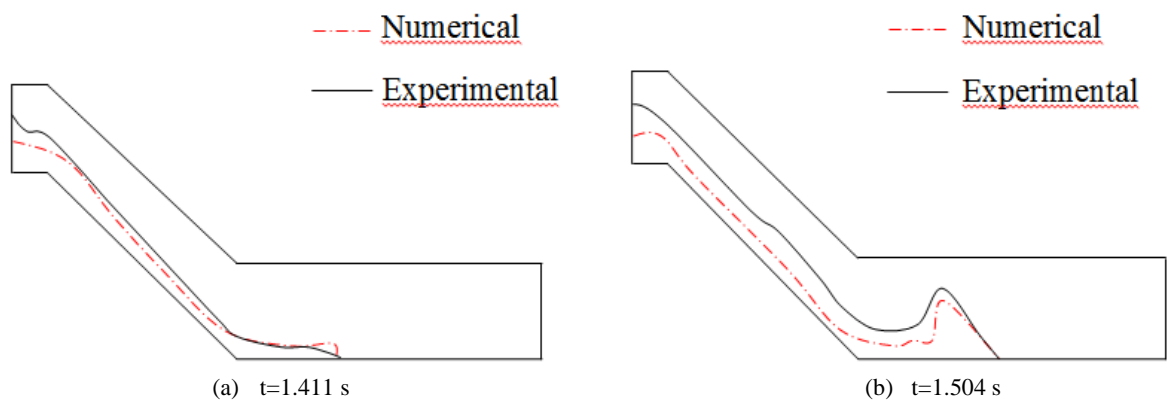


Figure 16. Comparison between numerical and experimental results.

5. Conclusion

The present study explored the non-linear of three dimensional unsteady potential flows over water Savonius rotor to hopefully develop a simulation method for predicting its hydrodynamic performance. The performance of cross-flow water turbines of the Savonius type, for very low head hydropower applications, has been investigated after the CFD model validation. A model of a water Savonius turbine was constructed and tested in a water tunnel to arrive at an optimum installation condition. A flow field around the rotor was examined visually to clarify the influences of the installation conditions on the flow field. The flow visualization showed a difference in the flow pattern around the rotor by changing these

parameters. A decrease in the water height in the intake during the flow has been observed. The impact of water front with the turbine was very aggressive. This fact is due to the higher flow velocity created through the penstock. The velocity was increased in value simultaneously with the ahead of water through the water channel. Also, it has been noted that the turbulent of dissipation rate is due to the turbulence phenomena created around the turbine and the friction of water with the wall of the test section bench.

Acknowledgments

The authors would like to thank the Laboratory of Electro-Mechanic Systems (LASEM) members for financial assistance.

References

- [1] Alexander, A.J., Holownia, B.P., Wind tunnel tests on a Savonius rotor. *Journal of Industrial Aerodynamics* 3(1978), 343-351.
- [2] Roth, N.J., Prototype design and performance of Savonius rotor based on irrigation system (Thesis of Master Degree) University of British Columbia, 1982.
- [3] Modi, V.J., Roth, N.J., Fernando, M.S., Optimum-configuration studies and prototype design of a wind-energy-operated irrigation system. *Journal of Wind Engineering and Industrial Aerodynamics* 16 (1984), 85-96.
- [4] Mojola, O., on the aerodynamic design of the Savonius windmill rotor. *Journal of Wind Engineering and Industrial Aerodynamics* 21(1985), 223-231.
- [5] Bergeles, G. and Athanassiadis, On the Flow Field around a Savonius Rotor, *Wind Engineering*, Vol.6 (1982) No.3 140-148.
- [6] Ueno, H., Mino, M. and Takada, N., Savonius type wind turbine, Influence of a side plate, *Journal of Japan Solar Energy Society* (2002) 35-40.
- [7] Fujisawa N, Gotoh F. Visualization study of the flow in and around a Savonius rotor, *Experiments in Fluids*, 407-412, 1992.
- [8] Fujisawa N, On the torque mechanism of Savonius rotors, *Journal of Wind Engineering and Industrial Aerodynamics*, 277-292, 1992.
- [9] Fujisawa, N. and Taguchi, Y, Investigation of Flow Field around Savonius Rotors by Particle Imaging Velocimetry and Numerical Calculations, *Turbo machinery*, 439-447, 1995.
- [10] *J. Fluid Mech.* 374, 407-424.
- [11] Whitham, G.B, The effects of hydraulic resistance in the dam break problem. *Proc. R. Soc. London*, 399-407, 1955.
- [12] Violeau, D., Issa, R. Numerical modeling of complex turbulent free-surface flows with the SPH method: an overview. *Int. J. Numer. Methods Fluids* 53 (2007), 277-304.
- [13] I. Mabrouki, Z. Driss, and MS. Abid, "Experimental validation on the flow around a water Savonius rotor," *Troisième Congrès Tunisien de Mécanique, COTUME'2014*.

Studying the Design and Verification of 5-axis NC program under the Manufacturing System

Wang Zhun *

School of Mechanical and Automobile Engineering, Anhui Polytechnic University, Wuhu 241000, People's Republic of China

Received 18 Mar 2014

Accepted 10 Jun 2014

Abstract

NC programming, based on part profiles, is the conventional theory involved in the NC codes creating tasks; this is not wrong but far from satisfying the needs of the 5-axis NC cutting jobs. Viewing from the manufacturing system level and taking the transmission lower tank cut job on the 5-axis MC (machine center) as an example, the author deeply investigated and summarized the technique principles and algorithms of all works involved from a manufacturing system preparation to the 5-axis NC program verification with the help of computer aided technologies. The program design for the 5-axis NC machining is achieved with the CAM methods, and the correctness of the NC codes is guaranteed with the Post-NC verifying. All these principles and algorithms are general and practical, and can be applied by the 5-axis MC users to promote their production quality, efficiency and cost targets.

© 2014 Jordan Journal of Mechanical and Industrial Engineering. All rights reserved

Keywords: *5-axis NC Machining, Programming Algorithm under the Manufacturing System, Manufacturing System in Verification, Physical Manufacturing Status*

1. Introduction

Traditionally, NC programming is emphasized in part profile or graphic driving cutter [1, 2]. However, the 5-axis NC machining is a complicated procedure, and the NC programming should be finished with a full consideration of the machine tool, CNC, cutters and fixtures, namely the design of NC program should be done under the manufacturing system environment. The 5-axis NC machining codes can be achieved by means of the Computed Aided Manufacturing—CAM technologies.

There are a lot of books and articles concerning the software operations for each CAM platform both at home and abroad, but there is a little comparative research on the integrating Post-NC verification into NC program design using CAM. For this reason, the author studied some popular CAM platform and Post-NC verification strategies, and dug out the algorithms of 5-axis NC machining codes design and verifying.

2. Algorithm of NC Program Design under the Manufacturing System

2.1. NC Programming Workflow

The NC programming workflow is shown in Figure 1. Every manufacturing system (Figure 1, right side) component, such as the machine tool configuration (CNC and construction lay out), the cutters, and the fixture

should be fully considered in each step. The operation inf. is called from the manufacturing system. The middle part of Figure 1 shows how the associated information is transferred from the manufacturing system step by step, and how the final correct NC codes are schemed out.

2.2. The Machining Tasks and Manufacturing System Involved

The discussed 5-axis NC machining tasks are the rough cutting of the low tank - rough finishing all surfaces and holes, as shown in Figure 2.

To accomplish the jobs, the manufacturing system is designed as follows: the 5-axis HMC (Horizontal Machine Center (refer to Figure 8)), the fixture (refer to Figure 9), and the cutters. All the operation specifications are expressed in a different technique doc.; for example, the operation sheets, the cutter list, machine tool regulation sheets [3].

3. CAM and its Postprocessor

3.1. Jobs in the First 5 Steps

As shown in Figure 1, the preparatory work is done in the step 1 and step 2, and the key jobs are the determination of the workpiece dimensional orientation and the setting of the program coordinate system (PCS). Figure 3 shows the PCS setting in the CREO/CAM and

* Corresponding author. e-mail: CADCAM_246@126.com.

Catia/CAM [4, 5]. The greatest work capacity occurs in the 4th step: all the detailed operation specifications should be imported to CAM platform, such as the machining parameters, the cutters and their compensation codes, and the other specific work contents. The cutter vector driven mode should be carefully set up for the 5-axis NC machining in this stage. The result of the preceding step is testified in the 5th step; this is called 'pre-verification' before the NC cutting codes are created. Figure 4 shows the pre-verification circumstances (in CREO/CAM).

3.2. The Critical Tasks in the 6th Step

The NC codes are created by the postprocessor in the 6th stage. During this phase, the dedicated postprocessor must be created firstly, and it must then be called to generate the appropriate NC codes.

Three jobs are done during creating the postprocessor.

Firstly, the machine tool layout and technical specifications should be imported into the "Post Creator" (see the center in Figure1). The "PTC/GPost" [4] result is shown in Figure 5 and Figure 6. Secondly, the program format is to be set up, which involves the transformation of the cutter path into the CNC-based NC codes, for instance, the output format of RTCP (Rotation Tool Centre Point) in the 5-axis NC machining [6]. As for this research, the 5-axis HMC is equipped with Fanuc 15/16M which enables RTCP functions through the use of code G43.4 [7]. In the "Post Builder"[8] (as shown in Figure 7), a MOM (Manufacturing Output Manager) segment compiled with the TCL (Tool Command Language) is affixed to the "tool change block", because the code 'G43.4' should be called immediately after the cutter changing. Thirdly, the other specific settings (for example, the postprocessor register, the preserved directory, etc.) should be finished.

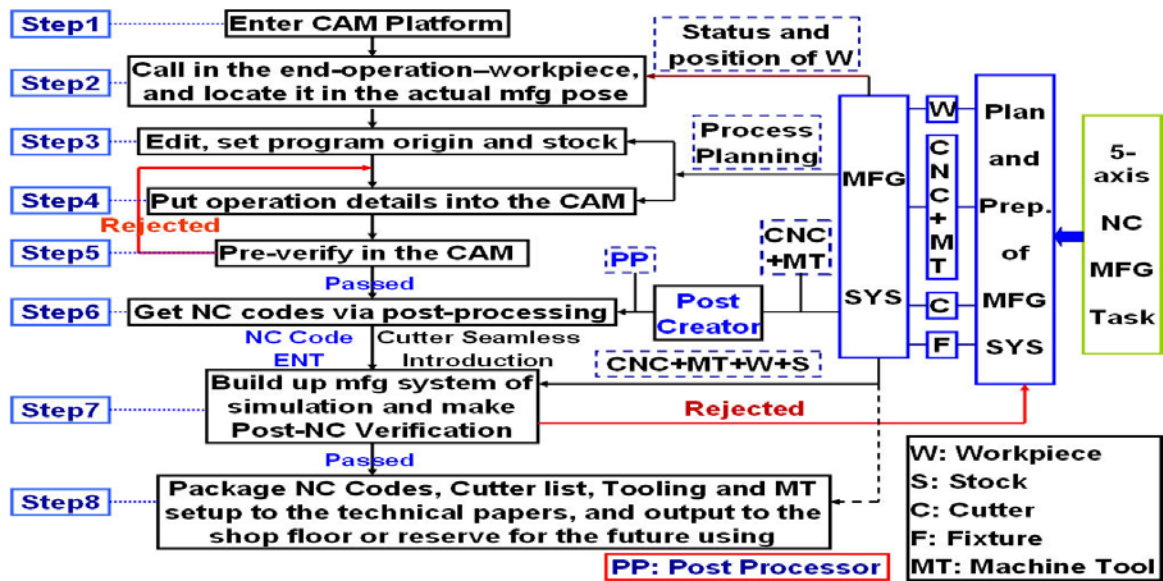


Figure 1. 5-Axis NC program design algorithm

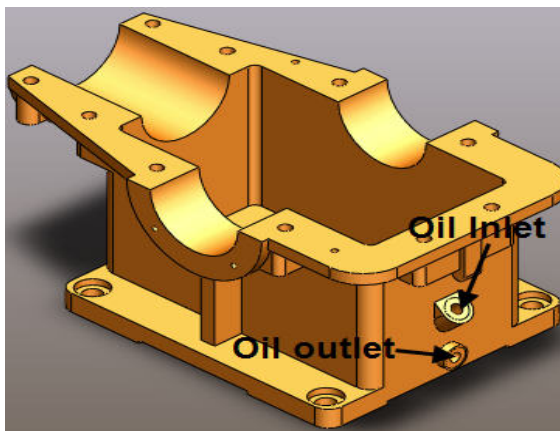


Figure 2. The lower tank of a transmission

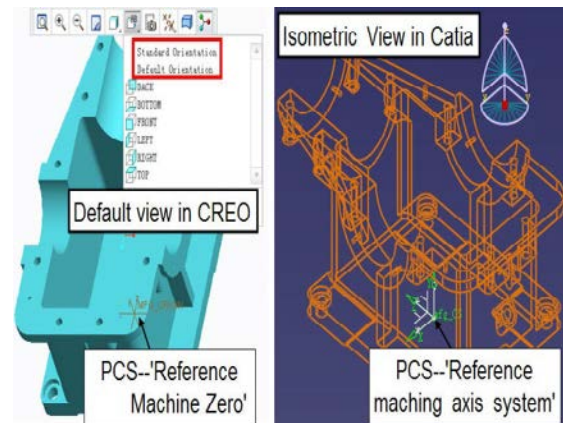


Figure 3. Setting of PCS in the 5-axis HMC

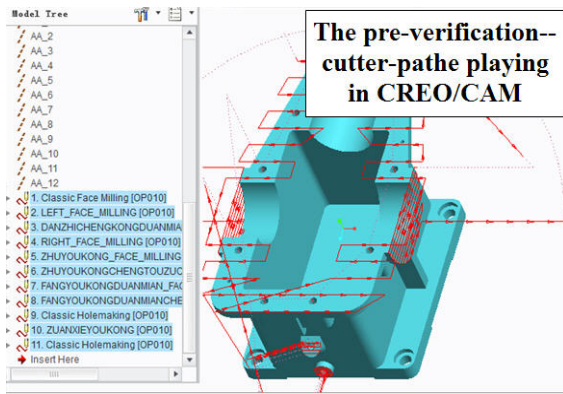


Figure 4. Pre-verification in CAM



Figure 5. Layout of the 5-axis HMC

4. Post-NC Verification under the Simulation Manufacturing System

4.1. Building up the Verification Manufacturing System

The certainty of the Post-NC verification is established on the fact that the “digital manufacturing system” totally represents the physical manufacturing status as much as possible. With the “manufacturing system”, the inherent feature and interrelation (especially, the spatial and relative motion relationship) of every element could not vary with the research stages or issues. The manufacturing system’s consistency throughout the different phases of the study is guaranteed by the bidirectional data transmission between the CAD/CAM platform and the verification package.

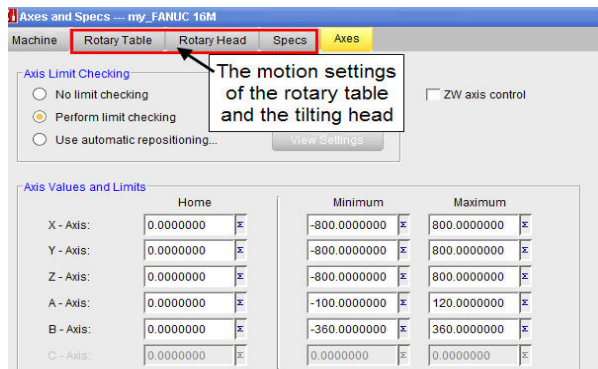


Figure 6. Technical specifications input

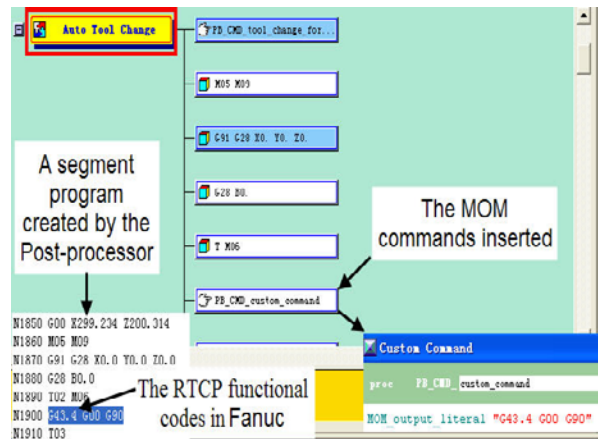


Figure 7. Output setting of the RTCP codes

The fixture and its interfacing with the worktable of a machine tool form into an “integrated manufacturing system”. So, the fixture should be developed based on the worktable [9]. As a consequence, the manufacturing system feature-model, created in different CAD platform, has the unified spatial position with its verification-model. The primary construction of the 5-axis HMC is shown in Figure 8 [6]. The worktable’s spatial relationship is shown in Figure 9 (left side). At the right side in Figure 9, there is the developed fixture with that associated worktable. Figure 10 shows the final manufacturing systems under the Post-NC verification platform-Vericut [10].

4.2. Start up the Manufacturing System and Execute the Verification

Several different running modes can be used to execute all kinds of simulations, such as uninterrupted running, pause at tool change, G codes running line-by-line, and so on. All the program errors could be checked out and eliminated by using a mix of these methods.

4.3. One Case of Postprocessor be Improved

In this research, the tool axis is on the slanting direction (45°) when the oil inlet (see Figure 2) is being cut, and the Post-NC verification shows that: the cutter vector is on the correct orientation, but, it feeds in and out as a Z-shape movement which results in gouge. In order to solve this problem, the researcher employed the line-by-line simulation mode and read the NC codes. He found that the troubles occurred at the code translation fulfilled by the postprocessor in which the two dimensional coordinate of the base points were represented into two program segments. The new code interpretation settings to the quick tool path are shown in Figure 11 (inside the “PTC/GPost”), and the NC codes, generated with the modified postprocessor, have proved to be of no kinematic errors in another Post-NC verification.

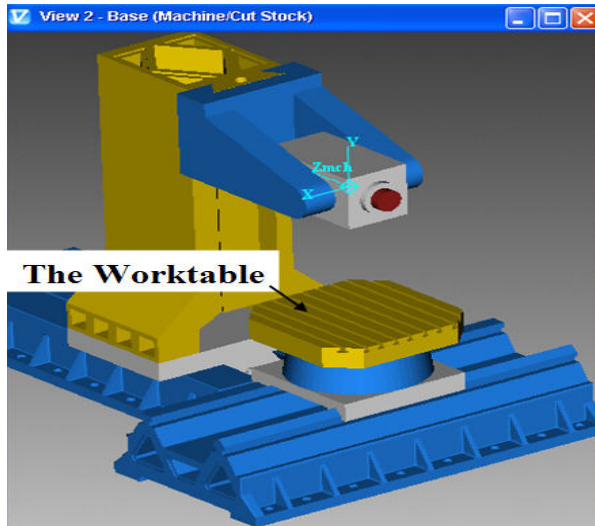


Figure 8. A 5-Axis HMC

4.4. One Case of Optimization to the NC Codes

In this study, when the top face and three side faces (refer to the Figure 2) are machined, the cutting and feeding parameters specified by the CAM are the fixed values, i.e., the machining parameters for all the 6 cut faces on the 4 different orientations (including the notches) are the constants. This will lead to extra machining time. When the NC programming is done based on the manufacturing system, the machine tool specifications, the workpiece materials, and the cutter materials have been considered. The “OptiPath” functional module of Vericut may be applied to resolve these problems [10], in which the empiric optimum cutting values about the materials of the cutter [11, 12], the materials of workpiece and the machine tool kinematic parameters are put into the module; the algorithm of “Volume Removal” or “Chips Thickness” is executed to obtain the optimum feed rates and spindle speeds, namely to get the optimum NC codes [13].

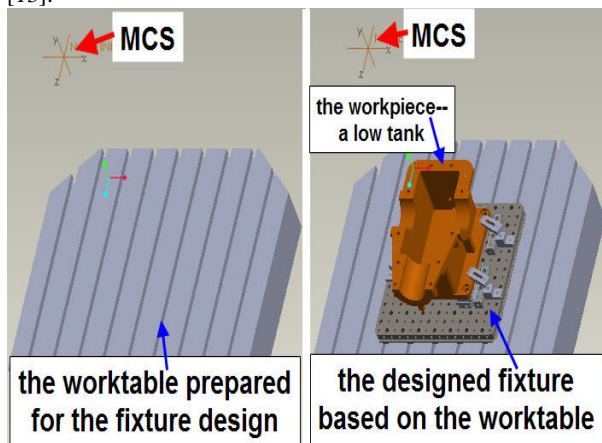


Figure 9. Worktable and designed fixture

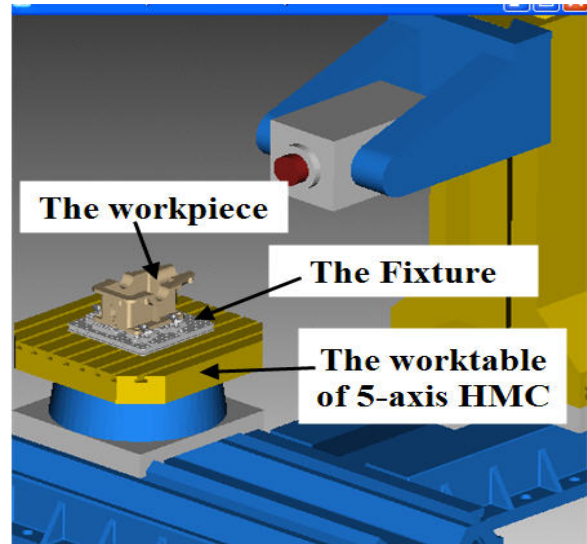


Figure 10. The final manufacturing systems

5. Summary

Taking the multi-directional machining on the 5-axis HMC as a case study and viewing from the manufacturing system, the researcher figured out the technical principles and algorithm involved in the program design and verification to the 5-axis NC machining. These approaches are of general purpose and can be applied to other types of 5-axis NC machining tasks. In addition, for the workpieces needing several set-ups, even requiring different machine tools to achieve multiple-operation, these principles and approaches can also be used to fulfill an integrated verification in order to estimate and correct all the potential design errors, which occur from the technological preparation to the field of machining. Moreover, the total manufacturing time may also be calculated out by the verification. All this effort contributes to the promotion of the quick response capability to market the modern enterprise.

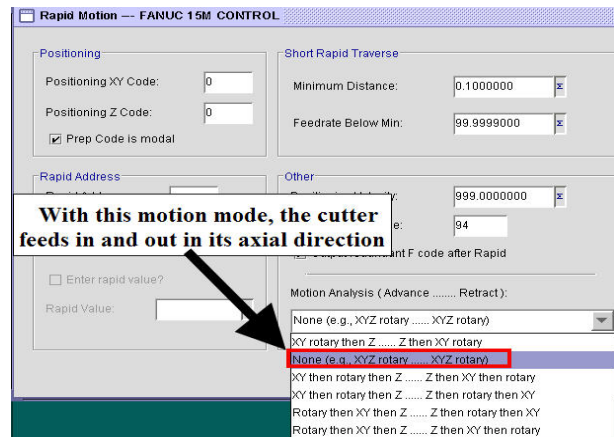


Figure 11. Appropriate setting of fast motion

Acknowledgment

This work is partly supported by the Professional Construction Foundation of China (No. TS10310.) and is also supported by the Professional Development Foundation of Anhui (No. 2012zy042).

References

- [1] Mike Mattson: CNC Programming principles and applications. 1st ed. ISBN: 7-111-15206-9. Beijing: China Machine Press; 2004.
- [2] Stanislav S. Makhanov, Weerachai Anotaipaiboon: Advanced Numerical Methods to Optimize Cutting Operations of Five-Axis Milling Machines. ISBN: 978-3-540-71120-9 (Print) 978-3-540-71121-6 (Online).
- [3] ZHAO Rufu: Handbook for Personnel of Metal Processing Planning. 4th ed. Shanghai: Shanghai Scientific and Technical Publishers; 2006 (in Chinese).
- [4] Information on <http://www.ptc.com>
- [5] Information on <http://www.3ds.com>
- [6] Wang Zhun: "Design method of five-axis MC based on integrating CAD platform with NC MFG verification software". Manufacturing Technology & Machine Tool, No. 1 (2013) 53–61 (in Chinese).
- [7] GE Fanuc Automation North America, Inc.: Series 15/150–Model B for Machining Center/Operator's Manual (Programming/ Operation). U.S.A : GE Fanuc Automation North America, Inc., (March 1997)
- [8] Information on <http://www.plm.siemens.com/zchn>
- [9] Adi Saptari, Wong Soon Lai, Mohd. Rizal Salleh: Jig Design, Assembly Line Design and Work Station Design and their Effect to Productivity. Jordan Journal of Mechanical and Industrial Engineering, Volume 5 (2011) Number 1, Pages 9 - 16
- [10] Information on <http://www.cgtech.com/cn>
- [11] Mohammed T. Hayajneh, Montasser S. Tahat, Joachim Bluhm: A Study of the Effects of Machining Parameters on the Surface Roughness in the End-Milling Process. Jordan Journal of Mechanical and Industrial Engineering, Volume 1 (2007) Number 1, Pages 1 - 5
- [12] B. Srinivasa Prasad, M. M. Sarcar: Analysis of Face Milling Operation Using Acousto Optic Emission and 3D Surface Topography of Machined Surfaces for In-Process Tool Condition Monitoring. Jordan Journal of Mechanical and Industrial Engineering, Volume 5 (2011) Number 6, Pages 509 - 519
- [13] Sylvain Lavernhe, Christophe Tournier, Claire Lartigue: Kinematical performance prediction in multi-axis machining for process planning optimization. Int J Adv Manuf Technol, No. 37(2008) 534–544.

Experimental Investigations on the Electrochemical Machining Characteristics of Monel 400 Alloys and Optimization of Process Parameters

^{1*}M.Kalaimathi, ¹G.Venkatachalam and ²M.Sivakumar

¹School of mechanical and building sciences, VIT University, Vellore-632014, TN, India

²Department of mechanical engineering, Sree Sowdambika College of engineering, Aruppukkottai-626134, TN, India

Received 17 Dec 2013

Accepted 16 Jun 2014

Abstract

Monel 400 alloys are used in various fields such as aerospace industries, marine industries, etc. It is very difficult to machine Monel 400 alloys using conventional machine tools. The Electrochemical Machining (ECM), an advanced manufacturing process, is a natural choice for machining Monel 400 alloys. The present work is carried out to investigate the influence of ECM process parameters, such as applied voltage (V), inter electrode gap (IEG) and electrolyte concentration (EC), on material removal rate (MRR) and surface roughness (Ra) during machining Monel 400 alloys. An aqueous sodium chloride (NaCl) is used as a basic electrolyte in the electrochemical machining of Monel 400 alloys. The experimental strategy is based on a response surface methodology. The effects of process parameters as well as their interactions are investigated and the process parameters are optimized through the desirability function of the response surface methodology. The microstructure of the Monel 400 alloys specimen, machined with ECM, is studied to understand the effect of electrolyte and other parameters during the machining.

© 2014 Jordan Journal of Mechanical and Industrial Engineering. All rights reserved

Keywords: Electrochemical Machining (ECM), Material Removal Rate (MRR), Surface Roughness (Ra), Monel 400 Alloys, Response Surface Methodology (RSM), Desirability Function (DF).

Nomenclature

V : Voltage between tool and work piece (V)
 IEG : Inter electrode gap between tool and work piece (mm)
 EC : Electrolyte concentration (grams per litre)
 MRR : Material removal rate (grams per minute)
 R_a : Surface roughness (μm)
 RSM : Response surface methodology
 CCD : Central composite design
 DF : Desirability function

1. Introduction

Electrochemical machining (ECM) is a non-contact metal removing process, which is used to shape the work piece by anodic dissolution process. ECM has traditionally been used in with difficult-to-cut materials and with complex geometry. A D.C. voltage (5-30 V) is applied across the IEG between pre-shaped cathode tool and an anode work piece. The electrolyte flows at a high speed through the IEG. The current density is usually 20 to 200 A/cm². The anodic dissolution rate, which is governed by Faraday's laws of electrolysis, depends on the

electrochemical properties of the metal, electrolyte properties and electric current/voltage supplied. ECM generates an approximate mirror image of the tool on the work piece [1]. The metal hydroxides and other by-products generated during the machining are removed from the gap by the high velocity of electrolyte flow. ECM process, a mechanical forceless machining with no thermally influenced machining zones, produces a high surface quality and low roughness. Tool design, pulsed current, micro-shaping and finishing, numerical control, environmental concerns and hybrid processes are very important in the utilization of the full potential of ECM [2]. The demand for the micro products and components of difficult-to-machine materials, such as tool steel, carbides, super alloys and titanium alloys, is rapidly increasing in automotive, aerospace, electronics, optics, medical devices and communication industries. These materials pose many challenges to conventional machining processes, such as turning and milling. Hence, it necessitates the machining of these materials with ECM. Advantages of ECM over other traditional machining processes include its applicability, regardless of material hardness, no tool wear, comparable high MRR, smooth and bright surface and the production of components of complex geometry with stress-free and crack-free surfaces [3]. ECM has been

* Corresponding author. e-mail: mkm1979@rediffmail.com

applied in many industrial applications including turbine blades, engine castings, bearing cages, gears, dies and moulds and surgical implants. ECM is also more suitable for large scale production.

Monel 400 alloy is an excellent alloy among all the commonly used nickel based alloys for its corrosion resistance and toughness. It is primarily used in industries such as nuclear, aerospace, missile, and marine. Monel alloys work hardens rapidly as it undergoes high strains during machining. This hardening effect slows further machining. Therefore, it is very difficult to machine these alloys using conventional machine tools. Tool failure is the common result in the machining of Monel 400 alloys with conventional methods due to the work hardening effect. ECM could therefore be a cost-effective alternative for Monel 400 alloys and could become more and more significant in the near future. Several works have been reported in the literature for machining of nickel based alloys using different non-conventional machining methods. The improvement in the machinability of nickel base and titanium alloys with ceramic tools was extensively analysed by Ezugwu *et al.* [4, 5]. Liu *et al.* studied the characterization of nickel alloy micro-holes using micro-EDM together with grinding [6]. Ulutan *et al.* analyzed machining induced surface integrity for titanium alloys and nickel-based alloys. Problems with residual stresses, white layer and work hardening layers, as well as micro-structural alterations were studied to improve surface qualities of end products [7]. Selvakumar *et al.* [8, 9] investigated the machining suitability of Monel 400 alloys with wire-cut electrical discharge machining (WEDM). Die corner accuracy and surface roughness of Monel 400 alloys were considered as responses; Selvakumar *et al.* [8, 9] also studied various WEDM process parameters' influence.

Significant attempts [10-13] have been made on machining of nickel based alloys. But all these machining methods, reported in the literature, result in the reduction of tool life including WEDM. But the machining suitability of Monel 400 alloys, with ECM process, is not widely reported in the literature. Hence, in the present

work, ECM has been used to study the machining characteristics of Monel 400 alloys. The aim of this work is to develop the comprehensive mathematical models for correlating the interactive and higher-order influences of the various machining parameters such as applied voltage (V), inter electrode gap (IEG) and electrolyte concentration (EC) on the prime machining performances, i.e., material removal rate (MRR) and surface roughness (R_a) for the effective utilization of the full potential of ECM. Response surface methodology (RSM) is employed to plan and analyze the experiments. The objective of using the RSM is not only to investigate the response over the entire factor space, but also to locate the region of the interest where the response reaches its optimum or near optimum value. By carefully studying the response surface model, the combination of the factors which gives the best response, can then be established [14]. RSM was implemented as an effective experimental strategy in end milling by Kadirgama *et al.* [15].

2. Experimentation

Schematic diagram of ECM set-up is shown in Figure 1. The process parameters, selected for the present investigation, are EC, V and IEG because of the significant influence on the ECM performances [16-19]. Their effects on the MRR and R_a are tested through the set of the planned experiments based on central composite design (CCD) of RSM. Table.1 shows the factors and their levels in coded and actual values. The levels of each factor were chosen as -2, -1, 0, 1, 2 in closed form to have a rotatable design. The coded values were obtained from the following equation:

$$X_i = \frac{\text{Chosen parametric values} - \text{Central rank of parameters}}{\text{Interval of variation}} \quad (1)$$

Where, X_i is the coded values of the variables IEG, V and EC, respectively.

The design requires 20 experiments for the three variables. The design was generated and analysed using DESIGN EXPERT statistical package.

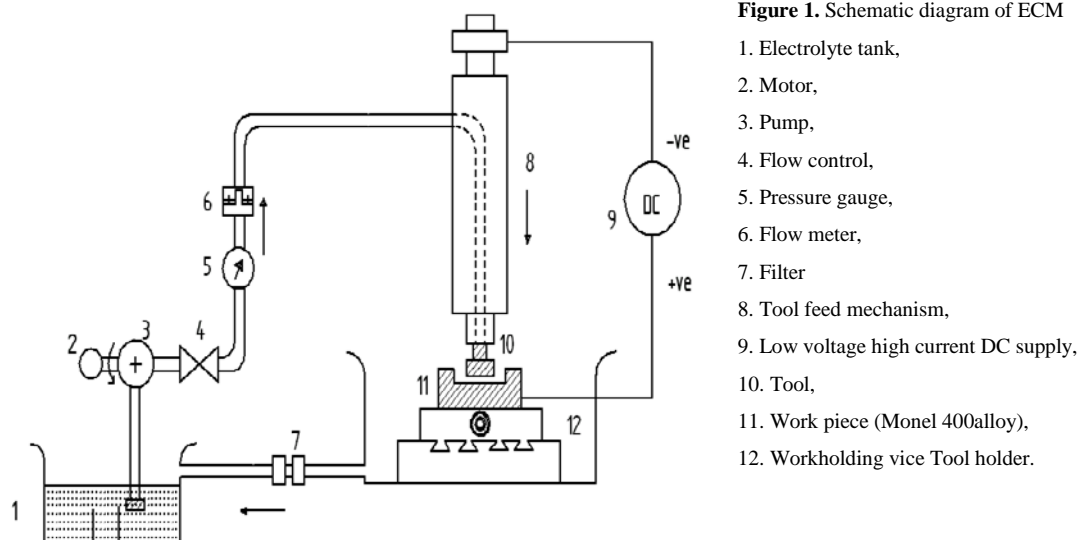


Figure 1. Schematic diagram of ECM

1. Electrolyte tank,
2. Motor,
3. Pump,
4. Flow control,
5. Pressure gauge,
6. Flow meter,
7. Filter
8. Tool feed mechanism,
9. Low voltage high current DC supply,
10. Tool,
11. Work piece (Monel 400alloy),
12. Workholding vice Tool holder.

Figure 2 shows a photographic view of the experimental apparatus of the ECM. Figure 3(a) and Figure 3(b) represent the 3D model and the cross sectional view of the tool used in this work. Commercially obtained Monel 400 alloys were used as a test specimen. The chemical composition (weight %) of Monel 400 alloys is as follows: C: 0.047, Si: 0.172, Mn: 1.03, P: 0.012, S: 0.01, Cr: 0.1, Mo: 0.1, Fe: 1.66, V: 0.029, W: 0.1, Cu: 29.24, Al: 0.01, Co: 0.103, Nb: 0.1, Ti: 0.047, Mg: 0.031, and Ni: 67.4.

Table 1. Process Parameters and their values at different levels

Symbol	Process parameters	Levels				
		-2	-1	0	1	2
X_1	Inter electrode gap, IEG (mm)	0.1	0.2	0.3	0.4	0.5
X_2	Voltage, (V)	10	15	20	25	30
X_3	Electrolyte concentration, EC (grams per litre)	100	130	160	190	220



Figure 2. Electrochemical machining set-up

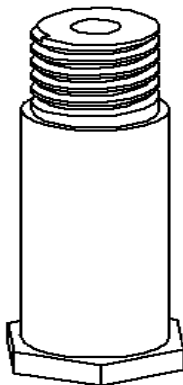


Figure 3. (a) 3D model of tool

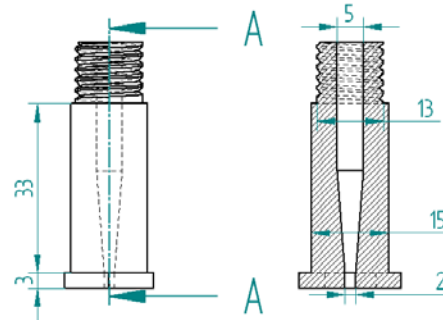


Figure 3. (b) Cross sectional view of tool

The MRR and R_a were observed for a various set of experiments with a different combination of process parameters based on RSM. Using RSM, a comprehensive mathematical model is developed for correlating the interactive and higher-order influences of various machining parameters on the dominant machining criteria, i.e., the MRR and the surface roughness (R_a). The general second order polynomial response surface mathematical model, which analyses the parametric influences on the various response criteria, is given below:

$$Y_u = b_o + \sum_{i=1}^n b_i X_{iu} + \sum_{i=1}^n b_{ii} X_{iu}^2 + \sum_{j>i}^n b_{ij} X_{iu} X_{ju} + e_u \quad (2)$$

Where Y_u represents the corresponding response, i.e., MRR and R_a of the ECM process in the present work. The value n indicates the number of machining parameters. The terms b_i , b_{ii} , b_{ij} are the second order regression coefficients. The second term under the summation sign of this polynomial equation attributes to the linear effects and the fourth term of the equation represents the interactive effects of the parameters. The collection of experimental data adopts the CCD in order to fit the quadratic model of y_u . The experiment has been carried out according to the designed experiment based on CCD which is illustrated in Table 2.

In this work, MRR was measured based on weight loss during machining time:

$$MRR = \frac{LW}{MT} \text{ grams per minute} \quad (3)$$

Where, LW-Loss of weight, i.e., weight difference of work piece before and after machining in grams
MT-Machining time in minutes.

Weights were measured using Sartorius (BS 423S) balance with an accuracy of 0.001g. The surface roughness (R_a) value is the indicator of the technical surface quality of an engineering product. In this work, R_a was measured using the Mitutoyo (SJ-201) surface roughness tester with a sampling length of 10 mm. Roughness measurements, in the transverse direction, on the work pieces were repeated three times and the average of the three measurements of surface roughness(R_a) values was recorded.

Table 2. Experimental observation

Exp. No.	Inter electrode gap (IEG)		Voltage (V)		Electrolyte concentration (EC)		MRR (grams/minute)	R _a (μm)
	Coded X ₁	Actual (mm)	Coded X ₂	Actual (V)	Coded X ₃	Actual (grams/litre)		
1	-1	0.2	1	25	-1	130	0.577	2.02
2	0	0.3	0	20	0	160	0.458	1.79
3	1	0.4	-1	15	-1	130	0.395	2.78
4	0	0.3	0	20	0	160	0.495	1.97
5	1	0.4	1	25	1	190	0.617	2.82
6	-1	0.2	-1	15	1	190	0.294	1.23
7	0	0.3	0	20	0	160	0.494	2.13
8	0	0.3	0	20	2	220	0.381	1.27
9	-2	0.1	0	20	0	160	0.563	1.27
10	0	0.3	0	20	-2	100	0.527	2.37
11	0	0.3	2	30	0	160	0.620	3.50
12	0	0.3	-2	10	0	160	0.417	2.19
13	2	0.5	0	20	0	160	0.504	2.45
14	0	0.3	0	20	0	160	0.451	1.82
15	0	0.3	0	20	0	160	0.518	1.91
16	0	0.3	0	20	0	160	0.518	1.82
17	1	0.4	-1	15	1	190	0.322	2.05
18	-1	0.2	1	25	1	190	0.585	2.22
19	-1	0.2	-1	15	-1	130	0.492	1.35
20	1	0.4	1	25	-1	130	0.402	2.76

3. ANOVA Analysis

The analysis of variance is performed for the model adequacy checking, which includes a test for the significance of the regression model, model coefficients and lack of fit. ANOVA is mainly carried out to analyse the variation among the groups. This is done by *F-test* at 95% confidence level. Significance and insignificance are determined by comparing the *F-values* with standard tabulated values at the corresponding degrees of freedom and 95% confidence level. The values of "Prob > F" less than 0.05 indicates that the model and its terms are significant. The values which are greater than 0.1 indicate that the model terms are not significant[14].

3.1. Material Removal Rate (MRR)

The quadratic model is statistically significant for the analysis of MRR. The details of ANOVA for the response surface quadratic model along with the partial sum of squares on MRR are given in the Table 3.

The *F-value* of the source "Model" 7.91 implies that the model is significant. This means that the regression model provides an excellent explanation of the relationship between the factors and the MRR. In this case, *V*, *IEG*EC*, *V*EC* are significant model terms. The lack of fit "*F-value*" 3.84 is less than the tabulated value, which means that the developed model is adequate.

Table 3. ANOVA for response surface quadratic model of MRR

Source	Sum of Squares	DF	Mean Square	F Value	Prob > F	Significance
Model	0.140 00	9	0.016 00	7.91	0.001 7	significant
IEG	0.006 84	1	0.006 84	3.41	0.094 6	
V	0.077 00	1	0.077 00	38.18	0.000 1	
EC	0.007 31	1	0.007 31	3.64	0.085 4	
IEG ²	0.001 43	1	0.001 43	0.71	0.418 3	
V ²	0.000 62	1	0.000 62	0.31	0.589 6	
EC ²	0.003 80	1	0.003 80	1.90	0.198 5	
IEG*V	0.000 70	1	0.000 70	0.35	0.567 4	
IEG*EC	0.014 00	1	0.014 00	6.91	0.025 2	
V*EC	0.030 00	1	0.030 00	15.00	0.003 1	
Residual	0.020 00	10	0.002 01			
Lack of Fit	0.016 00	5	0.003 18	3.84*	0.083 1	not significant
Pure Error	0.004 15	5	0.000 83			
Total	0.160 00	19				

F_{0.05(5,5)}=5.05,*Not significant

Table 4. ANOVA for response surface quadratic model of surface roughness(R_a)

Source	Sum of Squares	DF	Mean Squares	F Value	Prob>F	Significance
Model	6.220 00	9	0.690 00	18.13	< 0.000 1	Significant
IEG	2.220 00	1	2.220 00	58.14	< 0.000 1	
V	1.580 00	1	1.580 00	41.50	< 0.000 1	
EC	0.490 00	1	0.490 00	12.80	0.005 0	
IEG ²	0.001 35	1	0.001 35	0.035	0.854 7	
V ²	1.430 00	1	1.430 00	37.43	0.000 1	
EC ²	0.007 54	1	0.007 54	0.20	0.666 1	
IEG*V	0.100 00	1	0.100 00	2.71	0.130 9	
IEG*EC	0.069 00	1	0.069 00	1.81	0.208 3	
V*EC	0.150 00	1	0.150 00	3.99	0.073 8	
Residual	0.380 00	10	0.038 00			
Lack of Fit	0.300 00	5	0.059 00	3.54*	0.095 7	not significant
Pure Error	0.084 00	5	0.017 00			
Cor Total	6.600 00	19				

$F_{0.05}(5,5)=5.05$, *Not significant

The suitable regression model for the response MRR is given below:

$$MRR = 2.2427 - 2.0515 * IEG - 0.04595 * V - 0.01305 * EC + 0.01387 * IEG * EC + 0.00041 * V * EC \quad (4)$$

(Coefficient of determination $R^2=0.70$)

3.2. Surface Roughness(R_a)

The quadratic model is statistically significant for the analysis of surface roughness. The details of ANOVA for the response surface quadratic model along with the partial sum of squares on surface roughness are given in the Table 4:

The model F-value of 18.13 implies the model is significant. In this case, IEG, V, EC, V^2 are significant model terms. The "Lack of Fit F-value" of 3.54 implies there is a 9.57% chance that a "Lack of Fit F-value" which is due to noise.

The second order polynomial equation for R_a is fit as shown below:

$$R_a = 3.8174 + 13.661 * IEG - 0.3973 * V - 0.00876 * EC + 0.00953 * V^2 - 0.22725 * IEG * V - 0.03096 * IEG * EC + 0.001 * V * EC \quad (5)$$

This model can be used to navigate the design space.

4. Results and Discussion

4.1. Parametric Influence on MRR

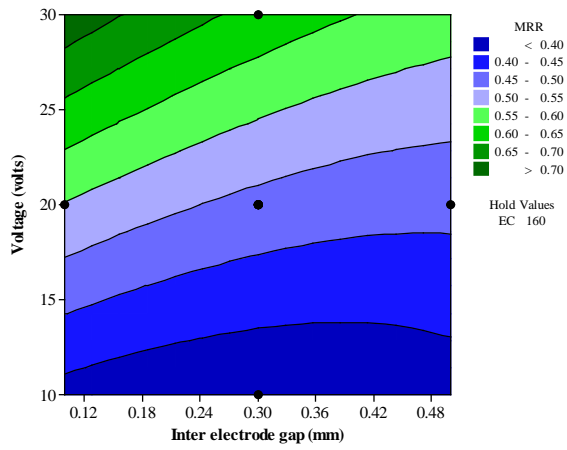
Based on the mathematical model (Eq. 4) which is developed through the CCD of the response surface methodology, the effect of the various process parameters' influence on the MRR has been analyzed. The contour

plots were drawn for various combinations of influencing parameters. The changes in the intensity of the shade in the plot represent the change in the MRR. Figures 4(a) – 4(c) represent the influence of parameters such as EC, V and IEG on MRR. Figure 4(a) exhibits the influence of the applied voltage and IEG on MRR. The increase in the voltage increases the machining current in the inter electrode gap (IEG), thereby increasing the MRR.

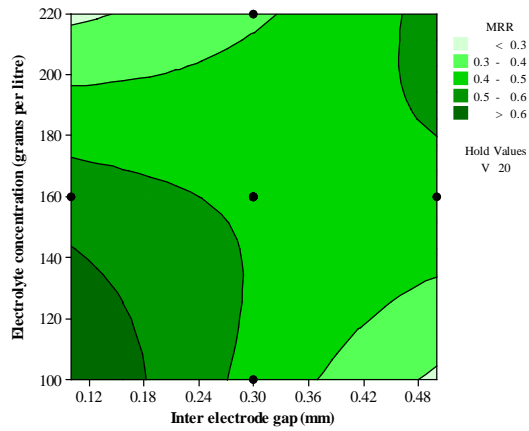
Smaller IEG increases the rapid anodic dissolution as a result of higher current density [15]. This conforms to the fundamental machining mechanism of ECM. Figure 4(b) represents the effect of IEG and EC on the MRR. The mobility of ions in the high concentration of electrolyte in the small IEG is disturbed. Therefore, it results in poor MRR. But, the smaller IEG and the moderate concentration allow more ions for ionisation, which results in increasing the MRR. This can be seen from the Figure 4(b).

Figures 5-7 highlights the effect of voltage with EC 160 grams per liter and IEG 0.3 mm on surface roughness (R_a) and MRR. Figure 5 clearly exhibits the very good anodic dissolution at high voltage (30 V). Higher voltages break the surface film and its disruption is non-uniform that results deep grain boundary attack of the metal surface. At low voltage (10 V), dissolution is poor, which could be seen in Figure 6.

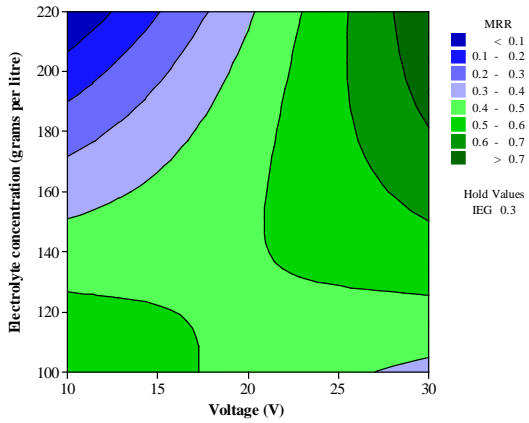
High and uniform dissolution occurs at 20 V as observed in Figure 7. This voltage is sufficient to make a uniform dissolution. It can be observed that the increase in electrolyte concentration (EC) increases MRR. The increase in both voltage (V) and EC enhances the MRR considerably which is attributed to the effect of the increase in the conductance of electrolyte. This can be seen in Figure 4(c).



(a) Influence of V and IEG on MRR



(b) Influence of EC and IEG on MRR



(c) Influence of EC and V on MRR

Figure 4. Contour Plots of MRR

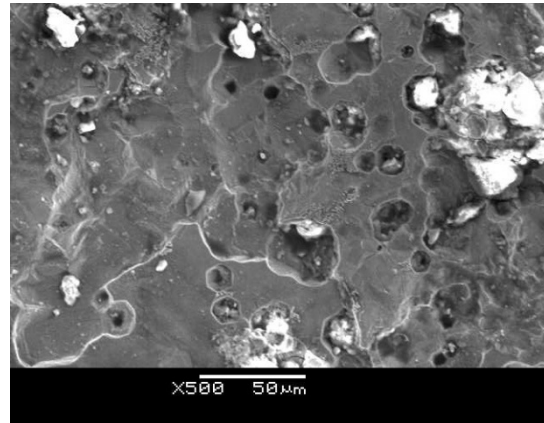


Figure 5. High and non uniform dissolution at 30 V

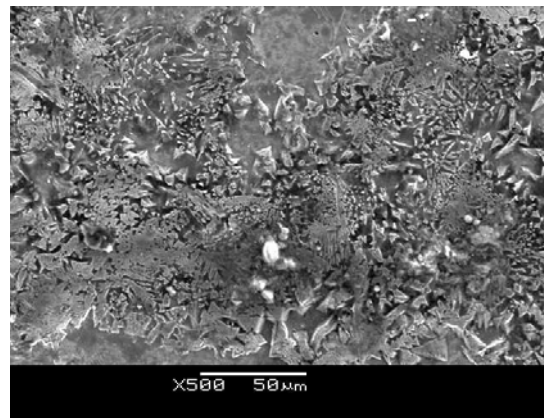


Figure 6. Moderate dissolution at 10 V

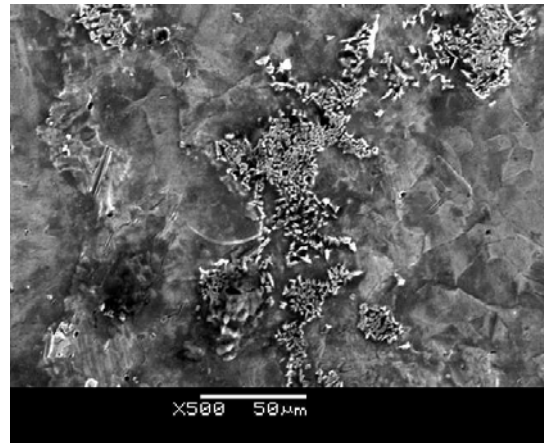
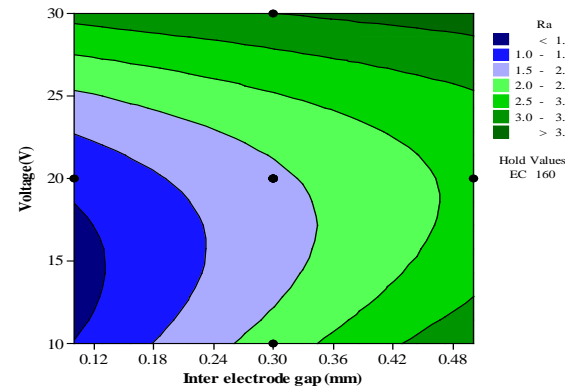


Figure 7. High and uniform dissolution at 20 V

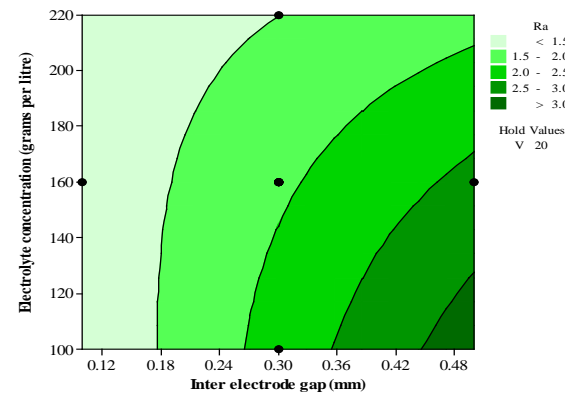
4.2. Parametric Influence on Ra

Figures 9(a) -9(c) illustrate the influence of parameters on the surface roughness (Ra) in aqueous NaCl environment. Figure 9(a) demonstrates the effect of the applied voltage (V) and IEG on the surface roughness (Ra) of machined Monel 400 alloys. Higher voltage enhances the anodic dissolution drastically but with some excessive heating, which leads to a poor surface finish. Low voltage is sufficient to get a good surface finish. But higher IEG reduces the current density in the gap which leads to non-uniform metal removal and results in a poor surface finish as shown in Figure 8.

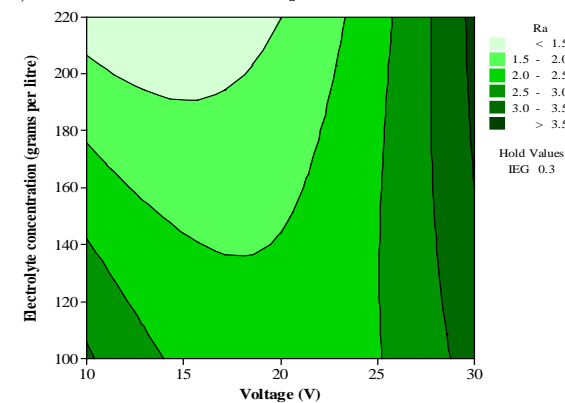
Higher electrolyte concentration and voltage lead to a rapid metal dissolution which results in a higher Ra. A slightly high electrolyte concentration with a low IEG produces low Ra. This is due to the higher current density in the smaller IEG with a uniform metal dissolution because of an adequate concentration.



a) Influence of V and IEG on Ra



b) Influence of EC and IEG on Ra



c) Influence of EC and V on Ra

Figure 9. Contour plots of surface roughness(Ra)

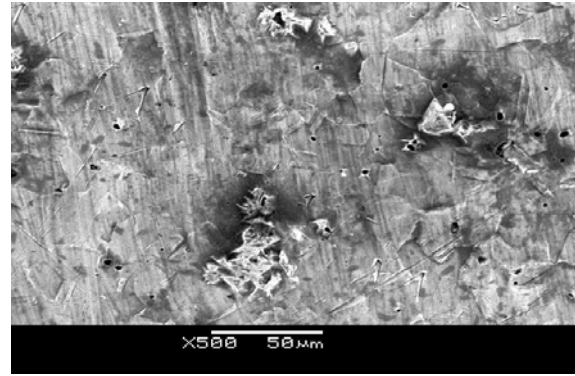


Figure 8. Poor dissolution at high IEG 0.5 mm

5. Response Surface Optimization

In RSM, multiple responses are optimized with the steepest ascent/descent method by the desirability function (DF). DF is one of the most extensively used methods for multi-response optimization. It transforms each response y_i into an individual desirability function $d_i(y_i)$ that varies in the range (0, 1). It increases as the corresponding response value becomes more desirable. Depending upon the nature of the responses (y_i), the desirability functions $d_i(y_i)$ will be maximized/minimized, or assigned to a target value. The individual desirability $d_i(y_i)$ will be as follows:

$$d_i(y_i) = 0 \text{ if } y_i(x) \leq L_i \tag{6}$$

$$d_i(y_i) = \left(\frac{y_i(x) - L_i}{T_i - L_i}\right)^r \text{ if } L_i \leq y_i(x) \leq T_i \tag{7}$$

$$d_i(y_i) = \left(\frac{y_i(x) - U_i}{T_i - U_i}\right)^r \text{ if } T_i \leq y_i(x) \leq U_i \tag{8}$$

$$d_i(y_i) = 0 \text{ if } y_i(x) > U_i \tag{9}$$

Where, x is the parameters, i.e., IEG, V, EC
 L_i and U_i are lower and upper acceptable bounds of y_i ,
 T_i is target values desired for i^{th} response, where $L_i < T_i < U_i$

r is the parameter that determines the shape of $d_i(y_i)$.

The individual desirability functions are then combined using the geometric mean, which gives the Composite desirability D :

$$D = ((d_1(y_1) * d_2(y_2) * \dots * d_m(y_m))^{\frac{1}{m}} \tag{10}$$

Table 5. Constraints

Variables	Goal	Lower bound (L_i)	Upper bound (U_i)
x_i	IEG	In the range	0.2 0.4
	V	In the range	15 25
	EC	In the range	130 190
y_u	MRR	Maximize	0.294 0.6298
	Ra	Minimize	1.23 3.5

The best composite desirability (0.822) is established at the following machining conditions.

IEG=0.2mm,V=18 V, EC=130 grams per litre, MRR=0.5546 grams per minute, Ra=1.5216 μ m

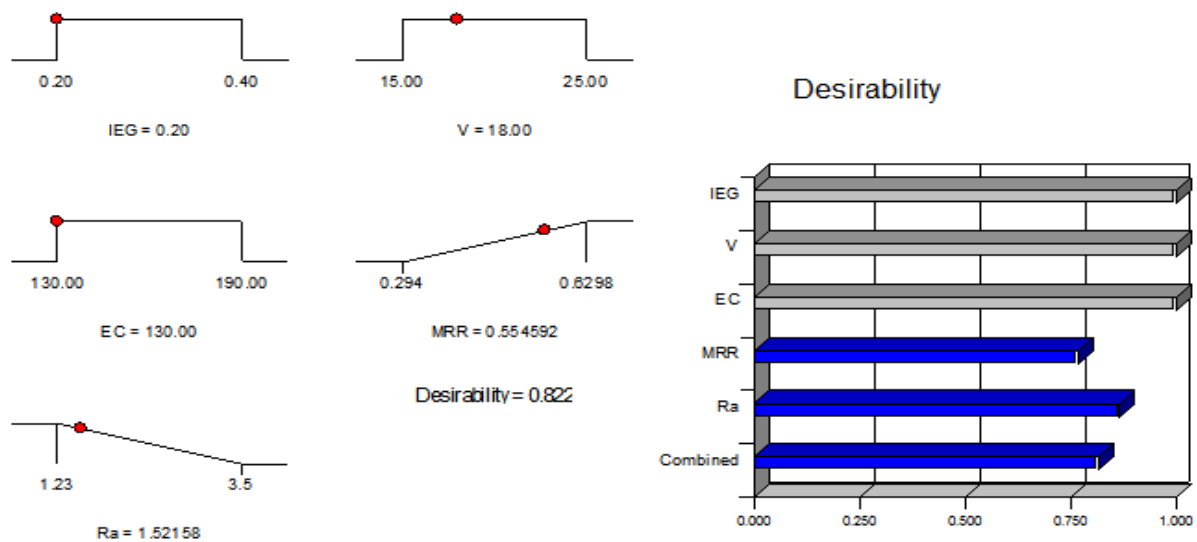


Figure 10. Ramps and bar chart

Figure 10 represents the ramps and bar chart at the optimal machining conditions.

6. Conclusion

An attempt has been made in this work to highlight the influence of ECM process parameters on the machining performances, i.e., MRR, R_a for Monel 400 alloys. Response surface methodology was employed to analyze the ECM process. Mathematical models have also been developed based on the RSM approach for correlating the MRR and R_a with process parameters. The adequacy of the developed mathematical model has been tested through the analysis of variance (ANOVA). The results of the analysis justify the closeness of the fit of the mathematical model at 95% confidence level. The influence of different process parameters on machining performance criteria are exhibited through contour plots. It is clear from the response contour plot of MRR that both the MRR and surface roughness increase with the increase in the voltage. The increase in the voltage causes the excessive heating of electrolyte and a corresponding deterioration of the work piece surface which increases the surface roughness. Electrolyte concentration of 160 grams per liter and IEG 0.3 mm provide good MRR and R_a . From the developed mathematical model, the optimal machining parametric combination, i.e., IEG=0.2 mm, V=18 V and EC=130 grams per liter was found out to achieve the maximum material removal rate, i.e., 0.5546 grams per minute and minimum surface roughness as 1.5216 μm . The effective utilization of ECM for Monel 400 alloys for achieving the best material removal rate (MRR) and surface roughness (R_a) has been attempted in this work.

References

- [1] Rajurkar K.P, Sundaram M.M and Malshe A. P, "Review of Electrochemical and Electro discharge Machining", *Procedia CIRP*, Vol. 6 (2013) 13-26, The Seventeenth CIRP Conference on Electro Physical and Chemical Machining (ISEM).
- [2] Rajurkar K.P, Zhu D, McGeough J.A, Kozak J and De Silva A, "New Developments in Electro-Chemical Machining", *CIRP Annals - Manufacturing Technology*, Vol. 48 (1999) Issue 2, 567-579.
- [3] Sundaram M.M. and Rajurkar K.P, "Electrical and Electrochemical Processes, in *Intelligent Energy Field Manufacturing*", CRC Press (2010) 173-212.
- [4] Ezugwu E.O, "Key improvements in the machining of difficult-to-cut aerospace super alloys", *International Journal of Machine Tools and Manufacture*, Vol. 45(2005) Issues 12-13, 1353-1367
- [5] Ezugwu E.O, Bonney J, Fadare D.A and Sales W.F, "Machining of nickel-base, Inconel 718, alloy with ceramic tools under finishing conditions with various coolant supply pressures", *Journal of Materials Processing Technology*, Vol. 162-163(2005) issue 15, 609-614.
- [6] Liu H.S, Yan B.H, Huang F.Y and Qiu K.H, "A study on the characterization of high nickel alloy micro-holes using micro-EDM and their applications", *Journal of Materials Processing Technology*, Vol. 169(2005) Issue 3, 418-426.
- [7] Durul Ulutan and Tugrul Ozel, "Machining induced surface integrity in titanium and nickel alloys: A review", *International Journal of Machine Tools and Manufacture*, Vol. 51(2011) Issue 3, 250-280.
- [8] Selvakumar G, Sarkar K and Mitra S, "Experimental analysis on WEDM of Monel 400 alloys in a range of thickness", *International Journal of Modern Manufacturing Technologies*, Vol. IV (2012) 113-120.
- [9] Selvakumar G, Sarkar K and Mitra S, "Experimental investigation on die corner accuracy for wire electrical discharge machining of Monel 400 alloy", *Proc IMechE Part B: J Engineering Manufacture*, Vol. 226 (2012) 10, 1694-1704.
- [10] Theisen W and Schuermann A, "Electro discharge machining of nickel-titanium shape memory alloys", *Materials Science and Engineering: A*, Vol. 378 (2004) Issues 1-2, 200-204.
- [11] Kaynak Y, Karaca H.E, Noebe R.D and Jawahir I.S, "Tool-wear analysis in cryogenic machining of *NiTi* shape memory alloys: A comparison of tool-wear performance with dry and MQL machining", *Wear*, Vol. 306 (2013) Issues 1-2, 51-63.
- [12] Curtis D.T, Soo S.L, Aspinwall D.K and Sage C, "Electrochemical super abrasive machining of a nickel-based aero engine alloy using mounted grinding points", *CIRP Annals - Manufacturing Technology*, Vol. 58 (2009) Issue 1, 173-176.
- [13] Gao D, Hao Z, Han R, Chang Y and Muguthu J.N, "Study of cutting deformation in machining nickel-based alloy Inconel 718", *International Journal of Machine Tools and Manufacture*, Vol. 51(2011) Issue 6, 520-527.

- [14] Montgomery Douglas C, "Design and Analysis of Experiments" 5th edition (1997), John Wiley publications, Singapore.
- [15] Kadirgama K, Noor M.M, Zuki N.M, Rahman M.M, Rejab M.R.M, Daud R and Abou-El-Hossein K. A, "Optimization of Surface Roughness in End Milling on Mould Aluminium Alloys (AA6061-T6) Using Response Surface Method and Radian Basis Function Network", Jordan Journal of Mechanical and Industrial Engineering, Vol. 2 (2008) No.4, 209-214.
- [16] Senthilkumar C, Ganesan G and Karthikeyan R, "Study of electrochemical machining characteristics of Al/SiC_p Composites", International Journal of Advanced Manufacturing Technology 43 (2009) 256-263.
- [17] Rama Rao S and Padmanabhan G, "Effect of process variables on metal removal rate in electrochemical machining of Al-B₄C composites", Archives of Applied Science Research, Vol. 4 (2012) 4, 1844-1849.
- [18] Rama Rao S and Padmanabhan G, "Linear Modelling of the Electrochemical Machining Process Using Full Factorial Design of Experiments", Journal of Advanced Mechanical Engineering, Vol. 1 (2013) 13-23.
- [19] Senthil Kumar K.L, Sivasubramanian R and Kalaiselvan K, "Selection of Optimum Parameters in Non-Conventional Machining of Metal Matrix Composite", Portugaliae Electrochimica Acta, Vol. 27 (2009) 4, 477-486.

Statistical Investigation on Effect of Electroless Coating Parameters on Coating Morphology of Short Basalt Fiber

S. Ezhil Vannan^{*1}, S. Paul Vizhian²

¹Research scholar, ²Professor & Chairman Department of Mechanical Engineering, University Visvesvaraya College of Engineering, K.R. Circle, Bangalore University, Bangalore-560001, India

Received 28 Feb 2014

Accepted 11 Jun 2014

Abstract

The Objective of the present paper is to investigate the effect of electroless coating parameters, such as Sensitization time (A), Activation time (B) and Metallization time (C), on the coating morphology of the basalt short fiber and the optimization of the coating process parameters based on L_{27} Taguchi orthogonal design. Coated and non-coated basalt short fiber, typically used with 7075 Aluminium alloy as reinforcement, is studied. The effect of coating the short basalt fiber with copper has proved beneficial to interfacial bonding (wettability) between the reinforcement and the matrix. The interface between the matrix and the reinforcement plays a crucial role in determining the properties of metal matrix composites (MMCs). An L_{27} array was used to accommodate the three levels of factors as well as their interaction effects. From the Taguchi methodology, the optimal combinations for coating parameters were found to be $A_1B_3C_3$ (i.e., 5 min. sensitization time, 15 min. activation time and 3 min. for metallization time). In addition, the interaction between pH value and the coating time and that between the coating time and the temperature, influence the coating parameters significantly. Furthermore, a statistical analysis of variance reveals that the metallization time has the highest influence followed by the activation time and the sensitization time. Finally, confirmation tests were carried out to verify the experimental results, Scanning Electron Microscopic (SEM) & Energy Dispersive Spectroscopy (EDS) studies were carried out on basalt fiber.

© 2014 Jordan Journal of Mechanical and Industrial Engineering. All rights reserved

Keywords: Electroless Coating, Basalt Fiber, Taguchi Technique, Genetic Programming.

1. Introduction

The interface between the matrix and the reinforcement is crucial and can affect the fabrication process significantly. If this interface is not tailored properly, it can lead to the degradation of the properties of composites. One of the general approach to this problem is deposition of coating around the fiber [1]. The coating technique has been studied by many researchers for the fabrication of metal matrix composites (MMC) [1-4]. Coating of reinforcement is one of the successful techniques adopted to prevent interfacial reaction and enhance the wetting of reinforcement [5]. Electroless copper coating of the reinforcement, which is a simple, low-cost and an easy to use process, has been successfully applied to prevent undesirable interfacial reactions and promote the wettability through increased overall surface energy of the reinforcement [6-8]. An attempt is made in the present investigation to assess the influence of electroless coating parameters such as Sensitization time (A), Activation time (B) and Metallization time (C) on the coating morphology of basalt short fiber. There are several other coating parameters that can affect the coating process of basalt

short fiber viz. pH value and temperature of the bath. In this study, Sensitization time (A), Activation time (B) and Metallization time (C) are considered for the optimization of coating. The main purpose of this work is to establish the influence of these coating parameters on the coating morphology of basalt short fiber and further to optimize the process based on L_{27} Taguchi orthogonal design [9-10]. This can be achieved through a series of experiments. However, such experiments will be expensive and often time-consuming. Design of Experiment (DOE) techniques, like the Taguchi method, can minimize the experimental runs to optimize the coating parameters. Furthermore, to identify which of the testing parameters have a significant influence over the performance of copper coating, Analysis of Variance (ANOVA) is also performed. Finally, verification and validation of the optimal condition obtained through orthogonal array design is carried out through a confirmation test and the improvement in the coating performance characteristics at the optimal condition is compared to the initial condition. Results thus obtained are also correlated with the ones obtained by genetic programming using DISCIPULUSTM software.

* Corresponding author. e-mail: ezhilsil@yahoo.co.in.

2. Design of Experiments (DOE)

Design of experiment is one of the important and powerful statistical techniques to study the effect of multiple variables simultaneously and it involves a series of steps which must follow a certain sequence for the experiments to yield an improved understanding of process performance. These experiments result in a certain number of combinations of factors and levels to be tested in order to achieve the required parametric variations. Taguchi approach relies on the assignment of factors in specific orthogonal arrays to determine those test combinations. Analysis of the experimental results uses a signal to noise ratio to aid in the determination of the best process design. The application of DOE concepts, like Taguchi technique factorial and surface response, has gained importance since these were helpful in providing information about the influence of various parameters in the hierarchical rank order. The combined effects of these parameters can be analyzed, and the correlation term can be found using these techniques.

2.1. Taguchi Technique

The Taguchi method, which is effective to deal with responses, was influenced by multi-variables. This method drastically reduces the number of experiments that are required to model the response function compared with the full factorial design of experiments. The major advantage of this technique is to find out the possible interaction between the parameters. The Taguchi technique is devised for the process optimization and the identification of the optimal combination of the factors for a given response. This technique is divided into three main phases, which encompass all the experimentation approaches. The three phases are:

1. The planning phase
2. The conduction phase
3. The analysis phase.

The planning phase is the most important phase of the experiment. This technique creates a standard orthogonal array to accommodate the effect of several factors on the target value and define the plan of experiments. The experimental results are analyzed using the analysis of means and variance to study the influence of the factors.

3. Experimental Work

3.1. Materials and Methods

Basalt is a natural material that is found in volcanic rocks. It has a melting temperature of 1300-1700°C, which is crushed and spun into fine continuous fibers. These are made with thermosetting resins, such as epoxy and (phenolic) polyesters using techniques like prepregs, laying out, winding, direct pressure autoclaving, and vacuum moulding etc. Continuous basalt fibres (CBF) has good thermal, electrical and sound insulating properties, good resistance to acids and solvents, and good thermal stability (under very low stress up to 1250°C, under common load only to 500°C) and has low cost compared to other fibers. Reinforcements used in this study are in the form of continuous basalt fibers with chemical

composition as shown in Table 1. In the present investigation, the deposition of copper coating on basalt short fibers by an electroless route has been optimized.

Table 1. Chemical composition of short basalt fiber

Element	SiO ₂	Al ₂ O ₃	Fe ₂ O ₃	MgO	CaO	Na ₂ O	K ₂ O	TiO ₂	MnO
%	69.51	14.18	3.92	2.41	5.62	2.74	1.01	0.55	0.04

3.2. Pre-Procedure

The continuous basalt fibers of average diameter 6 μm were chopped down to short fibers of about 1 to 2 mm length. The complete process of coating starts with the treatment of fibers in a muffle furnace for 10 min. at 500°C to eliminate the pyrolytic coatings around as received fibers. The electroless process, used to deposit the copper coatings on the basalt fiber, relies on a sequence of sensitizing, activation and metallization, with important cleaning, rinsing, washing and drying stages also being included.

3.3. Experimental Procedure

The short basalt fiber was cleaned in distilled water and dried at 90°C. The sizing and finishing treatment from the surface of the fibers, prior to coating, were removed by heating them to about 970 K for 10 min. in air. Fibers have elastic modulus of 90 GPa, and a yield stress of 4500 MPa. The coating procedure consist of three well-defined stages, namely sensitization, activation and metallization. The heat-cleaned fibers are first treated with glacial acetic acid to activate the surface, and then activated again using stannous chloride (SnCl₂); they were sensitized for different times (5, 10 & 15 min.) under continuous stirring. Fibers are then filtered and cleaned with distilled water. In order to have catalytic surfaces, the sensitized fibers were exposed to an aqueous solution containing palladium chloride (PdCl₂) and HCl under ultrasonic agitation. This process, called activation, produces the formation of Pd sites on the fiber surface, which allows the subsequent metallization with copper. The complete process of metallization starts with the treatment of fibers in an open oven for 10 min. at 500°C to eliminate the pyrolytic coatings around as received fibers.

Metallization is produced by immersion of activated fibers into a solution containing CuSO₄.5H₂O as metal ion sources also held under agitation. Different metallization conditions have been tried with timings, as indicated in Table 2, for the three processes, and the required thickness has been achieved. The reactive volume used assures that the concentration of the diluted copper can be considered constant during the deposition. The coatings obtained at different metallization times were then studied by SEM and the thickness of the copper layer was determined in transversal cross section. The specimen was mounted on a metal stub on top of which a double sided carbon tape was used and the sample was stuck on a carbon tape. Later the entire stub was placed in the coating machine for the copper coating process. For a non-conductive specimen, metal coating was usually applied to give the specimen electrical conductivity. This decreases the specimen's capacity to acquire an electrostatic charge and increases

the yield of secondary electrons. The important thing to remember while applying coating on short basalt fiber is to make sure that the coating on basalt short fiber must be as thin as possible so that the specimen surface morphology is not completely covered by coating. The resultant images reveal remarkable structural resolution down to a few nanometers with great accuracy, because the film provides a continuous coating over all the sample contours. The mould or stub was kept in the vacuum chamber and SEM imaging and EDS were done through JEOL JSM 6360 - A model with a magnification capacity of X500, X1000, X2000 and accelerating voltage of 20 kV with a working distance of 10 mm. The first area of image was chosen and focused then through software EDS analysis was done on the same image by either selecting spot analysis or line analysis or area analysis. The morphology of the coated fiber is studied with SEM followed by EDS to evaluate elemental distribution. Experiments were conducted based the outcome of Taguchi's technique. A L_{27} orthogonal array was selected for the analysis of the data as given in Table 3. Investigation to find the effect of time for sensitization, time for activation & time for metallization was carried out using Taguchi S/N ratio and regression equations for each response were developed. Objective of the model was chosen as 'Nominal the best type' [12] characteristics to analyze the effect of coating parameter.

3.4. Plan of Experiment

Conventional experimental design methods are too complex and expensive. A large number of experiments have to be carried out to study the process. Taguchi method uses an orthogonal array to study the entire process with only a small number of experiments. Moreover, traditional experimentation involves one factor at a time, wherein one variable is changed while the rest are held constant. The major disadvantage of this method is that it fails to consider any possible interactions between the parameters. An interaction is the failure of one factor not to produce the same effect on the response at different levels of a second factor varying. It is also not possible to study all the factors involved in the process and to determine their main effects (i.e., the individual effects) in a single experiment. Taguchi technique overcomes all these drawbacks and hence used for optimizing coating parameters and identifying the optimal combination of factors for the desired responses [15]

The steps involved are:

1. Identification of the response functions and the process parameters.
2. Determination of the number of levels for the process parameters and possible interaction between them.
3. Selection of the appropriate orthogonal array.
4. Selection of the optimum level of process parameters through Analysis of Variance [ANOVA].
5. Performing a confirmation experiment to verify the optimal process parameters.

The experiments were conducted as per the standard orthogonal array. The selection of the orthogonal array was based on the condition that the degrees of freedom for the orthogonal array should be greater than or equal to the sum of those coating parameters. In the present investigation, an L_{27} orthogonal array was chosen, which has 27 rows and 13 columns, as shown in the Table 3.

Table 2. Coating parameters with their values at three levels

Duration (minutes)			
Level	Sensitization	Activation	Metallization
1	5	5	1
2	10	10	2
3	15	15	3

The input parameters chosen for the experiments are Sensitization time (A) in minutes, Activation time (B) in minutes and Metallization time (C) in minutes. Table 2 indicates the factors and their levels. Trial runs were carried out by varying one of the coating parameters while keeping the rest of them at constant values. The working range was decided upon by measuring the achievable amount of deposition of copper coating on basalt short fiber. The range and the number of levels of the design parameters are given in Table 2. The fiber coating experiment was performed as per the condition dictated by design matrix, developed through Taguchi technique. The experiments consist of 27 tests (each row in the L_{27} orthogonal array) and the columns were assigned with parameters. The first column in Table 3 was assigned to time for sensitization (A), the second column for activation (B) and the fifth for metallization (C) and the remaining columns were assigned to their interactions. The response to be studied was the coating thickness on the fiber with the objective as "Nominal the best". The experiments were conducted as per the orthogonal array with level of parameters given in each array row. The coating test results were subjected to the analysis of variance.

Table 3. Orthogonal Array L₂₇ (3¹³) of Taguchi

L ₂₇ (3 ¹³) Test	1	2	3	4	5	6	7	8	9	10	11	12	13
1	1	1	1	1	1	1	1	1	1	1	1	1	1
2	1	1	1	1	2	2	2	2	2	2	2	2	2
3	1	1	1	1	3	3	3	3	3	3	3	3	3
4	1	2	2	2	1	1	1	2	2	2	3	3	3
5	1	2	2	2	2	2	2	3	3	3	1	1	1
6	1	2	2	2	3	3	3	1	1	1	2	2	2
7	1	3	3	3	1	1	1	3	3	3	2	2	2
8	1	3	3	3	2	2	2	1	1	1	3	3	3
9	1	3	3	3	3	3	3	2	2	2	1	1	1
10	2	1	2	3	1	2	3	1	2	3	1	2	3
11	2	1	2	3	2	3	1	2	3	1	2	3	1
12	2	1	2	3	3	1	2	3	1	2	3	1	2
13	2	2	3	1	1	2	3	2	3	1	3	1	2
14	2	2	3	1	2	3	1	3	1	2	1	2	3
15	2	2	3	1	3	1	2	1	2	3	2	3	1
16	2	3	1	2	1	2	3	3	2	1	2	3	1
17	2	3	1	2	2	3	1	1	2	3	3	1	2
18	2	3	1	2	3	1	2	2	3	1	1	2	3
19	3	1	3	2	1	3	2	1	3	2	1	3	2
20	3	1	3	2	2	1	3	2	1	3	2	1	3
21	3	1	3	2	3	2	1	3	2	1	3	2	1
22	3	2	1	3	1	3	2	2	1	3	3	2	1
23	3	2	1	3	2	1	3	3	2	1	1	3	2
24	3	2	1	3	3	2	1	1	3	2	2	1	3
25	3	3	2	1	1	3	2	3	2	1	2	1	3
26	3	3	2	1	2	1	3	1	3	2	3	2	1
27	3	3	2	1	3	2	1	2	1	3	1	3	2

4. Results and Discussion

4.1. Analysis of Experimental Results

After being collected, the data are to be analyzed by means of calculating S/N ratio (S/N: Signal/Noise) [16]. The signal to noise ratio in this case is a quality indicator by which the effect of changing a particular coating parameter for deposition of copper on the short basalt fiber is evaluated. In general, a better signal is obtained when the noise is smaller, so that a larger S/N ratio yields better final results. This means that the divergence of the final results becomes smaller. Signal to noise ratios of each experimental run is calculated based on the following equation, and the values are

$$S/N (\eta) = 10 \log_{10} (\mu^2/\sigma^2); \text{ Where } \mu=1/n\Sigma y_i,$$

$$\sigma^2= 1/(n-1) \Sigma (y_i - \mu)^2$$

Where y_1, y_2, \dots, y_n are the response of the coating thickness and 'n' is the number of observation.

The experimental results are analyzed, to see the main effects of interaction between level 1, level 2 and level 3 of the variables on coating parameters in the experiments. In the present work, three runs are performed for each of the nine experiments. The main objective of the present work is to optimize Sensitization time, Activation time and Metallization time to achieve the desired coating thickness; the above mentioned approach has been adopted. However, in situations where there is a feasibility to perform multiple runs for each combination of parameters provided by the design matrix, the Taguchi analysis can be performed by using S/N ratio analysis. In the present analysis, considering the constraint (coating thickness and time) mentioned above, Taguchi analysis is performed based on "average of results" methodology, which is shown in Table 4. Based on the analysis in Table 4, using S/N ratio, the optimum combination would be [A₁B₃C₃]

4.2. Analysis of Variance

The use of ANOVA is to analyze the influence of coating parameters like (A) time for sensitization, (B) time of activation, and (C) time for metallization. This analysis was carried out for a level of significance of 5% that is the level of confidence 95%. Table 5 shows the results of ANOVA analysis. One can observe from the ANOVA analysis that the time for sensitization, time for activation and time for metallization have the influence on coating thickness on fiber. The last column in Table 5 shows the percentage contribution of each factor on the total variation indicating their degree of influence on the result. The interaction between the above factors does not have a significant variation on the coating thickness on the fiber.

It can be observed from the ANOVA table that the time for metallization ($p=0.97\%$) is comparatively less than the time for activation ($p=25.94\%$) and time for sensitization ($p=3.25\%$), in spite of which there is no appreciable decrease in coating thickness. However, the interaction between time for sensitization and time of activation ($p=18\%$), time of activation and time for metallization ($p=45.03\%$) shows the highest when compared to time of activation and time for metallization ($p=4.44\%$). The pooled error associated in ANOVA table was approximately about 2.37%. This approach gives the variation of means and variance to absolute values considered in the experiment and not the unit value of the variable.

Table 4. S/N ratios for coating thickness for different coating parameters

Exp. No.	Time for sensitization (min)	Time for activation (min)	Time for metallization (min)	Mean thickness coating (μm)	S/N ratio (dB)
1	5	5	1	0.0465	-6.256
2	5	5	2	0.0981	0.218
3	5	5	3	0.0984	0.245
4	5	10	1	0.0840	-1.135
5	5	10	2	0.0536	-5.032
6	5	10	3	0.0394	-7.705
7	5	15	1	0.0376	-12.011
8	5	15	2	0.0552	-4.776
9	5	15	3	0.0157	-18.111
10	10	5	1	0.0685	-2.901
11	10	5	2	0.0240	-15.697
12	10	5	3	0.0993	0.324
13	10	10	1	0.0722	-2.444
14	10	10	2	0.0799	-1.564
15	10	10	3	0.0617	-3.809
16	10	15	1	0.0457	-6.417
17	10	15	2	0.1068	0.957
18	10	15	3	0.0430	-6.956
19	15	5	1	0.1048	0.792
20	15	5	2	0.0541	-4.951
21	15	5	3	0.1112	1.307
22	15	10	1	0.1044	0.755
23	15	10	2	0.0908	-0.458
24	15	10	3	0.0610	-3.908
25	15	15	1	0.0350	-8.734
26	15	15	2	0.0575	-4.422
27	15	15	3	0.0200	-13.594

Table 5. ANOVA Results

Source of Variances	SS	DOF	Variance	F _{cal}	F _{th}	p %
A	0.000583	2	0.000292	05.49	3.39	03.25
B	0.004649	2	0.002324	43.75	3.39	25.94
C	0.000174	2	0.000086	01.63	3.39	00.97
A x B	0.003226	4	0.001613	15.17	3.39	18.00
A x C	0.008071	4	0.004035	37.98	3.39	45.03
B x C	0.000795	4	0.000398	03.74	3.39	04.44
Error	0.000425	8	0.000213		3.39	02.37
Total	0.017923	26	0.008961			100.00

4.3. Morphology of Electroless Cu Coating

Figure 1 (a) shows the SEM micrographs as received basalt fiber and Figure 1(b) and 1(c) show electroless copper coated basalt fibers with low and higher magnification [17]. As shown in Figure 1 (a), basalt fibers have smooth surface striations along the fiber axis. In spite of the different surface morphology, the electroless copper films have been deposited on the fiber surface with good adhesion as indicated in Figures 1(b) and 1(c). From Figure 1 (c), we observe the deposition of copper layer on the surface of basalt fiber with a thickness of 40 nanometres as measured by SEM. A uniform and continuous coating of copper was given to short basalt fiber by optimized value about 95% of the continuously coated fibers had a coating thickness range about 20-50 nanometres and above this showed isolated dendrite deposit of copper. Figure 2, (a) and (b), shows the EDS pattern of uncoated and copper coated basalt fiber, respectively. Micrographs reveal clearly the deposition of copper on the short basalt fiber. Superior aggregations among the basalt fiber were observed due to the high chemical activity of copper atoms. The original basalt fiber exhibit a glossy surface. It can also be seen via the micrographs that, after successful coating, the surface appears dim. The EDS results confirm the presence of Cu, indicating a successful activation, sensitization and metallisation process.

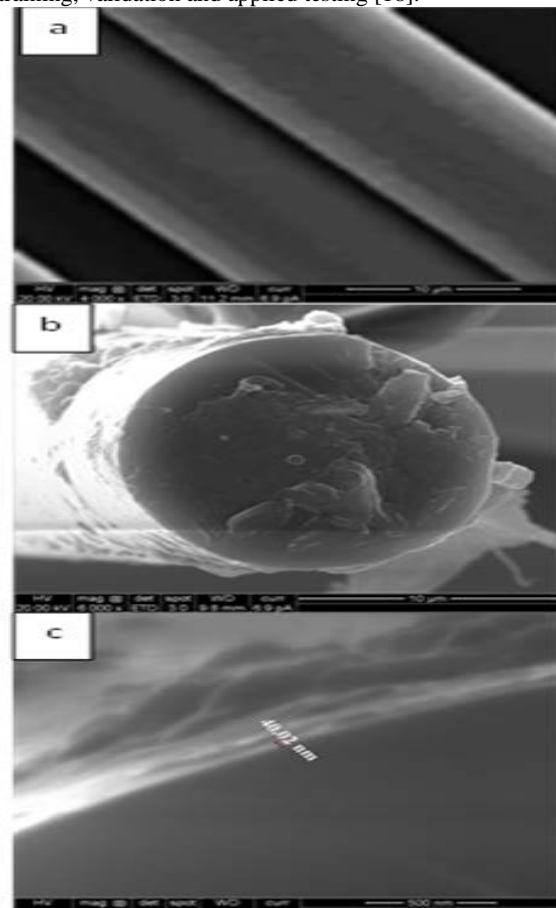
4.4. Orthogonal Array of Taguchi for Coating Thickness

The experimental studies were conducted according to the L₂₇ orthogonal mixed level array. The coating thickness was obtained as a result of the electroless coating experiments and the corresponding S/N ratios values are tabulated in the Table 4.

A graph of main factors plotted against the factor level obtained by calculating the coating thickness of the specimens are as shown in fig 3(a) & 3(b). It is observed from the graph that the coated thickness tends to increase in factor A (time for sensitization), a decrease in factors B (time for activation) and C (time of metallization). The levels that have the highest value of the S/N ratio and mean of mean thickness are the best factor levels. The optimum value is observed for combination of A₁B₃C₃ equation obtained by the S/N ratios.

4.5. Confirmation Test

A parallel study using GP was taken up to correlate the Taguchi based approach using DISCIPULUS™ software. To implement the concept of Genetic Programming, DISCIPULUS™ software was used. Data sets from the experiments were taken for analysis. The data samples were randomized manually using Microsoft Excel software. The randomized data sets were fed into the software by initially splitting them into three sets viz., training, validation and applied testing [18].

**Figure 1.** SEM micrographs

- a) Uncoated basalt fiber
- b) Lower magnification copper coated basalt fiber
- c) Higher magnification copper coated basalt fiber [17]

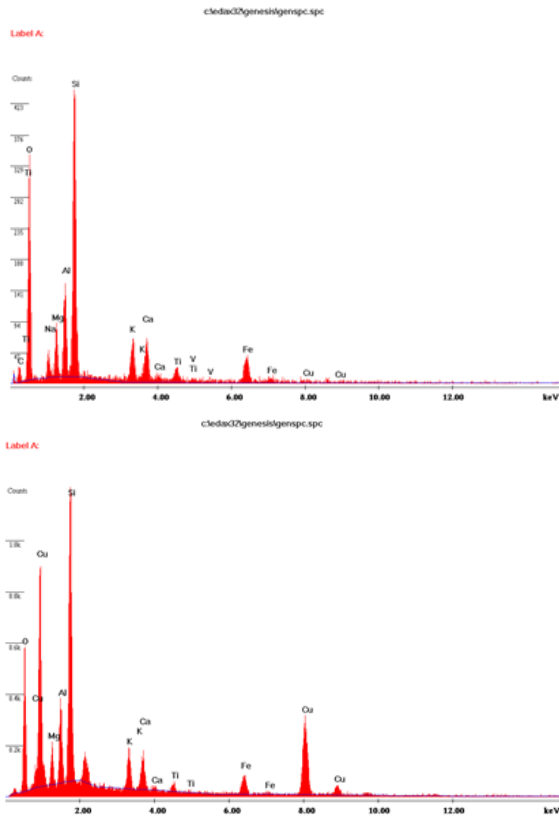


Figure 2. EDS image pattern

- a) Uncoated basalt fiber
- b) Copper coated basalt fiber [17]

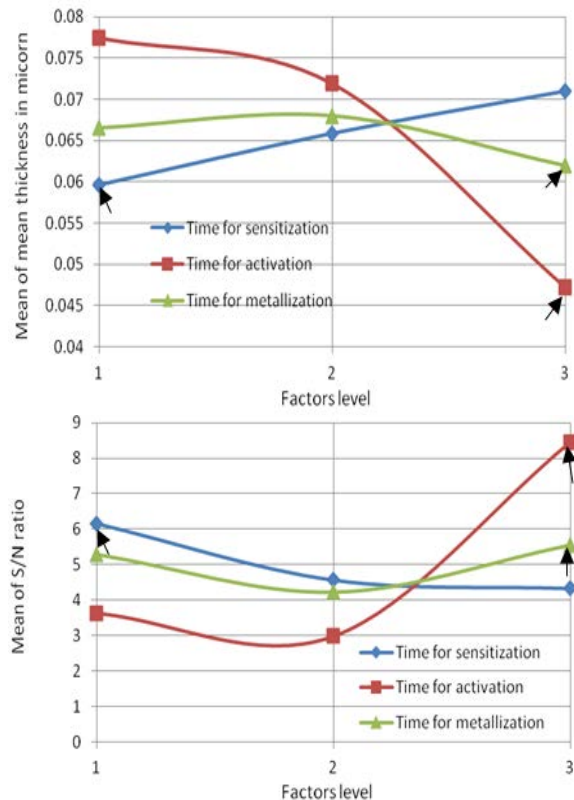


Figure 3. Relative effect of main factors on coating

- a) Mean of mean thickness
- b) S/N ratio.

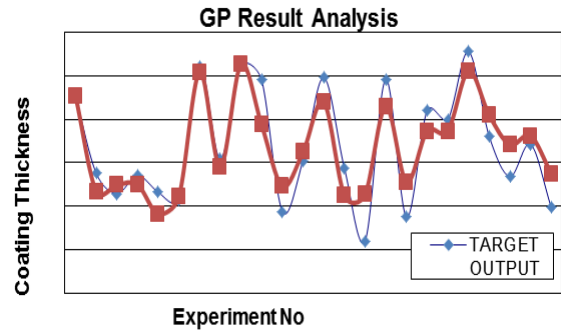


Figure 4. GP Result Analysis

5. Conclusions

From the analysis on the results of coating parameter on coating morphology of short basalt fiber by electroless method, the following conclusions can be drawn:

1. Coating of copper on short basalt fiber has been carried out successfully by electroless method.
2. Coating with optimized values resulted in about 95% of the continuously coated fibers with a coating thickness range of 20-50 nanometres and isolated dendrite deposit of copper in the remaining region.
3. Taguchi orthogonal array design is suitably applied to optimize the three coating parameters such as time for sensitization(A), time for activation(B) and time for metallization(C) to achieve the required coating thickness of Cu.
4. The optimum testing condition $[A_1B_3C_3]$ obtained from the analysis yields optimum coating thickness compared to other parametric combinations.
5. ANOVA shows that the time for metallization ($p=0.97\%$) is comparatively less than the time for activation ($p=25.94\%$) and time for sensitization ($p=3.25\%$), in spite of which there no appreciable decrease in coating thickness.
6. The SEM micrographs and EDS results indicate that the optimized parameters resulted in consistent coating morphology and thickness.
7. The results obtained from genetic programming were compared with the experimental values obtained by Taguchi technique. The results obtained from genetic programming are in general agreement with the experimental results with minimal variations.

References

- [1] T. P. D. Rajan, R. M. Pillai, B. C. Pai, J. Review "Reinforcement coatings and interfaces in aluminium metal matrix composites", Mater. Sci.33 (1998) 3491-3501
- [2] Delannay F, Froyen. L, Deruyttere A. Review: The wetting of solids by molten metals and its relation to the preparation of metal-matrix composites. J. Mater. Sci. 22 (1987) 1–16.
- [3] Baker, A.A., Shipman, C., Jackson, P.W. Short-term compatibility of carbon fibres with aluminium. Fibre Sci. Technol. 5(1972) 213–218.
- [4] A.M Davidson, D.Regener , A Comparison of Aluminium-Based Metal Matrix Composites Reinforced With Coated and Uncoated Particulate Silicon Carbide, Composite Science And Technology Vol.107(6),2000, pp 865-869

- [5] Wagner V., Evolution of Aluminium Alloys for aeronautics After the Two World Wars, *Metallurgia Italiana* 97 (6) (2005) 9-21.
- [6] B. C. Pai, GeethaRamani, R. M. Pillai, K. G. Sathyanarayana. Role of Magnesium in Cast Aluminum Alloy Matrix Composites. *Journal of Material Science*. 30(1995) 1903-1911.
- [7] Mallory G. O. Hajdu J. B (eds) (1991) *Electroless plating: fundamentals and applications*. AESF, Orlando, Fla., USA
- [8] G. O. Mallory, J. B. Hadju, *Electroless plating: fundamentals and applications*, AESF, Orlando, 1991.
- [9] Montgomery, D. C., 2007, *Design and Analysis of Experiments*, Wiley India Pvt. Ltd., New Delhi.
- [10] K. Hari Krishnan, S. John, K. N. Srinivasan, J. Praveen, M. Ganesan, P. M. Kavimani, An overall aspect of electroless Ni-P depositions - A review article, *Metall. Mater. Trans. A*. Vol. 37 (2006) pp. 1917-1926.
- [11] P. Sahoo, Wear behaviour of electroless Ni-P coatings and optimization of process parameters using Taguchi method, *Mater. Des.* Vol. 30 (2009) pp. 1341-1349.
- [12] P. Sahoo, S. K. Pal, Tribological performance optimization of electroless Ni-P coatings using the Taguchi method and grey relational analysis, *Tribol. Lett.* Vol. 28 (2007) pp.191-201.
- [13] T. S. N. Sankara Narayanan, K. Krishnaveni, S. K. Seshadri, Electroless Ni-P/Ni-B duplex coatings: preparation and evaluation of microhardness, wear and corrosion resistance, *Mater. Chem. Phys.*, Vol.82 (2003) pp.771-779.
- [14] F. Delaunois, P. Lienard, Heat treatments for electroless nickel-boron plating on aluminium alloys, *Surf. Coat. Technol.*, Vol. 160(2002) pp. 239-248.
- [15] "Design for a quality-an introduction to best of Taguchi and western methods of statistical experimental design" by Robert Lochner
- [16] "Design of experiments – An introduction to Taguchi and methods of statistical experimental design" by Dr. Madhav Phadke
- [17] R. Karthikeyan, S. Ezhil vannan, G. Ranganathan and S. Paul Vizhian "Effect of coating parameters on coating morphology of basalt short fiber for preparation of Al/Basalt Metal Matrix Composites", *Journal of Electrochemical*. (Accepted for Publication)
- [18] Francone. F, 1998-2000; Discipulus owners "Manual & Discipulus tutorials"; Register Machine learning Technologies.inc.

The Performance Study of Alcohol in an Air Gap Ceramic Insulated Diesel Engine with Brass Piston

S Sunil Kumar Reddy^{1*}, V.Pandurangadu², M.Venkat Rao³

¹ Associate Professor, Mechanical Department, N.B.K.R.I.S.T., Vidyanagar -524 413, Nellore (Dt.), A.P., INDIA

² Professor, Department of Mechanical Engineering, JNT University, Anantapur, A.P., INDIA

³ Professor, Department of Mechanical Engineering, N.B.K.R.I.S.T., Vidyanagar -524 413, Nellore (Dt.), A.P., INDIA

Received 12 Dec 2013

Accepted 13 Jun 2014

Abstract

Now a day it is becoming a challenge for the researchers to find a suitable alternative for diesel and to conserve fossil fuels, which are going to drain in the near future. These factors are to be considered for the invention of new designs of engines. This plays a major role for the researchers in the engine design. The alternative fuel selected must be a renewable, environmentally friendly liquid fuel, and it should provide less pollutant emissions. As ours is an agricultural country, the production of sugar cane is more and this plays a vital part in the production of alcohols which is a very good substitute for diesel. But with the high self-ignition temperature and low latent heat, it becomes difficult to burn alcohol in the existing diesel engines at the available compression ratios and injection pressures. But these have a peculiar property, burning at the elevated temperatures in the combustion chamber. Hence, in the present work, a ceramic insulated diesel engine is developed with an air gap between piston and skirt. This retains the heat in the combustion chamber, makes the combustion complete and further improves the thermal efficiency of the engine with a reduction in the emissions. The heat retaining capacity of the engine mainly depends on the piston material. Therefore, an attempt is made, in the present work, to study the performance and the emission characteristics of the engine with brass piston. Further, the turbulence in the combustion chamber provides the homogeneous mixture formation and improves the combustion quality. So the performance parameters of the engine are tested with brass piston insert and with twelve grooves. Among the various piston inserts tested, the brass insert with 12 number of grooves is identified as the best in terms of performance and emissions. However, in the present experimental work, the major problems acknowledged are the drop in volumetric efficiency and lubricating oil descent with the higher prevailing temperatures in the chamber. However, these problems can be overcome by turbocharging and with the development of new lubricating oils.

© 2014 Jordan Journal of Mechanical and Industrial Engineering. All rights reserved

Keywords: Ceramic Engines, Air Gap Insulation, Low Heat Rejection Engine, PSZ, Alcohol, Brass Piston.

1. Introduction

Diesel engines have major applications in the transportation sector which plays a key role in India's economy. But the diesel fuel is depleting at a fast rate and it causes pollution. So an alternative fuel is required. Hence, the alternative fuel selected must be replenishable, cheap and easily available. In our country, the majority of people lives in villages and their main occupation is agriculture. Further, if farmers prepare this alternate fuel, they will become independent for their needs. As India has about 100 million hectares of waste land, farmers can utilize this land which will become an untapped resource for India. Now a day farmers are producing various types of crops that are useful for the production of vegetable oils. Among all the fuels, alcohols are the best which will be the by-product in the production of sugar. Implementation of alcohol as a fuel in I.C. engines in India will lead to many advantages like greening the waste land,

supporting the agricultural sector, rural economy, and reducing the dependence on import crude oil and decreasing pollution. But alcohols have a high self-ignition temperature and a low latent heat which makes the burning of alcohols in diesel engines difficult at the available compression ratios and injection pressures.

Based on the available literature, it is observed that much amount of work has been done on the utilization of alcohol with diesel in the form of a blend. But with blends, the amount of fuel utilized is less and so the farmers will be short on their energy needs. If alcohol is used directly in the diesel engine without a blend with diesel, it will fulfill the requirements. But due to its properties, the combustion of alcohols is possible at the elevated temperatures in the combustion chamber. So in the present work, a ceramic engine is developed with the insulation of the combustion chamber [2, 3 and 4] with ceramics. Ceramics have a higher thermal durability and a lower thermal conductivity that controls the temperature distribution and heat flow in the structure. A lower heat rejection from the combustion

* Corresponding author. e-mail: mohdhn@yahoo.com.

chamber through thermally insulated components increases the available energy. This would increase the in-cylinder work and the amount of energy carried by the exhaust gases, which could also be utilized.

A major breakthrough in the technology of diesel engines has been achieved by the innovative work done by Kamo and Bryzik. R.Kamo *et al.* [6] conducted experiments with 0.13 mm thick thermal barrier coating of PSZ for the piston and cylinder head and 0.5 mm thick coating for cylinder liner. They observed, in the experiment, a higher premix, lower diffusion combustion, a reduction heat transfer loss, a higher heat release in the combustion chamber with 5 to 6 percent improvement in fuel efficiency at all the loads and speeds. T.Morel *et al.* [5] attained higher thermal efficiency at all loads for both heavy and light engines with the various level of insulation at constant peak pressure and A/F ratio. An eight percent improvement in the brake thermal efficiency was observed. Heat rejection was reported to be decreased while exhaust temperature was increased. S.H.Chan and K.A.Khor *et al.* [8] reported 4 to 7 % improvement in fuel consumption in single cylinder DI diesel engine. This was accomplished by using a constant air flow rate with boosting pressure with 1 mm thick PSZ coating to the cylinder head face and the valve heads by placing a short solid PSZ cylinder liner in the area above the piston rings and heat insulated steel piston. Nagalingam *et al.* [12] converted the four stroke diesel engine into LHR engine with the insulation of the components and conducted the experiments with alcohol and concluded that the performance of the engine with the insulation was increased and the emissions were reduced considerably. Y.Miyairi *et al.* [7] reported a reduction in BSFC by 7% under naturally aspirated conditions in single cylinder DI diesel engine. In this attempt, the fuel injection pressure and the amount of fuel injected was kept constant and the cylinder liner was water cooled. The chamber walls are insulated with PSZ. Murthy PVK *et al.* [9] reported the results of their investigations on LHR diesel engine with 3 mm air gap between piston skirt and insert with Nimonic alloy crown. They revealed that the performance was deteriorated at the available injection timing and pressure. At peak loads, the BSFC was decreased by 12 percent and smoke levels by 16 percent, but NO_x levels were increased by 34% with an injection timing of 32 °bTDC. Wallace *et al.* [11] have reported the use of a thermal barrier piston in the adiabatic engine and developed the temperature distribution analysis and reported that the piston top temperature were higher by around 400°C for the thermal barrier pistons.

From the literature, it is observed that a great amount of heat is lost through the piston. Hence, in the present work for the reduction of heat through the piston, thereby increasing the efficiency, an attempt is made with brass piston crown and air gap between piston skirt and crown. The brass crown is also as same as the size of the original piston and can be interchangeable [9, 10]. Similarly with the turbulence in the chamber, a homogeneous mixture can be formed and thus an increase in the efficiency becomes possible. Therefore, in this work twelve numbers of grooves are made on the brass piston and is used for the testing.

2. Objective

The main objective of the present investigation is to figure out the suitability of the insulated engine for alcohol. The experiment has the following phases:

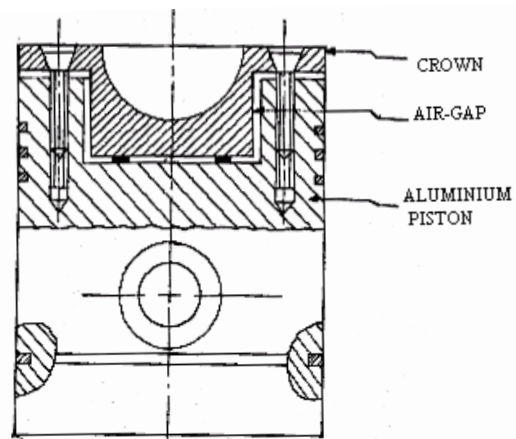
1. Conversion of the conventional diesel engine into insulated engine
2. Investigations with different piston inserts
3. Results and discussions

2.1. Conversion of the Conventional Diesel Engine into Insulated Engine

The important and most complicated part of the experimental work is the conversion of the normal diesel engine into an insulated engine with the insulation of the various components of the engine. So the engine components are insulated first. The detailed method of insulation is given below.

2.1.1. Piston Insulation

With the available literature, an air gap of 2 mm is optimized between the piston crown and skirt. This air gap retains the heat in the chamber. Figure 1 shows the line diagram and photographic view of the piston crown used in the experiment.



(a) Line diagram



(b) Photographic view of aluminum crown

Figure 1. Air gap insulated Aluminum crown

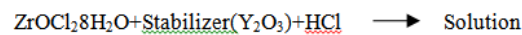
2.1.2. Cylinder Liner Insulation

As the piston is moving in the cylinder, the air gap insulation of 2 mm is provided on the outer surface of the liner. This insulation reduces the heat transfer to the cooling medium.

2.1.3. Cylinder Head and Valve Insulation

The ceramics have better heat and wear resistant characteristics, which retains the heat in the combustion chamber, improves the combustion efficiency, and reduces the pollutant emissions. For the present experiment, ceramic is chosen as the insulating material because of its low density, high thermal stability, and stability in severe chemical environment, its requiring low thermal conductivity and its favorable strength as well as its creep behavior. Ceramic coating is a simpler method of insulation for cylinder head and valves compared to other methods. The method of coating the Partially Stabilized Zirconia (PSZ) on the engine components are explained below.

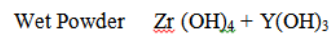
Zirconia is usually produced from the zircon ($ZrSiO_4$). For the production of the zirconia, the zircon is to be added with NaOH and HCl, so that the zircon is converted to zirconyl chloride. The reactions are as follows:



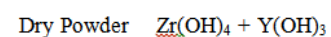
(Wash)

Cl-free Precipitate

(Filtration)



(Freezing Dry (Liquid N_2))



(Calcination)



Figure 3. Photographic view of plain brass piston (BP)

With the available PSZ powder, the coating will be done on the cylinder head and valve surfaces. In coating, the following processes are involved:

1. Pre-cleaning and pre-machining of the cylinder head and valve surfaces to remove rust, scale, paint, etc.
2. Coating of the PSZ powder on the component surfaces using plasma spraying technique up to the required thickness.
3. Final finishing operations, like grinding, lapping, polishing and cleaning.



Figure 2. PSZ coated cylinder head and valves

With the above specified methods, the cylinder head and valves bottom surfaces are machined to a depth of 0.5 mm and further insulated by coating the area exposed to the combustion with PSZ. The surface was then sand blasted to form innumerable pores. This coating prevents the heat flow through the cylinder head and valves. The PSZ coated cylinder head and valves are as shown in Figure 2 above. All these insulated parts, described above, are interchangeable with the standard engine parts.

2.2. Investigations with Different Piston Inserts

In the present work, for the reduction of the heat transfer from piston to the skirt, a piston is designed similar to that of the original aluminum piston which retains the heat in the combustion chamber and preheats the incoming charge. Further, for the good turbulence in the combustion chamber, an attempt is made with twelve numbers of grooves on the brass crown piston. The size and the shape of the groove are selected in such a way that a maximum number of grooves will be generated on the brass piston with the available technology. This brass crown piston is further knurled to increase its surface area to facilitate a better heat transfer from the gases to the brass crown. The brass pistons, tried in the work, are shown in Figures 3 and 4, and the same is compared with aluminum piston.



Figure 4. Photographic view of Brass crown piston crown with twelve grooves (BP12)

2.3. Results and Discussions

The experimental study is carried out on a single cylinder, water-cooled 3.68 KW Kirloskar ceramic coated diesel engines by changing piston crowns. First, the engine is operated with an aluminum piston by the diesel fuel. Then, it is further operated with alcohol with an aluminum piston and then with brass inserts. Both performances are mentioned in the graphs. If the engine is operated at the normal injection pressure, more alcohol will be injected into the combustion chamber due to its lower viscosity. Owing to its high latent heat of vaporization, it cools the engine combustion chamber. So for the present work the fuel injection pressure is reduced to 165 bars. All the tests are conducted at the rated speed of 1500 rpm.

The concentration of smoke is measured by Bosch smoke meter; UHC and NO_x are measured with non-dispersive infrared (NDIR) AVL exhaust gas analyzer. The air suction rate and the exhaust air flow rates were measured with the help of an air box method. Temperatures at the inlet and exhaust valves are monitored using Nickel-Nickel Chromium thermocouples. The time taken to consume 20 cc of fuel was noted down using a digital stop watch. Engine RPM is measured with an electro-magnetic pick up in conjunction with a digital indicator of AQUAH make. The diesel fuel and alcohol fuel are subjected to performance and emission tests on the engine with various piston inserts and the analysis of these results are as follows. The experimental set up used in the present work is shown in Figure 5.



Figure 5. Photographic view of Insulated Engine Experimental set up

2.3.1. Exhaust Gas Temperature

With the lower thermal conductivity of the PSZ, it holds the heat generated in the combustion chamber. Further, the brass piston restricts the heat flow through the piston. This increases the combustion efficiency and exhaust gas temperature, which makes the ignition of alcohol positive. Figure 6 shows the variation of exhaust gas temperature for three different types of pistons in an insulated engine. The exhaust gas temperature for brass piston is 560°C and for aluminum it is 510°C at full load with diesel. The exhaust gas temperatures of diesel fuel and alcohol with aluminum piston are closer. With the higher prevailing temperatures in the chamber, the complete combustion of diesel has taken place. The complete burning of alcohol in the chamber is attributed to the oxygen content in alcohol and the insulated

environment in the chamber. The turbulence provided by the grooves on the piston increases the exhaust gas temperature. So the insulated engine with BP12 shows maximum temperature at rated loads, which is 2.12% more than BP. The increased temperature inside the engine cylinder will increase the entropy and, in turn, will reduce the efficiency slightly, but it is controlled by the higher latent heat of alcohol. Further, this heat is rejected to the exhaust. This high temperature exhaust gas energy can be recovered by a turbo compounding system.

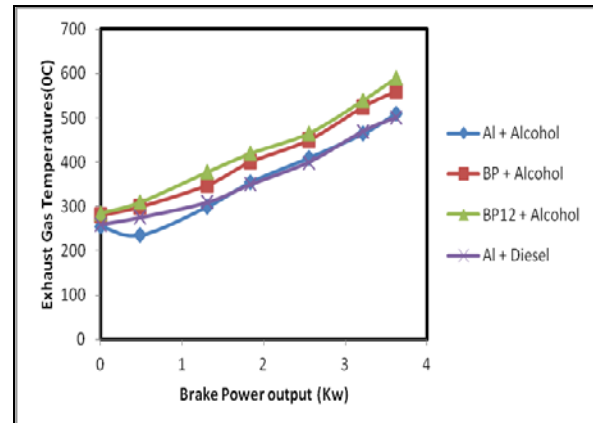


Figure 6. Comparison of Exhaust gas temperature with power output

2.3.2. Brake Thermal Efficiency

Figure 7 shows the variation of brake thermal efficiency of the ceramic insulated engine with the power output for various piston inserts. With ceramic insulation, the heat flow is restricted to the cooling system and these further increases with the brass pistons, air gap between piston and skirt, and with the grooves on the brass piston. As the brass crown piston acts as a good heat reservoir, it maintains the heat in the chamber and further combustion completes. The efficiency with brass pistons is comparatively more than the aluminum piston. So the brake thermal efficiency of BP12 is increased by about 1.58% compared to BP at the rated loads. The efficiency of alcohol with the aluminum piston is slightly more than the diesel. This is endorsed to the alcohols fuel injection pressure and oxygen content in the alcohol.

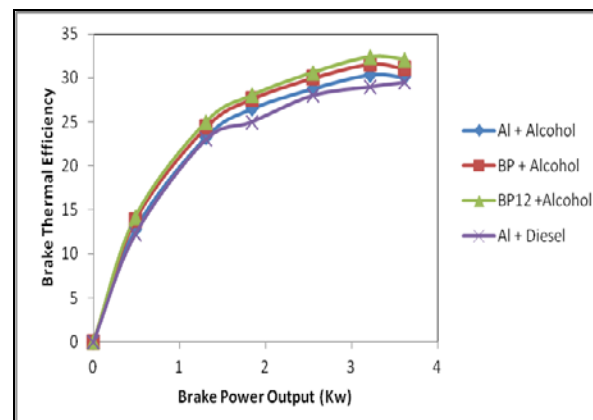


Figure 7. Variation of brake thermal efficiency with power output

2.3.3. Volumetric Efficiency

Figure 8 depicts the volumetric efficiency variation for various piston materials. With the basic properties of brass material, it absorbs the heat during the combustion process and the same heat is given back to the incoming charge in the suction stroke. This enhances the temperature of the inward charge and makes the combustion complete. The higher temperatures in the combustion chamber, with the brass pistons, trims down the density of the inward charge, drops the volumetric efficiency, and plunges the power output. This heat depends on the formation of homogeneous mixture and further turbulence in the combustion chamber. The amount of heat retaining capacity varies for different materials.

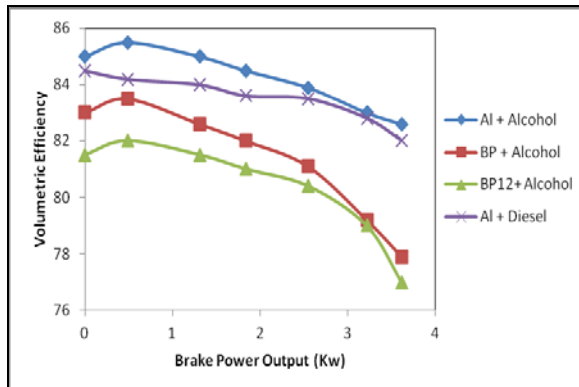


Figure 8. Variation of Volumetric Efficiency with Power output

The aluminum piston volumetric efficiency fluctuates from 85% at no load to 82% at full load. This fall in the volumetric efficiency varies with the heat in the combustion chamber. So for BP the absolute drop is 3.35% compared to the aluminum piston at the rated load, and the fall in the volumetric efficiency with BP12 is peak and is about 1% compared to BP. This reduction of volumetric efficiency is to be compensated with turbocharging.

2.3.4. Smoke Density

With the inferior operating temperatures and due to the lack of oxygen, the combustion will be incomplete in the combustion chamber and this may cause smoke in the exhaust. But in the present work the brass piston holds the heat in the chamber and it prevails the high temperatures in the combustion chamber. Further, the inherent oxygen content in alcohol and the higher operating heat cause the complete combustion and oxidation of the soot particles which reduce smoke emissions. Smoke densities were calculated by opacity test for the fuels. As the load is increased the rich mixture is formed and increases smoke intensities. The variation of exhaust smoke intensity for brass piston material is shown in Figure 9.

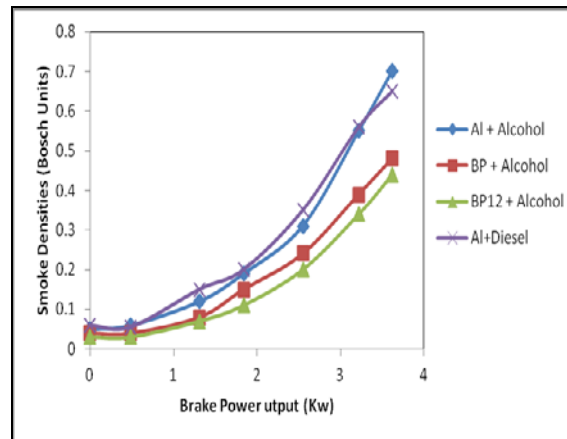


Figure 9. Comparison of Smoke intensity with power output

From the graph above, it is observed that the brass piston showed the lowest smoke emissions over the entire operating range and the reduction is about 19.8 percent. This will increase further with BP12 due to the turbulence generated by the piston. The drop is about 16 percent compared to BP.

2.3.5. Hydrocarbon Emissions

The variations of hydrocarbon emissions with power output for the different piston materials are illustrated in Figure 10. The main sources of these emissions in the diesel engine are lean mixing, burning of lubricating oil, and wall quenching. In spite of the rich air-fuel mixture due to the lower volumetric efficiency, the HC emissions are reduced considerably due to the completion of the combustion of the fuel with hot combustion chamber. From the graph, it is observed that the maximum reduction is with BP12. This is because of its material properties and turbulence generation. The reduction is about 6.26% compared to BP at the rated load.

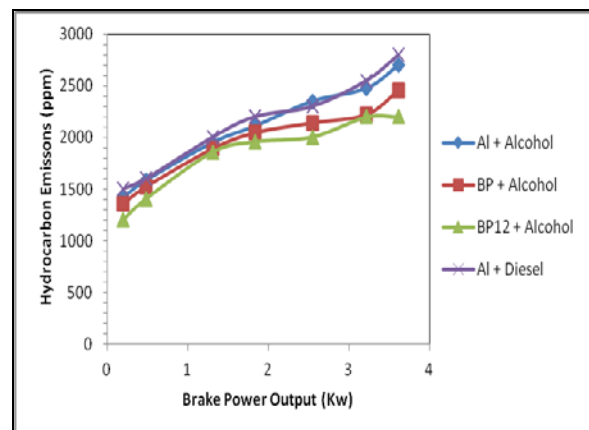


Figure 10. Comparison of Hydrocarbon emissions with power output

2.3.6. Nitrogen oxide Emissions

Figure 11 illustrates the variation of NO_x emissions with various piston inserts of the ceramic insulated engine. The amount of NO_x present in the combustion chamber, relies on the evaporation rate of the fuel. This increases the formation of the NO_x emissions with the availability of oxygen and the higher prevailing temperatures in the chamber.

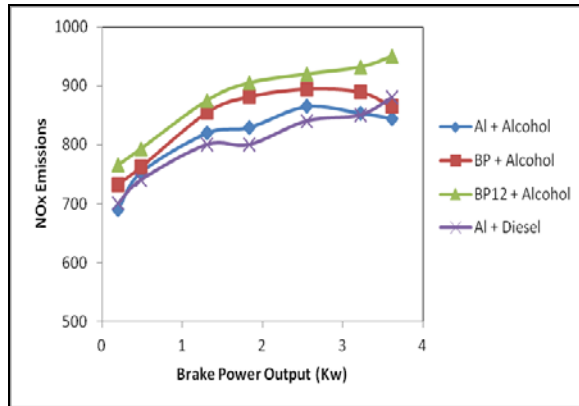


Figure 11. Comparison of Nitrogen Oxide emissions with power output

As the temperature with BP12 is higher, the increase in NO_x emissions is also more and is about 4% compared with base aluminum piston. The emission with BP is in between aluminum piston and BP12.

Conclusions

Following are the conclusions drawn based on the experimental results obtained while operating single cylinder ceramic insulated air gap diesel engine fuelled with diesel and alcohol:

- The brake thermal efficiency and exhaust gas temperatures with brass piston are more because it acted as a regenerator.
- With turbulence, BP12 performed well in terms of emissions and efficiency.
- The insulated components in the engine increase the available energy at the chamber and are evident with the exhaust gas energy which can be used to run a low pressure turbine.
- The volumetric efficiency of the ceramic engine is reduced with the higher operating temperatures of the chamber. This can be recovered with turbocharging system.
- With the higher temperature in the chamber NO_x emissions are more with BP12 compared to all other pistons.
- With the higher operating temperatures of the ceramic engine, the performance of the lubricating oil deteriorates resulting higher friction. This problem can overcome with new liquid lubricants or solid lubricants.
- The higher temperature in the chamber enables the use of low cetane fuels and confers the multi-fuel handling capability.

Good homogeneous mixture formation, complete combustion and lower pollutant emissions are the main important factors for the high-quality diesel engine

performance. These factors are highly influenced by viscosity, density amount of oxygen present in the fuel, etc. For alcohol, these factors are in a considerable range and can be modified easily. With the burning of alcohol in the diesel engine, it can be considered as a preferable replacement for the diesel fuel, thereby promoting our economy and making farmers self-sufficient.

References

- [1] Roy Kamo Adiabatic, Inc., Walter Bryzik and Michael Reid, "Coatings for improving Engine Performance", SAE 970204
- [2] D.A Parker, G.M Donnison,, "The Development of an Air Gap Insulated Piston", SAE Paper No.990652, Detroit, Feb. 1999.
- [3] S.J.Dhinagar, B.Nagalingam., K.V Gopalakrishnan., "Use of Ceramics in Internal Combustion Engines", Proceedings of 10th National Conference on IC Engines and Combustion, India,1997.
- [4] Tadeusz Hejwowski, "Comparative study of thermal barrier coatings for internal combustion engine", Vacuum 85(2010)
- [5] T.Morrel, P.N.Blumberg, E.F.Fort, "Examination of key issues in LHR engines", SAE 850356
- [6] R.Kamo, N.S.Mavinahally, L.Kamo, Bryzik, E.E.Schwartz, "Injection Characteristics that improve performance of ceramic coated diesel engines", SAE 1997-01-0972.
- [7] Y.Miyairi, T.Matsuhisa, T.Ozawa, N.Nakashima, "Selective heat insulation of combustion chamber walls for a DI Diesel engine with Monolithic Ceramics", SAE 980186
- [8] S.H.Chan and K.A.Khor, "The effect of thermalbarrier coated piston crown on engine characteristics", ASM International, Vol. 9 (2000) pp.103-109
- [9] P.V.K Murthy, M.V.S Murali Krishna, A, Sitaramaraju "Performance Evaluation of Low Heat Rejection Diesel Engine with pure diesel", International Journal of Applied Engineering Research, Dindigul, Vol. 1 (2010) No.3, pp?.
- [10] N Pankaj, Shrirao, Anand N. Pawar, "An overview on thermal barrier coating (TBC) materials and its Effect on Engine performance and emission", International journal of applied research in mechanical engineering Volume 1, 2011
- [11] F.J. Wallace, T.K. kao, M. Tarabad, W.D. alexander, and A. Cole, "Thermally insulated diesel engine" proc. of the Institution of Mech.Engg., Vol. 198, No.:5,97-105
- [12] P.R.Srivathsan, P.Terrin babu, S.Prabhakar "Experimental Investigation on a low heat rejection engine", International Conference on Frontiers in Automobile and Mechanical Engineering at Sathyabama University, Chennai on Nov-25-27, 2010.
- [13] G.Sivakumar, Dr.V.Shankar, Dr.G.Hemath kumar, "Is Thermal barrier coating for low heat rejection in SI engines or Diesel engines", International journal of emerging technology and advanced engineering, Vol. 2 (2012) issue 12
- [14] B.Nagalingam, S.Jabez Dhinagar and K.V.Gopalakrishnan, "Spark assisted alcohol operation in low heat rejection Engine", SAE 950059
- [15] C Hasimoglu," Exhaust emission characteristics of a Low heat rejection diesel engine fuelled with 10 percent ethanol and 90 percent diesel fuel mixture", Journal of Automobile Engineering, Vol. 222 (2008) Number 1, pp 93-100.
- [16] Alan C. Hansen , Qin Zhang , Peter W.L. Lyne , " Ethanol-diesel fuel blends—a review " Bioresource Technology, Vol. 96 (2005) Issue 3, pp 277-285.
- [17] Indian Petroleum and Petrochemicals Statistics 2009-2010, page 61, published by the Economics and Statistics Division, Department Of Petroleum., Ministry of Petroleum, Chemicals and Fertilizers, Govt. of India.

- [18] Kenneth G. Budinski and Michael K. Budinski, "Engineering Materials Properties and Selection", Edition 9, Printice Hall PTR, 2010
- [19] Kamal Kishore Khan, Dilip sharme, Senthil kumar, " The effect of thermal barrier coatings on diesel engine Performance of PZT loaded cynate mofied Epoxy coated combustion chamber". Jordan Journal of Mechanical and Industrial Engineering, Vol. 5 (2011) Number 1, pp ?.
- [20] M.Al-Hassan, H.Mujafet and M. Al-Shannag, " An Experimental study on the solubility of a diesel-ethanol blend and on the performance of a diesel engine fueled with diesel-biodiesel-ethanol blends". Jordon Journal of Mechanical and Industrial Engineering Vol. 6 (2012), Number 2, pp?.

Direct Torque Control of Induction Motor Based on Space Vector Modulation Using a Fuzzy Logic Speed Controller

Abdesselem Chikhi *

Department of Electrical Engineering, University of Batna, 05000, Algeria
Street Chahid Med Boukhrouf, Batna 05000, Algeria; Fax + 213 33 81 24 80.

Received 17 Jul 2013

Accepted 22 May 2014

Abstract

In the present paper, the proposed direct torque control using space vector modulation is based on a fuzzy logic technique to replace proportional integral regulator PI anti-windup of the speed of induction motor. In order to reduce torque, flux ripples and gets a swifter response velocity in comparison with the conventional DTC based on SVM. The MATLAB SIMULINK programming environment is used as a simulation tool. The results obtained show the importance of this control method.

© 2014 Jordan Journal of Mechanical and Industrial Engineering. All rights reserved

Keywords: Induction Motor IM, Direct Torque Control DTC, Space Vector Modulation SVM Proportional Integral PI, Fuzzy Logic Controller FLC

Nomenclature

DTC: Direct torque control.
SVM: Space vector modulation.
PI: Proportional integral.
FLC: Fuzzy logic controller.
FDTC: Fuzzy direct torque control
IM: Induction motor.

1. Introduction

High dynamic performance of induction motor drives is indispensable in many applications of today's automatically controlled machines. Induction motor control has attracted much attention recently in the power electronics field. Vector control based in rotor flux orientation presents a major disadvantage to be relatively sensible to the machine parameters variation. For such reasons, the direct torque control (DTC) methods of the induction machines have been developed during the nineties [1]. The basic concept is to control both stator flux and electromagnetic torque of the machine simultaneously. Its simple structure is due to the use of two hysteresis comparators and switching vector tables for both flux and torque control. The hysteresis controller is usually a two-value bang-bang controller, which results in taking the same action for the big torque error and small torque error [2]. Thus, it may produce a big torque ripple. To overcome the above problems, a few researchers have so far

presented the DTC scheme using the space vector modulation (SVM) techniques.

To control the speed of an induction motor driven by the DTC-SVM. The Proportional-Integral controller is always the preferred choice. This is because the implementation of the PI controller requires minimal information about the motor, where the controller gains are tuned until a satisfactory response is obtained [3].

As the induction motor is naturally a non-linear system and is subject to parameter variations, external disturbances, and non-linear loads, PI controller may not give a satisfactory performance when subjected to these conditions as shown by [4].

Nowadays, fuzzy logic is considered an interesting alternative approach for its advantages: analysis close to that of man-operator, ability of nonlinear systems control, best dynamic performances and the inherent quality of robustness.

The objective of this paper is, first, to solve the problems of torque ripple and inconstant switch frequency of inverter in the conventional direct torque control, a new DTC-SVM method for a speed control of AC motor drive is proposed. Second, to control the speed of AC motor driven by DTC-SVM using fuzzy controller in order to improve the speed of the response, small overshooting and fine precision in high and low speed.

2. Principle

Using the vectorial expressions, the machine in the reference frame binds to the stator is defined by:

* Corresponding author. e-mail: chikhi_aslem@yahoo.fr.

In the DTC system, the same active voltage vectors are applied during the whole sample period, and possibly several consecutive samples give rise to relatively high ripple levels in stator current, flux linkage and torque. One of the proposals to minimise these problems is to introduce Space Vector Modulation (SVM), which is a pulse width modulation technique that is capable of synthesising any voltage vector lying inside the sextant spanned by the six PWM voltage vectors.

In this method, DTC-SVM has proved to generate very low torque and flux ripples while showing almost as good dynamic performance as the DTC system. The DTC-SVM systems, though being a good performer, do introduce extra complexity [6].

The fluctuation of the IM torque has a closed relationship to the deviation from an ideal rotation stator flux vector Φ_{sref} which has a constant rotational speed and a constant length. The difference between Φ_{sref} and Φ_s , which is generated in a three-phase PWM inverter, causes torque pulsation. The relationship between torque pulsation $\Delta\Gamma_e$ and the deviation of Φ_s from Φ_{sref} has been deduced as:

$$\frac{\Delta\Gamma_e}{\Gamma_{e\text{ref}}} = k_s \frac{|\Delta\Phi_s|}{|\Phi_{sref}|} + k_\delta \Delta\delta \quad (5)$$

Where $\Gamma_{e\text{ref}}$ is the steady state torque $\Delta\Phi_s$ and $\Delta\delta$ are respectively the deviations from $|\Delta\Phi_s|$ and δ which are defined by:

$$\begin{aligned} \Delta\Phi_s &= |\Phi_{sref}| - |\Phi_s| \\ \Delta\delta &= \angle\Phi_{sref} - \angle\Phi_s \end{aligned} \quad (6)$$

Where k_s and k_δ are the constants derived from the IM specifications.

The torque ripple is actually caused by $\Delta\Phi_s$ and $\Delta\delta$ and the influence of the $\Delta\Phi_s$ is considerably smaller than that of $\Delta\delta$. As a consequence, the torque ripple can be almost removed if $\Delta\delta$ is kept close to zero.

In Figure1, one can notice that the torque error $\Delta\Gamma_e$ and the reference stator flux amplitude $|\Phi_{sref}|$ are delivered to voltage vector calculation, which, in its input, gives the deviation of reference stator flux angle.

From the α , β axes components of the stator reference voltage V_{sref} , are calculated as:

$$V_{s\alpha\text{ref}} = \frac{\Phi_{sref} \cos(\delta + \Delta\delta) - \Phi_{sref} \cos(\delta)}{T_s} + R_s I_{s\alpha} \quad (7)$$

$$V_{s\beta\text{ref}} = \frac{\Phi_{sref} \sin(\delta + \Delta\delta) - \Phi_{sref} \sin(\delta)}{T_s} + R_s I_{s\beta} \quad (8)$$

Where the vector magnitude and angle are given as,

$$V_{sref} = \sqrt{V_{s\alpha\text{ref}}^2 + V_{s\beta\text{ref}}^2} \quad (9)$$

$$\delta = \arctan \left(\frac{V_{s\beta\text{ref}}}{V_{s\alpha\text{ref}}} \right) \quad (10)$$

Where, T_s is the sample time of system.

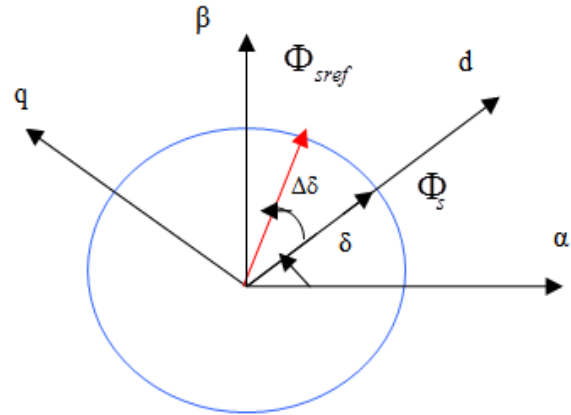


Figure 2. Representation of stator flux vectors Φ_s and Φ_{sref}

The voltage vectors, produced by a 3-phase inverter, divide the space vector plane into six sectors as shown in Figure3. In every sector, the arbitrary voltage vector is synthesised by a basic space voltage vector of the two sides of the sector and the one zero vector. For example, in the first sector, V_s is synthesised by the voltage space vector equations (10) and (11),

$$\bar{V}_{sref} T_s = \bar{V}_0 T_0 + \bar{V}_1 T_1 + \bar{V}_2 T_2 \quad (11)$$

$$T_s = T_0 + T_1 + T_2 \quad (12)$$

Where, T_s is the sample time of system, T_0 , T_1 and T_2 are the work times of the basic space voltage vector V_0 , V_1 and V_2 , respectively (Figure 4); with T_1 and T_2 are given by simple projections:

$$\begin{cases} T_1 = \frac{T_s}{2E} (\sqrt{6} V_{s\beta\text{ref}} - \sqrt{2} V_{s\alpha\text{ref}}) \\ T_2 = \sqrt{2} \frac{T_s}{E} V_{s\beta\text{ref}} \end{cases} \quad (13)$$

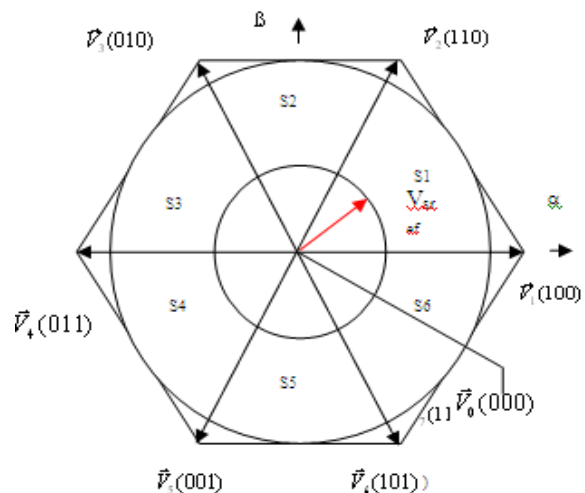


Figure 3. Diagram of the inverter exported voltage space vector

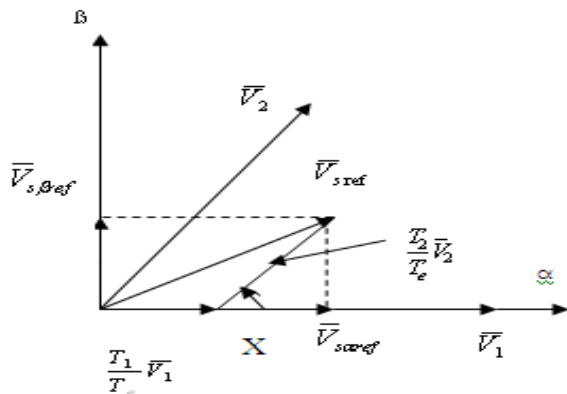


Figure 4. Projection of the reference voltage vector

The rest of the period is spent in applying the null-vector. For every sector, the commutation period is calculated. The amount of the times of vector application can all be related to the following variables: [7].

$$\begin{cases} X = \frac{T_s}{E} \sqrt{2} V_{s\beta \text{ ref}} \\ Y = \frac{T_s}{E} \left(\frac{\sqrt{2}}{2} V_{s\beta \text{ ref}} + \frac{\sqrt{6}}{2} V_{s\alpha \text{ ref}} \right) \\ Z = \frac{T_s}{E} \left(\frac{\sqrt{2}}{2} V_{s\beta \text{ ref}} - \frac{\sqrt{6}}{2} V_{s\alpha \text{ ref}} \right) \end{cases} \quad (14)$$

Table 1 . Applications durations of the sectors boundary

Sectors	T1	T2
1	Z	Y
2	Y	-X
3	-Z	X
4	-X	Z
5	X	-Y
6	-Y	-Z

The third step is to compute the three necessary duty cycles as:

$$\begin{cases} T_{aon} = \frac{T_s - T_1 - T_2}{2} \\ T_{bon} = T_{aon} + T_1 \\ T_{con} = T_{bon} + T_2 \end{cases} \quad (15)$$

The last step is to assign the right duty cycle (T_{xon}) to the right motor phase according to the sector.

Table 2. Assigned duty cycle to the PWM outputs

Sector	1	2	3	4	5	6
Sa	Tbon	Taon	Taon	Tcon	Tbon	Tcon
Sb	Taon	Tcon	Tbon	Tbon	Tcon	Taon
Sc	Tcon	Tbon	Tcon	Taon	Taon	Tbon

4. Fuzzy Logic Speed Controller

In the objective to cancel the static error and to reduce the time response while preserving the system stability, the proportional integral corrector PI used is replaced with a fuzzy logic controller.

4.1. Fuzzy Logic Controller

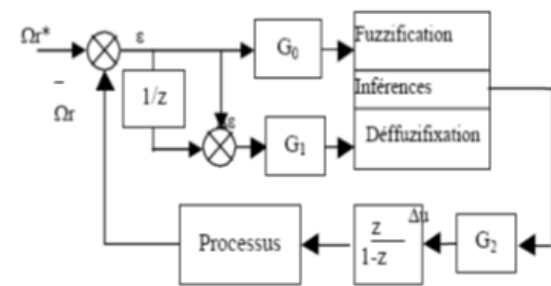


Figure 5. Fuzzy logic controller topology

The block diagram of the loop is made up mainly of the process to control, fuzzification blocks, inference and defuzzification where we define the membership functions of ϵ , $\Delta\epsilon$, and Δu for the first, fuzzy rules and their deduction for the second and the conversion of fuzzy variable into deterministic value for the third, of standardization factors (G_0 , G_1 and G_2), respectively associated at the input $\epsilon = \omega_{ref} - \omega_r$, also its variation $\Delta\epsilon$ and the control variation Δu [8].

4.2. Fuzzification

It rests on a positioning of the fields of possibilities in fuzzy subsets. For our case, the regulator has two inputs ϵ , $\Delta\epsilon$ and for the fuzzified outputs Δu as follow: for ϵ et Δu , we have seven linguistic terms (NS,NM,NB,EZ,PS,PM,PB) and for $\Delta\epsilon$ only three which are (N,EZ,P), each one of them is defined by a membership function of the triangular type according to Figures 6 and 7.

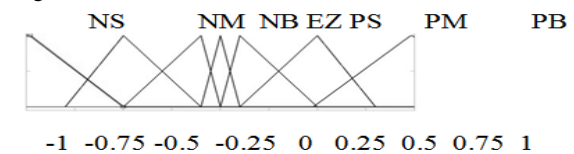


Figure 6. Fuzzy subset ϵ and Δu

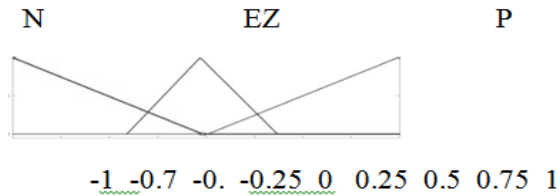


Figure 7. Fuzzy subset $\Delta\epsilon$

4.3. Rules

The set of rules is described according to the decision table of Mac Vicar [9] with the format If-Thus under the fuzzy rules table with two inputs variables according to:

Table 3. Decision table Mac Vicar

$\Delta u \ \Delta \epsilon$	ϵ	NB	NM	NS	EZ	PS	PM	PB
N		NM	NS	EZ	PS	PM	PB	PB
EZ		NB	NM	NS	EZ	PS	PM	PB
P		NB	NB	NM	NS	EZ	PS	PM

4.4. Interfacing

The choice of the inference method depends upon the static and dynamic behavior of the system to regulate, the control unit, and, especially, on the advantages of adjustment taken into account.

We have adopted the inference method Max-Min because it has the advantage of being easy to implement on the one hand and gives better results on the other hand [9].

4.5. Defuzzification

The most used defuzzification method is that of the center of attraction of balanced heights, our choice is based on the latter owing to the fact that it is easy to implement and does not require much calculation [10].

5. Simulations Results

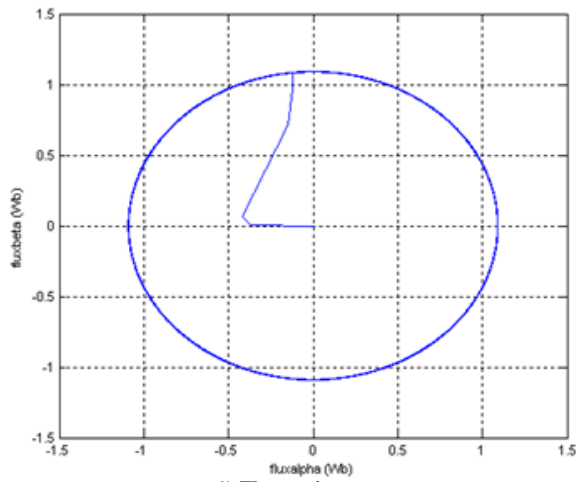
In order to illustrate the improvements that offer a fuzzy regulator with regards to a classic PI for the static and dynamic performances of the control of the asynchronous machine with DTC using space vector modulation, we led a study of simulation with the same test conditions such as the three transitory modes: a no load starting, an introduction of a load torque and the inversion of the direction of speed rotation, and to test the control robustness with respect to the parametric variations.

5.1. Introduction of Load Torque

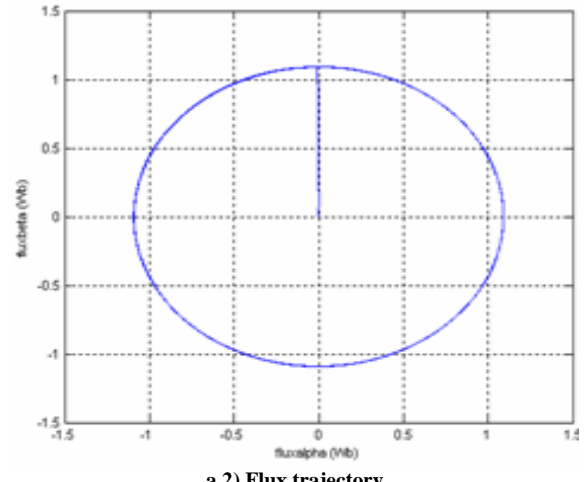
To test the adjustment robustness of the induction machine with fuzzy logic controller, we have introduced a load torque of 25N.m at $t=0.5s$; to examine this test further, we used a step of instruction of 25N.m at $t=0.5s$, see Figure 8. It is noted that the speed reaches its reference $\omega_{ref} = 100rad/s$ without going beyond and that the disturbance rejections due to the applied instructions of loads at the various above mentioned moments are eliminated in contrast to those observed during the adjustment by classic PI, see Figure 7. It is also noted that the regulation effect always persists; indeed the electromagnetic torque acts very quickly to follow the instructions of the introduced loads and presents a remarkable reduction in the harmonics.

5.2. Inversion of Speed Direction of Rotation

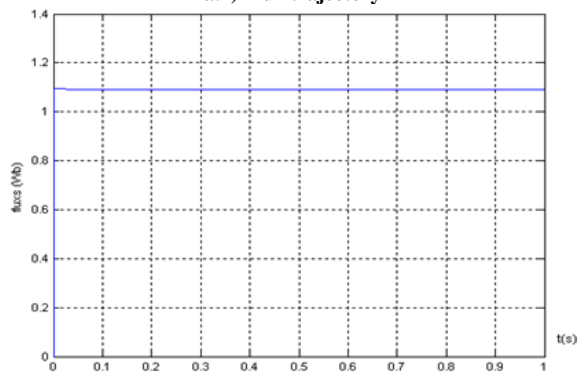
Figure 8 clearly illustrates the robustness of the fuzzy regulator, particularly the speed response with regards to a significant inversion of its reference from 100 rad/s to -100 rad/s. and for low speed for 20 rad/s to -20 rad/s, it is clearly noted that the speed is established without going beyond and converges quickly to its reference. However, the electromagnetic torque marks a peak at starting and another reverse at the change of the speed direction of the rotation, but the braking time at starting, in the reverse direction, is relatively shorter than that obtained by a classic PI.



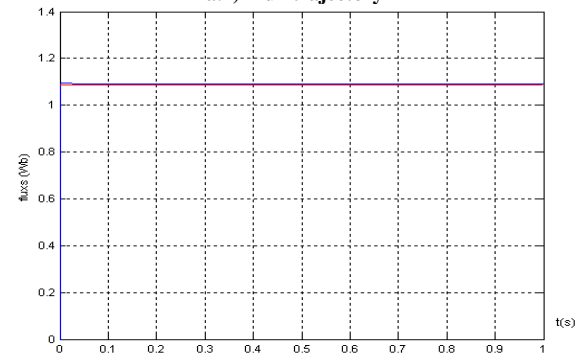
a.1) Flux trajectory



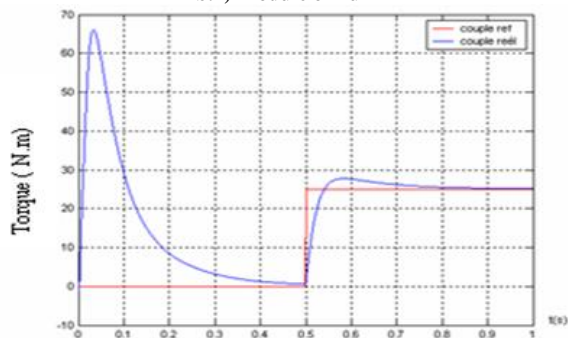
a.2) Flux trajectory



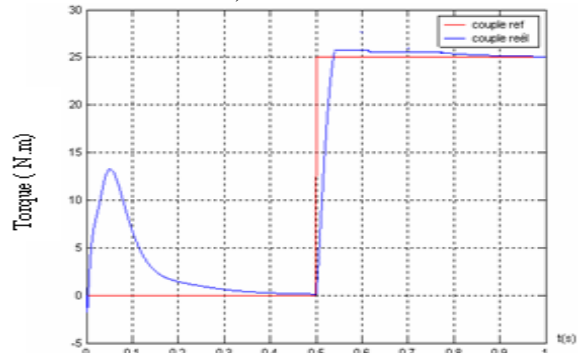
b.1) Module of flux



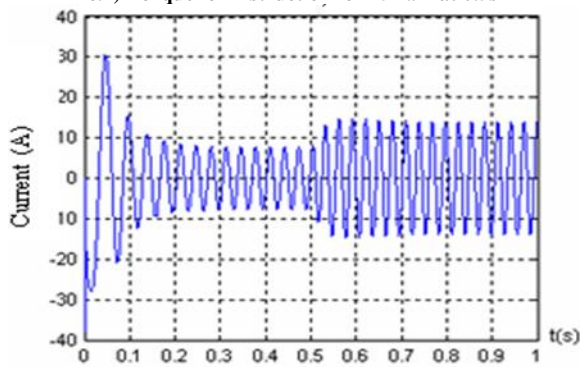
b.2) Module of flux



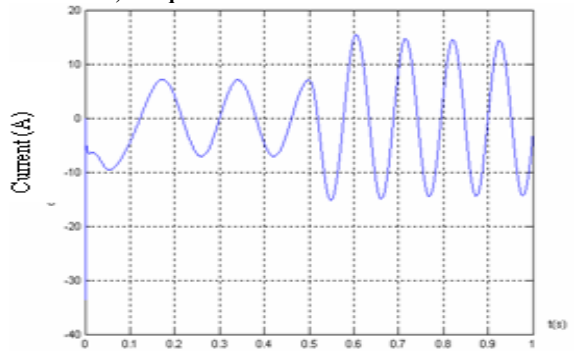
c.1) Torque for instruction for 25 N.m at 0.5s



c.2) Torque for instruction for 25 N.m at 0.5s



d.1) Current



d.2) Current

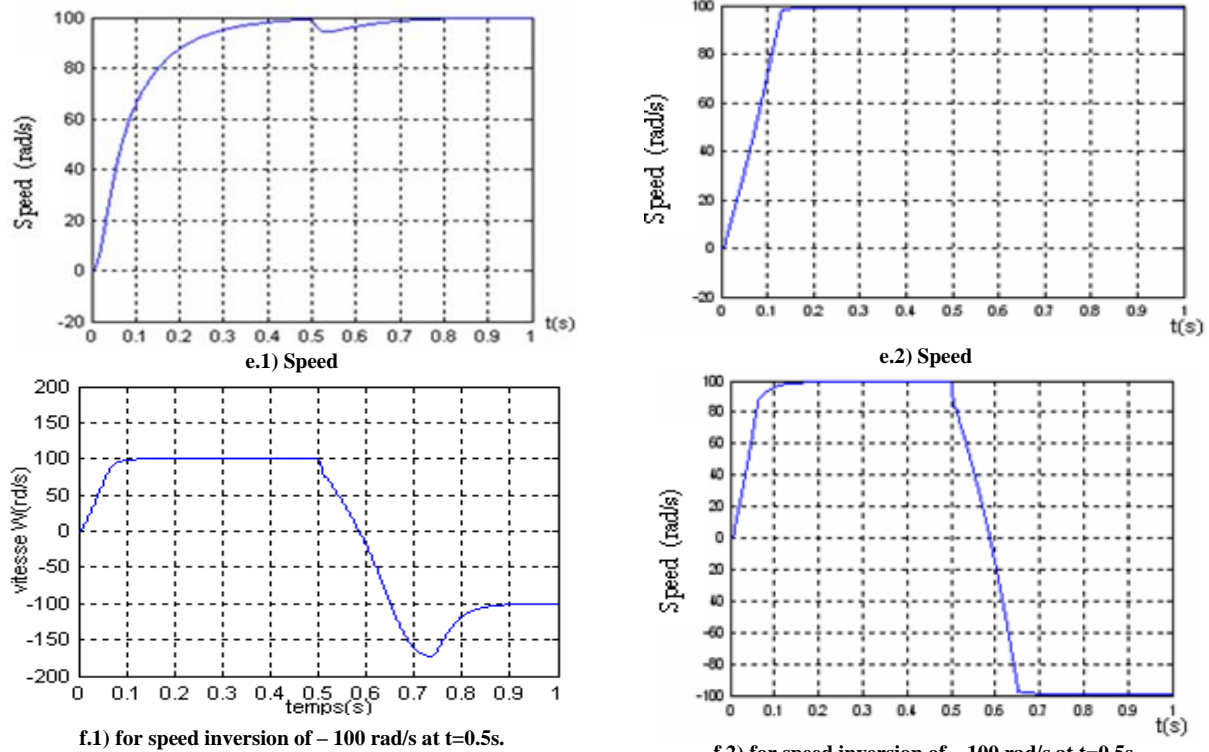


Figure 8. The system response with classic PI

Conclusion

In the present study, we have introduced the principles of the fuzzy logic control and have also justified our choice of this method for the control of asynchronous machines. After having chosen the method of Simulink simulation and having confirmed its effectiveness, we have used this simulation under several operating conditions in order to exploit, with exactness, the different results obtained. Thus, it was clearly shown that the fuzzy controller exceeds the classic regulator. But in spite of the robustness of FLC fuzzy logic controller for all the considered variations (load torque and inversion of the speed direction of rotation) with respect to classic PI, there are certain reserves on the characteristics of this new control technique when the operating conditions change in large band. In conclusion, it is believed that the DTC, using SVM principle, will continue to play a strategic role in the development of high performance drives [11].

References

- [1] X. del Toro Garcia, A. Arias, M. G. Jayne, and P.A. Witting, "Direct Trque control of induction motors utilizing three-level voltage source inverters", IEEE Transactions on Industrial Electronics, Vol. 55 (2008) No. 2, pp. 956-958.
- [2] B. P. Panigrahi, D. Prasad, S. Sengupta, " A simple hardware realization of switching table based direct torque control of induction motor", Electric Power Systems Research, Vol. 77 (2007) No. 2, pp. 181-190.
- [3] Z. Zhang, R. Tang, B. Bai, and D. Xie, "Novel Direct Torque Control Based on Space Vector Modulation With Adaptive Stator Flux Observer for Induction Motors", IEEE transactions on Magnetics, Vol. 46 (2010) No. 8, pp. 3133–3136.
- [4] G.R.A. Markadeh, J. Soltani: Robust Direct Torque and Flux Control of Adjustable Speed sensorless induction Machine Drive based on Space Vector Modulation using a PI predictive Controller, Electrical Engineering, Vol. 88 (2006) No. 6.

- [5] A. Sapin, P. K. Steamer, J. J. Simond, "Modeling simulation and test of three-level voltage-source-inverter with output LC filter and direct torque control", IEEE Transactions on Industry Applications, Vol. 43 (2007) No. 2, pp. 469-475.
- [6] Ozkop E, Okumus H I, "Direct torque control of induction motor using space vector modulation (SVM-DTC)", 12th International Middle-East on Power System, MEPCON, 2008, pp. 368-372.
- [7] J. Soltani, G. R. A. Markadeh, and N. R. Abjadi, "A new adaptive direct torque control (DTC) scheme based-on SVM for adjustable speed sensorless induction motor drive," in ICEMS, Seoul, Korea, Oct. 8-11, pp. 497-502, 2007.
- [8] A. Miloudi, E. A. Al-radadi, A. D. Draou, "A Variable Gain PI Controller Used for Speed Control of a Direct Torque Neuro Fuzzy Controlled Induction Machine Drive", Turk Jour Elec Engin, Vol. 15 (2007) No. 1, pp. 37-49.
- [9] J. Zhijun, H. Shimiao, C. Wenhui, "A New Fuzzy Logic Torque Control Scheme Based on Vector Control and Direct Torque Control for Induction Machine", (ICIC'08), 2008.
- [10] S. Xi Liu, M. Yu W, Y. Guang Chen, S. Li, "A Novel Fuzzy Direct Torque Control System for Three-level Inverter-fed Induction Machine", International Journal of Automation and Computing, Vol. 7 (2010) No. 1, pp. 78-85.
- [11] H. Li, Q. Mo, Z. Zhao, "Research on Direct Torque Control of Induction Motor Based on Genetic Algorithm and Fuzzy Adaptive PI Controller", International Journal on Measuring Technology and Mechatronics Automation, Vol. 3 (2010) pp. 46-49.

Appendix: Simulation Parameters

Stator resistance $R_s = 1.2\Omega$.
 Rotor resistance $R_r = 1.8\Omega$.
 Stator inductance $L_s = 0.1554$ H.
 Rotor inductance $L_r = 0.1568$ H.
 Rotor time constant $T_r = 0.0871$ s.
 Mutual inductance $M = 0.15$ H.
 Motor inertia $J = 0.07$ Kg.M².
 Coefficient of friction $f = 0.00$ N.m/rad/s.
 Number of pole pairs $P = 2$.
 Reference Flux $\Phi_{ref} = 1.1$ Wb.
 Rated power $P_n = 4$ Kw.
 Rated speed $\omega_n = 100$ Rad/s.



الجامعة الهاشمية



المملكة الأردنية الهاشمية

المجلة الأردنية
للمهندسة الميكانيكية والصناعية

JJIMIE

مجلة علمية عالمية محكمة
تصدر بدعم من صندوق البحث العلمي

<http://jjmie.hu.edu.jo/>

ISSN 1995-6665

المجلة الأردنية للهندسة الميكانيكية والصناعية

مجلة علمية عالمية محكمة

المجلة الأردنية للهندسة الميكانيكية والصناعية: مجلة علمية عالمية محكمة تصدر عن عمادة البحث العلمي و الدراسات العليا في الجامعة الهاشمية بالتعاون مع صندوق دعم البحث العلمي في الأردن.

هيئة التحرير

رئيس التحرير

الأستاذ الدكتور نبيل عنقارة

قسم الهندسة الميكانيكية و الصناعية، الجامعة الهاشمية، الزرقاء، الأردن.

الأعضاء

الأستاذ الدكتور ناصر الحنيطي
الأستاذ الدكتور سهيل كيوان
الأستاذ الدكتور محمود زعل ابو زيد
الأستاذ الدكتور محمد أحمد حمدان
الأستاذ الدكتور إبراهيم الروابدة
الأستاذ الدكتور امين الربيدي

مساعد رئيس هيئة التحرير

الدكتور خالد الوديان

الدكتور اسامة منيزل

فريق الدعم

تنفيذ وإخراج

م.مهند عقدة

المحرر اللغوي

الدكتور قصي الذبيان

ترسل البحوث إلى العنوان التالي

رئيس تحرير المجلة الأردنية للهندسة الميكانيكية والصناعية

عمادة البحث العلمي والدراسات العليا

الجامعة الهاشمية

الزرقاء - الأردن

هاتف : 00962 5 3903333 فرعي 4147

Email: jjmie@hu.edu.jo

Website: www.jjmie.hu.edu.jo